UAB
Universitat Autònoma de Barcelona

Self-assembled Nanomaterials: Targeted Strategies for SARS-CoV-2 Capture

Molood Behbahanipour

Universitat Autònoma de Barcelona
Departament de Bioquímica i Biologia Molecular
Institut de Biotecnologia i Biomedicina

Self-assembled Nanomaterials: Targeted Strategies for SARS-CoV-2 Capture

Doctoral thesis presented by Molood Behbahanipour
for the degree of PhD in Biochemistry, Molecular Biology
and Biomedicine from the Universitat Autònoma de Barcelona

The work presented in this thesis was performed
in the Department of Biochemistry and Molecular Biology
and the Institute of Biotechnology and Biomedicine, under the supervision of
Dr. Jordi Pujols Pujol, Dr. Susanna Navarro Cantero, and Prof. Salvador Ventura Zamora

Molood Behbahanipour

Dr. Jordi Pujols Pujol	Dr. Susanna Navarro Cantero	Prof. Salvador Ventura Zamora

Bellaterra, January 2025

SUMMARY

This doctoral thesis centers on developing innovative bioengineered prion-inspired protein assemblies aimed at neutralizing Severe Acute Respiratory Syndrome Coronavirus 2 (SARS-CoV-2), providing potential applications in antiviral surfaces and therapeutic interventions. In this regard, a generalizable modular method using the 21-residue Soft Amyloid Core (SAC) peptide from the Sup35 yeast prion domain has been applied as an assembling module fused to two different high-affinity binding domains that recognize the Receptor Binding Domain (RBD) of SARS-CoV-2 spike protein. To do so, we have implemented two distinct bioengineered platforms to build stable and biocompatible materials. First, we incorporated our binding domains to insoluble amyloid-like fibrils, exploiting Sup35-SAC self-assembly. Second, we built soluble amyloid-like oligomers, referred to as OligoBinders. Nanofibrils offer a potential solution as a viral neutralization material for high-risk public spaces to prevent virus transmission, while OligoBinders are a promising candidate for diagnostics, therapeutics, and preventive measures against viral transmission. Both approaches leverage the self-assembly nature of prion domains to create targeted, safe, and biocompatible antiviral modular tools. These findings indicate broader implications for bioengineered antiviral materials, potentially extending to other viral pathogens beyond SARS-CoV-2.

RESUMEN

Esta tesis doctoral se centra en el desarrollo de ensamblajes proteicos bioingenierizados para neutralizar el Coronavirus 2 del Síndrome Respiratorio Agudo Severo (SARS-CoV-2), ofreciendo nuevas estrategias antivirales para el desarrollo de soluciones terapéuticas y herramientas de diagnóstico. Para ello, explotamos las propiedades de autoensamblaje de la proteína Sup35 de levadura. En concreto, la capacidad amiloidogénica del fragmento de 21 residuos correspondiente a su núcleo de agregación (SAC). Fusionamos el péptido SAC de Sup35 a dos dominios de alta afinidad capaces de reconocer el Dominio de Unión al Receptor (RBD) de la proteína Spike de SARS-CoV-2 para así generar una proteína quimérica bifuncional sobre la cual basamos el desarrollo de dos biomateriales diferentes. Primero, explotando las propiedades amiloidogénicas inherentes de la región SAC generamos fibras funcionales (Nanofibrils) para crear un entramado capaz de reconocer y capturar SARS-CoV-2. Segundo, construimos oligómeros solubles (OligoBinders) que neutralizan partículas víricas de SARS-CoV-2. Mientras que las Nanofibras encuentran su potencial aplicación en la neutralización de materiales como superficies y soluciones acuosas para prevenir transmisión vírica, los Oligomeros tiene una aplicación dirigida a su uso clínico, ya sea como estrategia terapéutica o de diagnóstico. Ambos materiales reportados en la presente tesis, aprovechan las propiedades de autoensamblaje propias de los priones naturales para crear nuevas aplicaciones seguras, dirigidas y compatibles con biomateriales aplicados a la salud. Los resultados sugieren que la composición modular de nuestros biomateriales puede extenderse a otros patógenos y aplicaciones más allá de la neutralización del SARS-CoV-2, abriendo las puertas a la bioingeniería de nuevos nanomateriales.

RESUM

Aquesta tesis centra els esforços en el desenvolupament d'ensamblatges protèics bioenginyeritzats per neutralitzar el Coronovirs 2, causant de la Síndrome Respiratoria Aguda Greu (SARS-CoV-2), oferint noves estratègies antivirals pel desenvolupament de solucions terapèutiques y de diagnòstic. Per fer-ho, explotem les propietats d'autoensamblatge de la proteïna Sup35 de llevat. En concret, la capacitat amiloidogènica del fragment de 21 aminoàcids corresponent al seu nucli d'agregació (SAC). Fusionem el pèptid SAC de Sup35 a dos dominis d'alta afinitat capaços de reconèixer el Domini de Unió al Receptor (RBD) de la proteïna Spike de SARS-CoV-2 per generar una proteïna quimèrica bifuncional sobre la qual basem el desenvolupament de dos biomaterials diferents. Primer, explotant les propietats amiloidogèniques de la regió SAC generem fibres funcionals (Nanofibrils) per crear un entramat capaç de reconèixer i capturar SARS-CoV-2. Segon, construim oligòmers solubles (OligoBinders) que en neutralitzen les partícules víriques. Mentres que les Nanofibres tenen potencial per a ser aplicades en la neutralització de materials com superfícies y solucions aquoses per prevenir la transmissió vírica, els OligoBinders es poden aplicar en usos clínics, ja sigui com a estratègia terapèutica o de diagnòstic. Ambdós materials reportats en la tesis s'aprofiten de les propietats d'autoensamblatge pròpies dels prions naturals per a crear noves aplicacions segures, dirigides y compatibles amb biomaterials aplicats en el camp de la salut. Aquests resultats suggereixen que la composició modular dels nostres biomaterials es pot extrapolar a altres patògens y a noves aplicacions més enllà de la neutralització de SARS-CoV-2, obrint les portes a la bioenginyeria de nous nanomaterials.

TABLE OF CONTENTS

List of abbreviations 1

Introduction 2

1. Protein Structure 2

1.1 Protein Folding 3

2. Protein Self-Assembly 7

2.1 Determinants of Protein Self-Assembly 8

2.1.1 Driving Forces of Protein Self-Assembly 8

2.1.2 Intrinsic Factors 10

2.1.3 External Influencing Factors 11

2.2 The Significance of Self-Assembly in Biological Systems 12

3. Amyloid-Based Self-Assembled Nanomaterials 13

3.1. Aggregation and Amyloid Fibril Formation 13

3.2. Structural Characteristics of Amyloid Fibrils 15

3.3. Physicochemical Properties of Amyloid Structures 17

3.4. Oligomers: Soluble Intermediate Species in the Amyloid Aggregation Process 18

3.5. Functional Amyloid and Amyloid-Based Nanomaterials 19

4. Prion and Prion-Like Proteins 22

4.1. Prions 22

4.2. Prion-Like Proteins 23

4.3. Differences Between Prion-Like Domains and Classical Amyloid Stretches 24

4.4. Prion-Inspired Nanomaterials 25

4.5. Soft Amyloid Cores in Prion Domains and Their Use in Nanomaterials 27

5. Targeting Severe Acute Respiratory Syndrome Coronavirus 2 29

Research objectives 31

CHAPTER 1: Bioengineered self-assembled nanofibrils for high-affinity SARS-CoV-2 capture and neutralization 34

CHAPTER 2: OligoBinders: Bioengineered Soluble Amyloid-like Nanoparticles to Bind and Neutralize SARS-CoV-2 48

Concluding remarks 63

References 65

ANNEX 1: Supplementary materials Chapter 1 74

ANNEX 2: Supplementary materials Chapter 2 89

List of abbreviations

RNase A	Ribonuclease A
TMV	Tobacco Mosaic Virus
CCMV	Cowpea Chlorotic Mottle Virus
GSTs	Glutathione S-Transferases
ThT	Thioflavin T
Cryo-EM	Cryo-Electron Microscopy
ssNMR	solid-state Nuclear Magnetic Resonance
EPR	Electron Paramagnetic Resonance
TEM	Transmission Electron Microscopy
AFM	Atomic Force Microscopy
CR	Congo red
Far-UV CD	Far-UV Circular Dichroism
FTIR	Fourier-Transform infrared
CPEB	Cytoplasmic Polyadenylation Element Binding Protein
IDRs	Intrinsically Disordered Regions
PrDs	Prion Domains
PrLDs	Prion-Like Domains
FTD	Frontotemporal Dementia
ALS	Amyotrophic Lateral Sclerosis
CC	Coiled-coil
APRs	Amyloid-Prone Regions
HS	Hot Spots
LARKS	Low-complexity Aromatic-Rich Kinked Segments
SAC	Soft Amyloid Core
RBD	Receptor-Binding Domain
DHFR	Dihydrofolate Reductase
COVID-19	Coronavirus Disease 2019
SARS-CoV-2	Severe Acute Respiratory Syndrome Coronavirus 2
AgNPs	Silver Nanoparticles
mAbs	monoclonal Antibodies
hACE2	human Angiotensin-Converting Enzyme

Introduction

1. Protein Structure

Proteins are the most abundant biomolecules in the cell. They are vital for nearly every dynamic process in living organisms, including providing structural support, enzymatic activity, regulating hormones, functioning as antibodies, transporting molecules, controlling gene expression, enabling muscle contractions, signal transduction, and even acting as an energy source when necessary (Creighton, 1993). There are approximately 100,000 distinct types of proteins, each defined by its unique sequence of amino acids that are linked together in a polymeric chain disposition. To become functional, proteins adopt a specific three-dimensional structure, known as the native state (Dobson, 2004). For some proteins, the native state adopts a compact and stable conformation, while for others, it remains disordered or partially disordered but still fulfils essential functional roles. The protein structure is typically categorized into four levels: The **primary structure** is the linear sequence of amino acids linked by peptide bonds. The **secondary structure** involves localized folding into α-helices, β-sheets, β-turns and loops, mostly stabilized by hydrogen bonds between backbone atoms. The **tertiary structure** is the overall three-dimensional folding of the single polypeptide, driven by various intramolecular interactions between side chains of amino acids, including hydrogen bonds, Van der Waals forces, electrostatic interaction, hydrophobic interactions, and disulfide bridges. Moreover, multiple polypeptide chains (subunits) might assemble through non-covalent intermolecular interactions to form a multimeric protein. This functional protein complex is referred to as a the **quaternary structure** (Herczenik & Gebbink, 2008).

The study of protein structure plays a pivotal role in biochemistry, biomedicine, and molecular biology. Techniques such as X-ray crystallography, Nuclear Magnetic Resonance (NMR) spectroscopy, and cryo-electron microscopy (cryo-EM) have resolved numerous protein structures and enabled a deeper understanding of the relationship between protein structures and how these proteins operate both in normal physiology and in pathological conditions. In this sense, information of protein structures at the atomic level provides the foundation for a wide range of applications. For example, it enables the rational design of therapeutic interventions, such as the rational development of small-molecule drugs that precisely target specific protein regions. As well, protein structures can be redesigned to enhance their functions and address biotechnological and medical challenges (Ebrahimi & Samanta, 2023). In recent years, the implementation of artificial intelligence (AI) tools has revolutionized the

study of protein structures. AlphaFold, developed by DeepMind, leverages deep-learning algorithms to predict protein structures with remarkable accuracy—exceeding 90% in many cases—based solely on amino acid sequences (Jumper et al., 2021). This capability significantly reduces reliance on traditional experimental methods, which are often time-intensive and expensive. By providing access to reliable structural models, unsolved protein structures become accessible (Varadi et al., 2022). For instance, the AlphaFold database contains over 214 million predicted protein structures, which increases the coverage of the human proteome from 48% to 76% (Porta-Pardo et al., 2022).

1.1 Protein Folding

Protein folding is the process by which a protein chain adopts its native structure from an unfolded state. This process is thermodynamically driven, with the native state representing the most energetically favourable conformation. The specific molecular interactions within the protein, as well as its interactions with the surrounding solvent, are determined by the physicochemical properties of the amino acids in the protein chain. Consequently, the amino acid composition and its sequential arrangement encode all the necessary information for the folding process.

Pioneering studies on protein folding began in the early 20th century, with Linus Pauling's research on chemical bonding, particularly the peptide bond, in the 1930s laying the foundation for understanding protein structures. Later, in 1951, Pauling and Robert Corey's proposal of the α-helix and β-sheet structures expanded the knowledge of how protein chains fold into stable configurations (Pauling & Corey, 1951; Pauling et al., 1951). The significant breakthrough in protein folding was achieved in the late 1950s when John Kendrew and Max Perutz uncovered the structures of myoglobin and hemoglobin, respectively, using X-ray crystallography, providing the first high-resolution view of the full three-dimensional structure of proteins (Kendrew et al., 1958; Perutz et al., 1960).

In 1961, Christian Anfinsen's experiments with ribonuclease A (RNase A) guided subsequent protein folding research. He demonstrated the spontaneous refolding of RNase A into its native, bioactive state after denaturation, solely based on the amino acid sequence, without the need for other molecules to control or catalyse the process (Anfinsen et al., 1961). This led to the proposal of what is known as the thermodynamic hypothesis, which states that the sequence of amino acids in a protein contains all the necessary information for the protein to fold into its functional three-dimensional structure, the most thermodynamically stable state, where Gibbs

free energy is minimized under given environmental conditions (Anfinsen, 1973). Later, Cyrus Levinthal made the argument, known as Levinthal paradox, which states that protein folding cannot be solely the result of random thermodynamic search processes. He suggested that there are too many possible conformations for proteins to find their native structures through random exploration in conformational space, which would take an astronomical amount of time (Dill, 1985; Levinthal, 1968; Zwanzig et al., 1992). However, proteins fold within milliseconds to seconds. This paradox led to the idea that protein folding follows preferential pathways, sampling a restricted number of conformations to reach the final folded state. It also initiated the search for models of protein folding, resulting in the development of the concepts of preferential kinetic pathways and the folding funnel.

Folding funnel model conceptualized protein folding as a directed process through a funnel-shaped energy landscape in which at the top of the funnel, the proteins exist in an unfolded state with many possible conformations with high energy. As proteins fold, they move downhill in the funnel with specific pathways, where constantly their energy and the number of accessible conformations are reduced till proteins reach to their most stable, lowest-energy conformation (the native state), which lies at the bottom of the funnel. Then folding funnel concept has been advanced by introducing a more detailed and quantitative approach known as the energy landscape theory. This theory gives an in-depth view of how proteins follow their folding pathways, balancing thermodynamic stability with kinetic efficiency. It posits that proteins have many intermediate states but are directed toward their final folded structure. Considering the folding funnel as a rugged energy landscape, with many local energy minima and barriers, protein's folding process involves navigating a complex surface with multiple routes, some of which involve overcoming energy barriers (high points) and avoiding kinetic traps (local minima), while there is still a general thermodynamic bias through preferred kinetic pathways toward the global minimum (figure 1) (Dill & Chan, 1997).

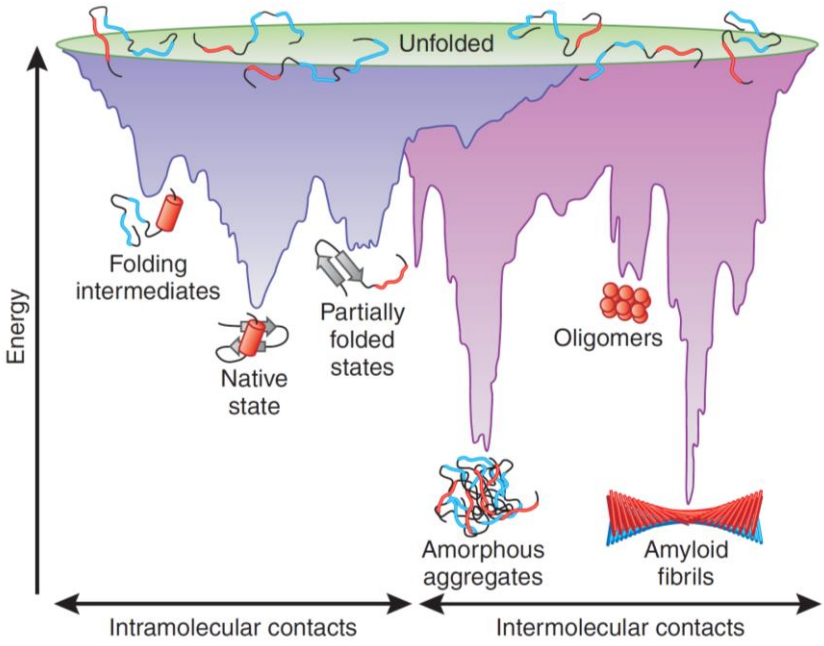

Figure 1. Energy landscape scheme of protein folding and aggregation. The purple surface represents the folding process where proteins move toward their stable native state through intramolecular interactions. The pink area highlights alternative pathways where misfolding leads to amorphous aggregates or amyloid fibrils. These two pathways overlap, with misfolding occurring either during folding or through destabilization of the native state (Hartl & Hayer-Hartl, 2009). The figure has been reproduced with permission from *Nature Structural & Molecular Biology*, Springer Nature.

Considering the **energy landscape theory** as a unifying framework, various structural models contribute to our growing understanding of protein folding, and how protein chains transition from unfolded states to native conformations. The **hydrophobic collapse model**, which explains the rapid early folding due to hydrophobic residues clustering together, this initial collapse then promotes the formation of the secondary structure and other specific interactions, which ultimately lead to the final protein conformation (Tanford, 1962). The **framework model** and **hierarchical folding model** describe how secondary structures such as α-helices and β-sheets form early, providing a scaffold that guides further folding. In the framework model, secondary structures are formed first and independently of tertiary interactions, before assembling into the final structure (Kim & Baldwin, 1982). However, the hierarchical folding model emphasizes that folding occurs in a stepwise, hierarchical manner, where local regions in the sequence that are marginally stable fold first, and these local structures then progressively interact and assemble into larger, more complex structures through a series of intermediate stages, ultimately, leading to the native conformation (Baldwin & Rose, 1999). The **diffusion-**

collision model suggests that protein fold through a process involving fluctuating microdomains (small regions of secondary structure like α-helices or β-strands or hydrophobic clusters) that move diffusively. Finally, these microdomains collide and coalesce to form multimicrodomain intermediate structures, eventually if favourable, they may lock to the native protein conformation (Karplus & Weaver, 1994). The **nucleation–condensation model**, in which folding begins with the formation of critical nuclei that serve as the stable core of the folded structure, while the rest of the protein condenses around this core, completing the folding process cooperatively (Fersht, 1995). For a given protein, the folding pathway may involve a combination of several folding models, by which the protein chain acquires native on-pathway interactions.

Within the cellular environment, despite the complexity of the folding process, proteins avoid kinetic traps through a combination of thermodynamic guidance, biological assistance through chaperones and quality control mechanism (Hartl & Hayer-Hartl, 2009), and additional protein intrinsic properties such as co-translational folding (Bitran et al., 2020) and disulfide bond formation (Hidaka, 2014)). Nevertheless, kinetic trapping can occur in some proteins when they become locked in intermediate structures due non-native interactions, which create high energy barriers. This can lead to various folding outcomes, including the formation of long-term misfolded proteins. These species are non-functional, and in some cases, they can evolve into macromolecular self-assembled arrangements through protein aggregation.

The native state of a protein, though functional, may not necessarily correspond to the most stable conformation. Protein aggregates, in comparison to soluble monomeric proteins, are energetically more favourable and are endpoints of misfolded protein species. This is primarily due to two factors: first, the incremental number of intermolecular interactions provides enthalpic stability. Second, the system's entropy increases as the macromolecular assembly enhances water molecules disorder. Amyloid fibrils, a specific and highly ordered form of protein aggregation, exemplify the structural optimization aimed at minimizing free energy. These exceptionally stable fibrillar structures are implicated in the pathogenesis of several neurodegenerative diseases, such as Alzheimer’s and Parkinson’s Disease (Chiti & Dobson, 2017). As toxic, non-degradable species, their accumulation—whether inside or outside the cell—exceeds the capacity of cellular clearance mechanisms, contributing neuronal death and disease progression.

Altogether, this phenomenon highlights the metastable nature of protein structures, where thermodynamically more stable conformations exist but are kinetically inaccessible under normal physiological conditions. Changes in environmental conditions (e.g., temperature, pH, molecular crowding agents, protein concentration, or the presence of specific aggregates with a certain secondary structure, like β-sheet aggregates) can influence the folding pathway of a protein and, eventually, promote misfolding and aggregation (Baldwin et al., 2011; Baskakov et al., 2001; Varela et al., 2018).

2. Protein Self-Assembly

Self-assembly is a phenomenon widely exploited by nature to expand the structural and functional repertoire of both inorganic and biologic material (Whitesides & Grzybowski, 2002). The principle refers to the ability to autonomously build higher order organizations from an initial limited number of monomeric building blocks. In the protein context, self-assembly allows to create new biological architectures and functions ranging from the molecular level to the nanoscale and macroscale networks (Solomonov et al., 2024). From a thermodynamic perspective, this natural process maintains the system in a stable, low-energy state by balancing repulsive and attractive intermolecular forces (Whitesides & Grzybowski, 2002). Multitude of repetitive and non-covalent weak interactions are involved in the formation of intermolecular interactions between protomeric units of the mature assembled complex, instead of the intramolecular interactions observed in the stabilization of monomeric native conformations.

Protein self-assembly plays a crucial role in physiological conditions. For instance, actin filaments, fundamental to the cytoskeleton, rely on the polymerization of actin subunits, and ribosomes represent complex protein assemblies critical for protein synthesis (Baßler & Hurt, 2019; Pollard & Cooper, 2009). However, self-assembly can also lead to pathological outcomes, as seen in the formation of toxic amyloid aggregates associated with neurodegenerative diseases (Chiti & Dobson, 2017).

The principles of self-assembly have been harnessed in synthetic biology to engineer novel protein-based materials and nanostructures. Examples include the development of silk fibroin scaffolds for tissue engineering (Fan et al., 2021), amyloid-inspired nanofibers for cell adhesion and differentiation (Das et al., 2018), and virus-like particles for encapsulation strategies using nanoparticles (Shimanovich et al., 2014). The primary advantage of self-assembly lies in its ability to be precisely controlled, enabling the creation of biomaterials with tailored structural and functional properties. Through genetic engineering, the primary sequence of proteins can be modified to include assembling modules, functional domains, or specific amino acids

introduced. Understanding the intricate relationship between protein structure and self-assembly behavior is pivotal for scaling up the production of high-precision, adaptive nanomaterials (Solomonov et al., 2024).

2.1 Determinants of Protein Self-Assembly

Strategically control self-assembly of proteins into functional assemblies requires understanding of their building block structures and the mechanisms ruling their interactions. Higher-order protein self-assembly is governed by thermodynamics and kinetics, achieved through both non-covalent and dynamic covalent intermolecular interactions (Li et al., 2022; Wang et al., 2016). The hierarchical organization of protein structures, starting from free amino acids to fully folded native structures, extends seamlessly into the assembly of macromolecular complexes. Just as secondary and tertiary structural elements are acquired and combined to form stable proteins, the interaction between individual protein subunits dictates the form, function, and stability of larger assemblies. Thus, comprehending the interplay between different subunits is critical for elucidating the behavior of protein assemblies.

Protein self-assembly is inherently influenced by both internal factors, such as the intrinsic properties of the protein (e.g., sequence, structure, and flexibility), and external factors, including environmental conditions like pH, ionic strength, temperature, and the presence of cofactors or chaperones. Internal and external factors together govern the pathways and kinetics of assembly, as well as the final structural and functional properties of the assemblies. For example, the hydrophobic collapse of unfolded polypeptides or the templated assembly of amyloid fibrils showcases the critical interplay between internal sequence features and external environmental triggers.

By leveraging these principles, researchers can design biomaterials with precisely controlled properties, opening new avenues in synthetic biology and nanotechnology. Understanding the intricate balance of thermodynamic stability, kinetic pathways, and environmental influences will remain fundamental to advancing our ability to engineer protein self-assembly systems.

2.1.1 Driving Forces of Protein Self-Assembly

Protein self-assembly is primarily driven by a combination of non-covalent interactions. Non-covalent interactions, including hydrogen bonding, hydrophobic interactions, aromatic stacking (π-π stacking), electrostatic interactions, and Van der Waals forces, individually presents weak bond energies (2–250 kJ mol^{-1}) compared to covalent bonds (100–400 kJ mol^{-1}) and are reversible. However, the synergistic effect of these interactions in sufficient numbers

can form highly stable assemblies, and the fine balance between them controls the shape and function of the final structure (Mendes et al., 2013).

For example, hydrogen bonds, involving hydrogen atoms between two electronegative atoms such as nitrogen (in amide or amino groups) and oxygen (in carboxyl groups), can be either inter- or intramolecular. Hydrogen bonding plays a crucial role in protein folding, stabilizing peptide secondary structures, and inducing peptide self-assembly into organized nanostructures due to their selective and highly directional characteristics. The strength of hydrogen bonds depends significantly on the nature of the hydrogen bond donor and acceptor, as well as the surrounding environment (such as the solvent). Their strength can be also increased by combining several hydrogen bonds, and become more specific based on their geometric orientation. Similarly, aromatic π-π stacking among aromatic residues like phenylalanine, tyrosine, and tryptophan, when they cluster together in a face-to-face orientation, provide stability in aqueous environments due to the hydrophobicity of their aromatic group, as well promote the directional growth of peptide assemblies. Particularly, π-π interactions become a stronger driving force in nonpolar solvents, such as toluene, where solvent competition for interaction with aromatic groups is minimized. Hydrophobic interactions also play a significant role in surfactant systems, where amphiphilic peptides aggregate by hiding their hydrophobic tails in the interior, while their hydrophilic heads remain exposed to water. This entropy-driven process is a unique organizing force for the formation of stable structures based on repulsion of solute by the solvent to minimize their contact with water. Unlike π-π stacking, with well-organized arrangement of aromatic amino acids, hydrophobic interactions are non-directional, leading to disordered organization of aromatic residues. Peptide self-assembly is also affected by electrostatic interactions, which are a strong driving force between charged amino acids, particularly in charged peptides, and can be modulated by changes in pH or ionic strength. Furthermore, Van der Waals forces, arising from electron fluctuations between two closely spaced molecules, though weaker, contribute to overall stability when combined with other forces non-covalent interactions (Mendes et al., 2013; Wang et al., 2016).

Dynamic covalent bonding such as disulfide (sulfur-sulfur reactions), imine (aldehyde-amine reactions), and hydrazone bonds (aldehyde-hydrazide reactions), further enhance the complexity and stability of protein assemblies. Disulfide bonds have been shown to act as a stabilizing mechanism for long helical fibril structures, enhancing the overall stability of nanostructures. They can also help form a diverse and dynamic library of mechanically interlocked cysteine-decorated peptides through self-assembly in water (Li et al., 2022).

Metal coordination, where multivalent metal ions interact with proteins mainly through coordination bonds with amino acids that have high electron density groups, also serves as a precise and directional force. Other classic supramolecular forces, including non-covalent host-guest interactions, are known for their higher reversibility and stimulus responsiveness. Receptor-ligand interactions, on the other hand, are distinguished by their reversibility, high selectivity, innate diversity, and strong binding constants (Bai et al., 2016; Li et al., 2024; Zhu et al., 2021). Furthermore, the self-assembly process can be precisely engineered by modifying protein secondary structures. Several strategies are exploited to stabilize α-helical secondary structures and promote peptide self-assembly into stable nanostructures. Since short peptides in α-helical conformation are thermodynamically unstable outside their native environment, stabilizing methods such as hydrogen-bond surrogates (Liu et al., 2008), salt bridge formation (Marqusee & Baldwin, 1987), and the incorporation of non-standard amino acids like α-aminoisobutyric acid are used to facilitate the self-assembly of alpha-helical peptides (Mondal et al., 2015).

2.1.2 Intrinsic Factors

The inherent properties of polypeptides, including the amino acid sequence, side chains characteristics, and hydrophobic or hydrophilic nature of peptides, influence assembly morphology and behaviour, mainly by influencing electrostatic, hydrophobic, or hydrophilic forces (Li et al., 2022). For instance, specific amino acid patterns can significantly alter the resulting nanostructures, such as diphenylalanine peptides have been shown to self-assemble into well-ordered elongated nanotubes, whereas its highly similar analogue, diphenylglycine peptides, due to the restricted rotational freedom and higher steric hindrance from the lack of a methylene group in its side chain, shows lateral growth and forms nanospheres under similar conditions (Reches & Gazit, 2004).

The hydrophobicity and hydrophilicity of peptides significantly affect the self-assembly behaviour, kinetic, or dynamic of self-assembly, and the resulting morphology. For example, increased hydrophobicity can cause a shift in self-assembled nanostructures from vesicles forms to tubes and ribbons. It has also been demonstrated that peptides with longer hydrophobic tails increase the system's entropy and lead to faster self-assembly (Wang et al., 2009).

Furthermore, the order of amino acids in protein sequences can have a significant impact on the self-assembly ability and morphology; since even peptides with very similar overall hydrophobicity and charges may self-assemble in different ways. It has been shown that minor variations in amino acid patterns within protein sequence can result in distinct morphologies,

such as β-sheet nanoribbons, micelle-like aggregates, or even prevent the self-assembly process (Lee et al., 2013). These findings imply the critical role of amino acid sequence and side chain properties in tuning nanostructure morphologies and self-assembly behaviour. Therefore, the rational design and selection of protein sequence is key in controlling the self-assembly process and the formation of nanostructures with the desired morphology.

2.1.3 External Influencing Factors

Protein self-assembly is not only dictated by intrinsic determinants but is also regulated by various external environmental factors, such as temperature, pH, and solvent conditions. Temperature affects both hydrophobic and hydrogen bonding interactions. As the temperature increases, the stability of hydrogen bonds decreases, while the strength of hydrophobic interactions increases. Therefore, temperature variations may affect the self-assembly behaviour in different ways, depending on the relative contribution of these two interactions in the system. Elevating temperature can lead to either irreversible or reversible structural phase transitions for some peptides, while it may not affect others. However, heat denaturation of proteins at temperatures higher than 80°C is usually irreversible because, under these conditions, proteins mostly aggregate. Protein self-assembly behaviour and morphology are also regulated by the pH of the solution. The ionization state of amino acids varies at pH levels significantly higher or lower than physiological pH. Consequently, different charge distributions on protein surfaces can impact electrostatic attraction or repulsion, as well as hydrophobic interactions, favouring or hindering the protein self-assembly process (Li et al., 2022). Solvent conditions play a significant role in self-assembly morphology. For example, diphenylalanine peptides self-assemble into nanometer-sized hollow tubular structures in water, but when acetonitrile is added to the aqueous phase, these peptides form larger structures like microtubes and fibers. And from pure acetonitrile, only small, highly uniform nanofibers can be obtained (Huang et al., 2011). In another study, the self-assembly behaviour of dipeptides derived from D- and L-alanines into twisted nanoribbons shows chiral inversion between water and tetrahydrofuran solvents (Li et al., 2013). Furthermore, eternal stimuli, such as mechanical stress or ultrasound, can cause conformational changes or aggregation. For instance, ultrasound can convert amyloid lysozyme fibrils into non-amyloid forms by breaking their β-sheet structure, or it can induce fibrillation (Solomonov et al., 2024).

2.2 The Significance of Self-Assembly in Biological Systems

Proteins perform a vast array of functions across all living organisms, from viruses to bacteria and eukaryotes, including vital roles in various biological process such as metabolism, chemical transportation, signal transduction and serving as major components of structural scaffolds. Some examples of these self-assembled structures include the planar bacterial surface layer, the cage-like bacterial microcompartment, the helical Tobacco Mosaic Virus (TMV) nanotube, the cyclic light-harvesting system, the filamentous MreB complex, as well as LecA, galactose-binding lectin that can self-assemble into various structures, ranging from linear nanoribbons to two-dimensional nanosheets, and three-dimensional layered structures (Bai et al., 2016; Solomonov et al., 2024). Most of these natural protein assemblies have a high degree of symmetry, which minimizes the number of distinct interaction sites between proteins and leads to energy-efficient interactions and more stability, efficiency, and better functionality. Symmetry-based protein self-assembly is common in biological systems, where natural proteins have evolved to form symmetrical assemblies based on their shape, including closed structures (cyclic, cubic, or dihedral); one-dimensional (linear, helical or cyclic symmetries); two-dimensional (planar symmetries); or three-dimensional (spatial symmetries) (Luo et al., 2016; Zhu et al., 2021). The use of symmetry strategies also inspires the creation of various bottom-up protein assemblies, as their symmetric architecture reduces the complexity of genetic and design process.

The highly synergistic coordination of the protein subunits gives the protein-self-assemblies several advantages over the individual monomeric proteins. First, they possess higher stability and durability while maintaining dynamic reversibility due to their supramolecular structure. These characteristics are essential for adaption to the constantly changing conditions in biological systems. For instance, two major cytoskeletal elements, including actin filaments and microtubules, are polymerized from actin monomers and tubulin dimers, respectively, undergoing dynamic assembly and disassembly in response to internal and external stimuli, enabling structural organization and functional dynamic of cells. In contrast, the third major elements, intermediate filaments, provide more stable structural support, but they can also disassemble and reassemble when necessary, such as during cell division. Another example of reversible self-assembly is stable polyhedral viral capsids Cowpea Chlorotic Mottle Virus (CCMV), which protect viral genomes from harsh extracellular environments, such as variations in pH, temperature, and digesting enzymes. However, with specific recognition, they can disassemble once inside host cells to release viral genome. Another notable example is

protein phase separation, where specific proteins and RNA undergo liquid-liquid phase separation (LLPS), to form dynamic, reversible membraneless compartments like nucleoli, Cajal bodies, and stress granules. This mechanism enables cells to organize molecular components efficiently, regulate key biological functions, and rapidly adapt to environmental changes (Boeynaems et al., 2018). Second, protein self-assemblies demonstrate collective behaviour, enhancing their biological functions and unique physicochemical properties compared to basic single protein monomers due to the periodic patterns of their architecture. This can be observed in the light-harvesting complex, a key component of photosynthesis, which captures and transfers light energy with greater efficiency than the photosynthetic reaction center. Similarly, enzymes like glutathione S-transferases (GSTs), which are involved in detoxifying harmful substances, dimerize to maintain thermodynamic stability and binding affinity, functioning more effectively in oligomeric forms. In fact, most soluble enzymes operate as oligomers (Bai et al., 2016).

Beyond its biological significance, protein self-assembly has emerged as a promising framework for engineering multifunctional biomaterials, offering unparalleled precision in tailoring properties such as size, shape, elasticity, and mechanical strength. The ability to design materials with such precision is rooted in the hierarchical organization of proteins. By manipulating the primary sequence and self-assembly pathways, it is possible to fabricate biomaterials that mimic natural tissues or exhibit entirely novel functionalities. For instance, silk fibroin-based scaffolds have been successfully engineered for tissue regeneration, utilizing silk's ability to self-assemble into robust and flexible fibers (Eliaz et al., 2022; Fan et al., 2021; Li & Sun, 2022; Pacheco et al., 2022). Viral capsids, another example of protein-based assemblies, serve as inspiration for nanoscale delivery vehicles, capitalizing on their natural ability to encapsulate and protect genetic material (Shimanovich et al., 2014)

3. Amyloid-Based Self-Assembled Nanomaterials

3.1. Aggregation and Amyloid Fibril Formation

The protein folding process involves acquiring the most thermodynamically stable protein state through a series of intermediates with the thermodynamically favourable steps, known as on-pathway folding. However, there is also the probability that this process fails, resulting misfolded conformations, which can then interact intermolecularly to form disordered or highly ordered aggregates, a process referred to as off-pathway folding. In both on- and off-pathways, kinetically trapped intermediates are biased toward the global energy minimum. While the on-

pathway is dominated by intramolecular interactions leading to the natively folded state, the off-pathway is dominated by intermolecular interactions that promote highly ordered aggregates. Competition between intramolecular and intermolecular interactions is crucial in determining whether the protein follows the on-pathway folding or off-pathway folding (Figure 1) (Hartl & Hayer-Hartl, 2009).

The primary driving forces triggering off-pathway folding are hydrophobic forces, due to the exposure of hydrophobic residues in the secondary structures and disordered regions of polypeptide chains from partially misfolded and misfolded proteins to the aqueous environment. Nonspecific intermolecular interactions of these misfolded proteins typically cause their aggregation into amorphous aggregates and, in some cases, result in highly ordered aggregates due to the balance between the hydrophobicity and charges. Amyloid fibrils are a well-known example of stable, highly ordered aggregates. However, this does not exclude the fact that amyloid fibrils also exhibit structural polymorphism (Adamcik & Mezzenga, 2018; Hartl & Hayer-Hartl, 2009).

The kinetics of amyloid fibril formation follows a nucleation-dependent polymerization mechanism (Figure 2) (Ferrone, 1999; Lomakin et al., 1996), generally characterized by a three-step process. It initiates with a long lag phase, referred to as the **nucleation process**, during which soluble protein monomers or amyloid-forming peptides start interacting to form prefibrillar species such as oligomers or protofibrils depending on the system or condition, serving as templates for further fibril growth. The nucleation process is thermodynamically unfavourable and slow, as monomeric proteins need to overcome energy barriers to form a nucleus. This process can be shortened by adding pre-formed fibrils, a process called seeding or modulated by factors that destabilize the soluble native protein structure like denaturants, proteolysis, mutations, truncations, low pH, or high temperature, which increase the population of partially structured folding intermediates with exposed aggregation-prone regions. Alternatively, increasing the steady-state concentration of these soluble aggregation-prone intermediates enhances the probability of intermolecular interactions, leading to their coalescence, reducing the lag phase, promoting faster nucleation, and accelerating amyloid fibril formation by seeding further fibril growth. A key idea is that amyloid fibril formation is supposed to represent the lowest free-energy conformation for all polypeptide chains. This process can proceed from partially folded intermediates, either through partial unfolding of the native structure or by partial structuring of unfolded polypeptides to expose amyloidogenic

regions under appropriate solution conditions, followed by their assembly through non-specific interactions and structural changes (such as domain swapping, β-strand stacking, strand association, or edge-edge-association) directed by the physicochemical characteristics of the polypeptide chain and the solution conditions (Chiti et al., 1999; Colon & Kelly, 1992; Guijarro et al., 1998; Jahn & Radford, 2008; McParland et al., 2000; Nelson & Eisenberg, 2006; Uversky & Fink, 2004).

Then the nucleation process is followed by **elongation**, a rapid and thermodynamically favourable exponential growth phase, and finally reaching the **steady or saturation phase** of insoluble mature fibrils. At this step, there is a dynamic equilibrium between the assembly and disassembly of fibrils (Ferrone, 1999; Lomakin et al., 1996).

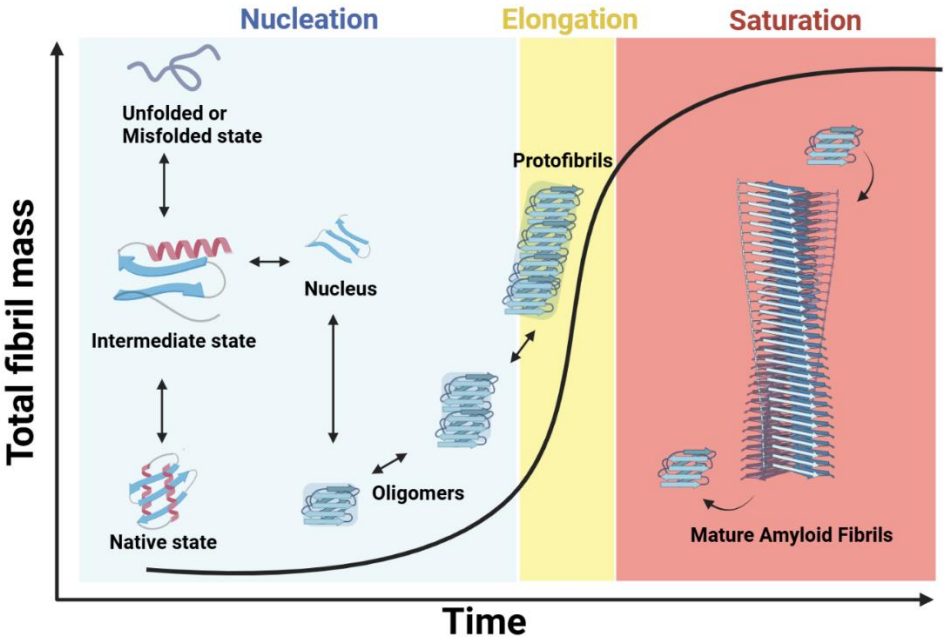

Figure 2. Nucleation-dependent polymerization model. The process of amyloid fibril formation includes a lag phase (light blue), rapid growth phase (yellow), and steady or saturation phase (red), characterized by a sigmoidal kinetic curve that can be monitored using Thioflavin T (ThT) fluorescence or light scattering. In the first step, the soluble and monomeric species do not bind to the ThT dye and do not scatter incident light. As amyloid structures form in the solution, both signals grow proportionally. Created with Biorender.com.

3.2. Structural Characteristics of Amyloid Fibrils

Even though a generic cross-β structure of amyloids was defined approximately 40 years ago, obtaining high-resolution structures of amyloid fibrils due to their insolubility and non-crystalline nature was challenging. Recently advances in experimental methods and techniques

such as cryo-EM, solid-state nuclear magnetic resonance (ssNMR), electron paramagnetic resonance (EPR) and X-ray microcrystallography start revealing detailed image of amyloid fibril architecture and their properties (Eanes & Glenner, 1968; Eisenberg & Sawaya, 2017; Riek & Eisenberg, 2016).

Amyloid fibrils have an invariant structural fingerprint at the atomistic length level. That is characterized by a typical core cross-β-sheet structure, where β-sheets align parallel to the fibril axis, while the β-strands within each sheet are oriented perpendicularly to the fibril axis. The spacing between the β-strands and β-sheets is ~ 4.7 Å and ~ 6-11 Å, respectively based on X-ray diffraction studies (Figure 3) (Greenwald & Riek, 2010).

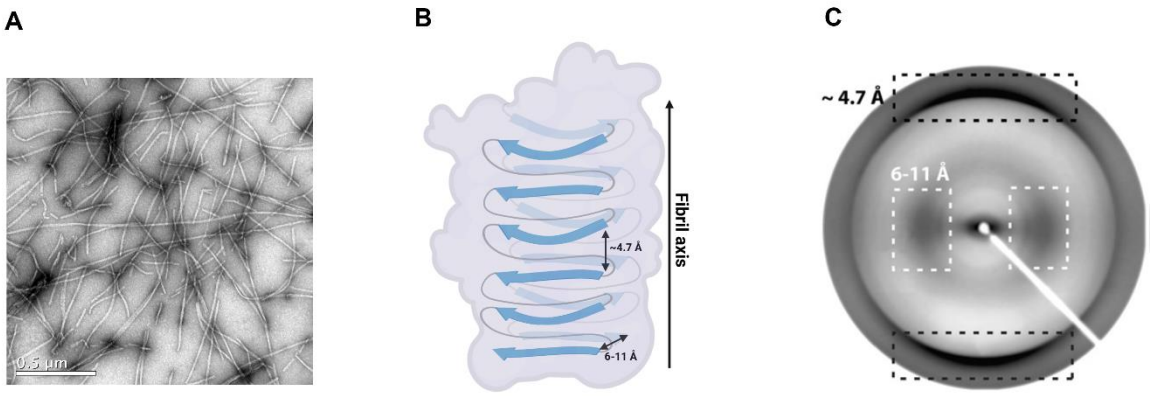

Figure 3. The cross-β structure of amyloid fibrils. (A) Negatively stained transmission electron micrographs of amyloid fibrils. (B) Schematic diagram of cross-β sheets within a fibril filament. β-strands in each sheet are perpendicular to the fibril's axis. Created with Biorender.com. (C) Typical cross-β X-ray fiber diffraction pattern shows two characteristic diffuse reflection: one meridional reflection at ~ 4.7 Å, corresponding to the spacing between stacked β-strands (black dashed box), and one equatorial reflection between ~6–11 Å, corresponding to the spacing between β-sheets (white dashed box) (Greenwald & Riek, 2010).

At the mesoscopic scale, mature amyloid fibrils typically assemble from 2 to 6 protofilaments (Adamcik & Mezzenga, 2018). These protofilaments can associate laterally or twist together, with their side chains fitting tightly in an interlocking arrangement called a steric zipper, forming a dry and stable interface (Riek & Eisenberg, 2016). Amyloid fibrils can be visualised as straight, unbranched structures, approximately 70-120 Å in diameter and at least one micrometre in length, using transmission electron microscopy (TEM) and atomic force microscopy (AFM) (Adamcik & Mezzenga, 2018; Jahn & Radford, 2008).

The amyloid fibrils demonstrate significant diversity in their mesoscopic structures (including, nanotubes, helical ribbons, and twisted ribbons), contributing to their structural polymorphism through different possible three-dimensional arrangements of protofilaments, as well as variations in their number, orientation, and conformations. Notably, amyloid fibrils formed under different conditions show identical structures at the atomic level, with no difference in molecular polymorphism, but exhibit polymorphism at the mesoscopic level (Seuring et al., 2017). Recent studies also suggest that the structural polymorphism is a widespread feature of amyloid fibrils both *in vivo* and *in vitro*, supporting the idea that amyloid fibril formation follows similar physicochemical principles. Besides, the misfolding pathways for amyloid proteins are considered to be conserved throughout the body, independent of where amyloid fibrils form or accumulate, since similar amyloid structures observed in different tissues of one patient and diseased animal (Annamalai et al., 2016; Annamalai et al., 2017).

Amyloid fibrils also demonstrate high mechanical strength, with a Young's modulus comparable to steel and silk. These intrinsic mechanical properties of amyloid fibrils mainly related to the hydrogen bonding between β-strands within each sheet. Likewise, a progressive increase in Young's modulus, along with an increase in β-strand content during fibrillization has been seen (Adamcik & Mezzenga, 2018).

As different polypeptide sequences can form amyloid fibrils, with aforementioned features makes amyloid assemblies an interesting topic of study in both biological and pathological fields.

3.3. Physicochemical Properties of Amyloid Structures

Classical features of amyloid fibrils is their high affinity for Congo red (CR) and Thioflavin T (ThT), two amyloid-specific dyes that widely used for the diagnosis and characterization of amyloid fibrils for many years. Distinct optical properties of amyloid fibrils when stained with CR and ThT dyes involve red-green birefringence under a polarized light and increased fluorescence intensity, respectively. From a spectroscopic point of view, amyloid assemblies show a red-shift in the absorbance maximum of CR from 490 nm to 510-540 nm upon binding, while their binding to ThT results in a fluorescence emission peak at 482 nm. The interaction of these two dyes with amyloid structures are assumed to be related with their incorporation into the grooves of the intermolecular β-sheet structures (Nilsson, 2004; Sabaté & Ventura, 2013).

The characteristic β-sheet structures during amyloid formation can be also monitored by observing changes in the secondary structure using techniques such as far-UV circular dichroism (far-UV CD), displaying a minima peak at 217 nm. Additionally, Fourier-Transform infrared (FTIR) spectroscopy can also be used, as the amide I region of amyloid fibrils shows a narrow, intense absorption peak in the 1615-1630 cm^{-1} range that is lower than typical β-sheets (above 1630 cm^{-1}). This is because amyloid β-sheets are usually large, tightly packed, and highly ordered, resulting in slower and more coordinated molecular vibrations around the C=O (carbonyl) bonds extended along large sections of the fibril backbone, leading to lower infrared absorption than typical β-sheets (Calero & Gasset, 2012; Moran & Zanni, 2014; Sabaté & Ventura, 2013).

In addition, the cross-β-sheet characteristic of amyloid fibrils is highly resistant to digestion by proteinase K (a serine protease) due to their highly ordered and densely packed structures. Therefore, the core of amyloid-like aggregates, depending on their soluble or insoluble nature, can be identified by limited proteolysis with proteinase K, resulting in different digestion patterns (Sabaté & Ventura, 2013).

3.4. Oligomers: Soluble Intermediate Species in the Amyloid Aggregation Process

Soluble oligomers are key intermediates typically formed early during aggregation of proteins and remain in solution after high-speed centrifugation. Amyloid oligomers may initially display disordered or α-helical content, but as they progress during fibrillation, they often undergo a structural transition into β-rich structures, which serve as template for amyloid fibril formation. Nevertheless, some oligomers can also stabilize as final products into toxic or non-toxic species. Their toxic effects are strongly related to their structural instability and hydrophobic properties, which make them more prone to penetrate membrane lipid compositions and disrupt lipid bilayers. These interactions often lead to the disruption of membrane integrity, causing cellular dysfunction and toxicity, which is considered critical in the progression of protein aggregation diseases such as Alzheimer's, Parkinson's, and prion diseases (Bemporad & Chiti, 2012; Breydo & Uversky, 2015; Uversky, 2010) (Figure 4).

Intermediate-sized amyloid oligomers with larger hydrophobic surface exposures and loosely packed, less stable assemblies, are more likely to interact with cell membranes and other cellular structures, causing membrane permeabilization and disassembly compared to larger oligomers (Figure 4). Thus, the size and exposure of hydrophobic surface are two main elements affecting the toxicity caused by oligomers. Additionally, their polymorphism can also

significantly impact their cytotoxic potential and is vital for understanding their variable toxicity observed in amyloid diseases (Stefani, 2010). However, oligomers are not always harmful, as some amyloidogenic proteins form non-toxic oligomers that may even inhibit fibrillation (Muschol & Hoyer, 2023).

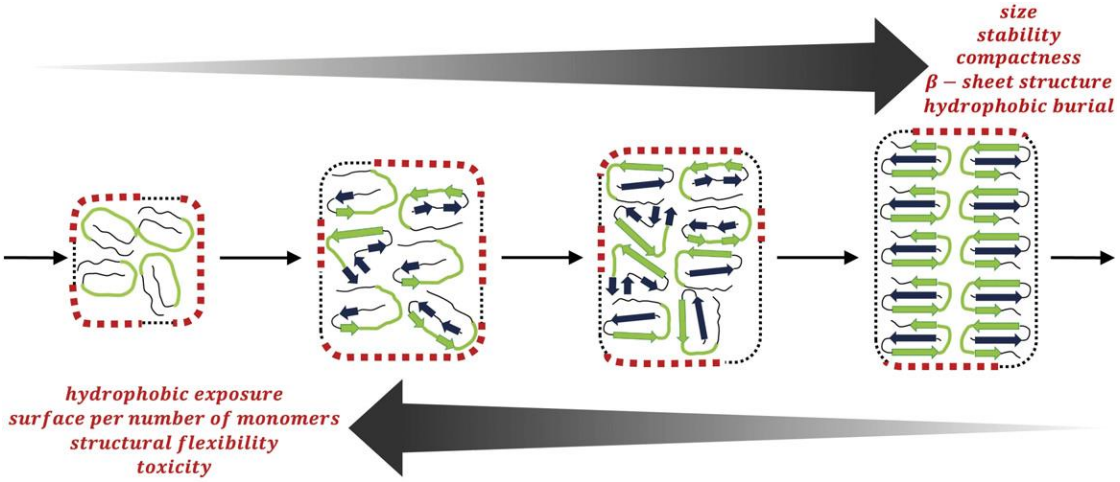

Figure 4. Schematic representation of the structural rearrangement of oligomers during the aggregation process. The top and bottom arrows indicate the increasing and decreasing parameters, respectively, during the process. The oligomer surface is depicted with a thin black dotted line when shielding amyloidogenic segments, while exposed hydrophobic or amyloidogenic surfaces are shown with a thicker red dotted line. Grean segments correspond to amyloidogenic regions, and green and blue arrows represent β-sheet structures. Adapted from (Bemporad & Chiti, 2012).

Despite the lack of detailed information on the structural properties and formation mechanisms due to structural instability and heterogeneity of oligomers, there is evidence that oligomers tend to form β-sheet-rich structures with parallel or antiparallel arrangements, and their size can vary from dimers to larger multimers. The morphology of oligomers can be spheroidal (globular), annular (ring-like), or protofibrillar. They are considered dynamic entities, as their formation, stability, and structure are influenced by the protein sequence and environmental conditions, such as metal ions in solution and chemical modifications (Breydo & Uversky, 2015; Stefani, 2010; Uversky, 2010).

3.5. Functional Amyloid and Amyloid-Based Nanomaterials

Amyloid structures are not only associated with many neurodegenerative diseases, but nature has also leveraged the rigid-repeating structure of amyloids to develop functional

macromolecular structures in various biological systems. Their functional forms play vital roles in structure, storage, signaling, and information processing across many species, including bacteria, fungi, and mammals. Well-known examples of functional amyloids in nature include their roles as structural elements in forming extracellular structures that provide support and protection. For instance, curli fibrils found in *Escherichia coli.,* formed by CsgA protein which help bacteria adhere to surfaces and form biofilms. Another structural functional amyloid is Chaplins, a group of amyloidogenic proteins required for the aerial development of filamentous *Streptomyces coelicolor*, assisting in forming aerial hyphae, which allow the bacteria to grow above the surface (Sawyer et al., 2012). Similarly, EAS Hydrophobins, amphiphilic proteins secreted as soluble monomers by the fungus *Neurospora crassa*, can self-assemble into amyloid fibrils called rodlets, which facilitate spore formation. These rodlets laterally assemble to form amphiphilic amyloid monolayers at hydrophobic: hydrophilic interfaces, enabling the reduction of surface tension, spore dispersal and attachment to hydrophobic surfaces (Macindoe et al., 2012). In mammals, a functional amyloid structure formed by the Pmel17 protein is involved in melanin synthesis by templating and accelerating melanin formation in melanocytes, while also sequestering toxic intermediates during the process (Fowler et al., 2006).

Other notable roles attributed to functional amyloids are their ability to store molecules or proteins in an inert form through reversible aggregation until needed. For example, Cdc19, a pyruvate kinase enzyme in yeast, is stored in an enzymatically inactive, amyloid-like aggregated form during cellular stress and becomes active when needed (Saad et al., 2017). In humans, amyloids play functional roles in the storage of peptide hormones in secretory granules in an amyloid-like conformation for later use (Maji et al., 2009). Similarly, microcin E492, a bacteriocin peptide produced by *Klebsiella pneumoniae*, is stored in amyloid-fibril forms, resulting in a loss of its antibacterial activity, and becomes active upon fibril disassembly (Bieler et al., 2005). Another example of this storage capability is seen in prion-like amyloids in yeast, which serve as a form of heritable information carriers, contributing to the organism's ability to adapt to different environmental conditions. Such as Sup35, a yeast prion protein, plays a role in epigenetic inheritance in *Saccharomyces cerevisiae* by existing in both amyloid and non-amyloid forms. The amyloid form of Sup35 acts as an enhancer of readthrough at translation termination, enabling the expression of hidden genetic variations under specific environmental conditions and transmitted this amyloid form to progeny through non-Mendelian inheritance (Wickner et al., 1995). Beyond yeast, similar mechanisms have

evolved in a more complex organism, such as *Aplysia*, a sea slug, where the neuronal isoform of Cytoplasmic Polyadenylation Element Binding Protein (CPEB) is involved in mRNA translation and long-term memory storage by adopting an amyloid form to store information (Si et al., 2003). Additional roles of functional amyloids include their participation in signal transduction. For example, the oligomerization of HET-s prion through amyloid templating result in programmed cell death in fungus *Podospora anserina* (Riek & Saupe, 2016). Similarly, RIP1/RIP3 forms an amyloid signaling complex that initiate kinase activation and necroptosis, a form of programmed cell death in mammals (Li et al., 2012).

Furthermore, the remarkable hierarchical assembly, stability, mechanical strength, high aspect ratio, and flexibility of amyloid assemblies are being exploited to develop a broad spectrum of advanced amyloid-based nanomaterials for biomedical, environmental, and sensing applications (Table 1). The elasticity of amyloid fibrils provides a scaffold that can be decorated or modified with different sequences and modular interactions, while maintaining their structural integrity and self-assembly characteristic. This elasticity also allows functional groups to be added to certain side chains without compromising the self-assembly process, enabling the formation of variety of different fibrils with unique properties and specific interactions (Cui et al., 2019; Mankar et al., 2011; Wang et al., 2023). However, functionalizing these scaffolds with bioactive domains is challenging, since conformational transition towards a β-sheet-rich structure during fibrillation may affect the folding and conformation of the functional domain and its subsequent inactivation. This can be overcome by carefully considering the length and type of linkers, the characteristics of the amyloidogenic assembling module, and fibrillation conditions (Robang et al., 2024; Wang et al., 2023).

Amyloid assemblies, especially functional amyloids, have been used for diverse applications, including biodegradable nanocomposites, membranes for water purification, drug delivery, and hydrogel formation. Amyloid-based materials have also demonstrated potential as smart materials responsive to environmental stimuli and as biomaterial for regenerative medicine, such as scaffolds for bone and cartilage repair, and virus disinfection. Amyloids can also form nanowires and nanotubes for electrical conductivity in nanodevices. (Table 1) (Peña-Díaz et al., 2024; Solomonov et al., 2024; Wang et al., 2023; Yadav et al., 2024).

Table 1. Utilizing Amyloids for Functional Material Development

Origin	Protein	Functional Application	Reference
Escherichia coli	CsgA	Bioplastic, hydrogels, cell-specific drug delivery, regenerative tissue engineering, water purification, biosensors, biomimetic underwater adhesive, virus capturing (influenza, SARS-CoV-2), conductive films for bioelectronics	(Peña-Díaz et al., 2024)
Staphylococcus aureus	Bap	Environmental sensor	(Taglialegna et al., 2016)
Saccharomyces cerevisiae	Sup35	Antibody binding, Biocatalytic, biosensing, virus capturing (SARS-CoV-2), enhance binding affinity	(Behbahanipour et al., 2023; Behbahanipour et al., 2024; Men et al., 2018; Wang et al., 2021; Wang et al., 2019)
Milk	β-Lactoglobulin	Aerogels for water purification	(Peydayesh et al., 2020)
Egg white	Lysozyme	Hydrogel, Organic solvent nanofiltration membranes	(Seth et al., 2023; Wu et al., 2020)
Peanut and Sunflower	Nut and oilseed proteins	Membranes for water purification from toxic heavy metals	(Soon et al., 2022)

4. Prion and Prion-Like Proteins

4.1. Prions

Prions are a class of proteins that can switch between different conformations, adopting multiple stable states, where at least one is self-propagating and typically corresponds to an amyloid or amyloid-like structure (Saad & Jarosz, 2021; Wang & Ventura, 2020). Moreover, their self-templating conformation can induce other normal identical proteins to transform into the same misfolded form through a template-directed conformational change and make a basis for prion-based inheritance (Fraser, 2014; Saad & Jarosz, 2021). This allows prions to transmit information across cellular generations outside of traditional genetic inheritance, spreading within an organism and, in specific contexts, between individuals (Harbi & Harrison, 2014). When prions possess a pathogenic conformation, they can lead to prion-related diseases, such

as Creutzfeldt-Jakob disease in humans, bovine spongiform encephalopathy and scrapie in animals (Johnson, 2005). Prions can also act as cellular memory across generations through transmission of adaptive responses to environmental changes even after the original inducing signal has dissipated. Despite their inherent stability and heritable conformation, some prions can revert their self-propagating states under certain cellular conditions. Therefore, prion formation and disassembly can be influenced by environmental stimuli such as pH changes, nutrient availability, and oxidative stress, making them responsive elements in adaptive signaling pathways (Saad & Jarosz, 2021).

Initially sequence analysis for yeast prion proteins revealed the presence of long domains rich in intrinsically disordered regions (IDRs) of low complexity, which are enriched in polar and uncharged amino acids such as asparagine (Asn), glutamine (Gln), tyrosine (Tyr), serine (Ser), and glycine (Gly), while being depleted in hydrophobic residues. These regions, known as prion domains (PrDs), are necessary and sufficient for prions to adopt various conformations, self-template, and self-aggregate into β-sheet-rich structures prone to forming amyloid fibrils. Subsequent proteome analyses have identified similar regions in proteins across a wide range of organisms, from prokaryotes to eukaryotes, including mammals, referred to as prion-like domains (PrLDs). These so-called prion-like proteins account for approximately 1% of the total human proteome. IDRs also allow prions to engage in phase separation and multivalent interactions, forming dynamic liquid-like droplets or gel-like assemblies within cells (King et al., 2012; Ross & Cascarina, 2023; Ross et al., 2005; Saad & Jarosz, 2021).

4.2. Prion-Like Proteins

Prion-like proteins despite sharing structural characteristics with prions, especially in having IDRs that are key to their flexibility in adopting diverse functional structures and forming stable assemblies, they do not always show the same self-propagating ability. These proteins are particularly enriched in RNA or DNA-binding proteins and play essential physiological roles in cellular functions, including binding, regulation, signaling, and formation of membraneless organelles. For example, the prion-like MAVS protein in humans assembles upon viral RNA detection to maintain an antiviral response, or the Balbiani body in oocytes, particularly in *Xenopus*, relies on prion-like assemblies of Xvelo protein to support embryo development (Harrison & Shorter, 2017; Saad & Jarosz, 2021).

Moreover, Prion-like proteins can contribute to the onset and progression of neurodegenerative diseases and cancer through the propensity of their PrLDs for aggregation, self-templating, and

phase separation. For example, TDP-43 aggregation is associated with Amyotrophic Lateral Sclerosis (ALS) and frontotemporal dementia (FTD), FET proteins (FUS, EWSR1, and TAF15) are linked to both neurodegenerative diseases and oncogenesis, and hnRNPA1 and hnRNPA2B1 are implicated in multisystem proteinopathies (Bartolomé-Nafría et al., 2024; Harrison & Shorter, 2017; Vazquez-Sanchez et al., 2024). Recently, our group identified that the interplay between coiled-coil (CC) motifs and low-complexity, glutamine-rich sequences in 20 human prion-like proteins may play a key role in providing functional flexibility, especially in cellular regulation and transcription processes, while also facilitating amyloid transitions, thereby highlighting their dual roles in health and disease (Batlle et al., 2021; Behbahanipour et al., 2021).

4.3. Differences Between Prion-Like Domains and Classical Amyloid Stretches

PrLDs and classical amyloid stretches both play a role in protein aggregation, but they differ in their structures and functions. Classical amyloid stretches known as amyloid-prone regions (APRs) or hot spots (HS), are typically short (5-15 residues) and are rich in aliphatic hydrophobic and aromatic amino acids such as valine (Val), isoleucine (Ile), leucine (Leu), tryptophan (Trp), phenylalanine (Phe), and tyrosine (Tyr). These regions typically lack polar and similarly charged amino acids, including arginine (Arg), lysine (Lys), aspartic acid (Asp) and glutamic acid (Glu), as well amino acids such as proline (Pro) and glycine (Gly) (De Groot et al., 2005; López de la Paz & Serrano, 2004; Monsellier et al., 2008). These segments directly induce aggregation by forming stable, rigid amyloid assemblies. These assemblies rely on strong interactions, including hydrogen bonds within aligned β-sheets that stabilize the amyloid structure through a ‘steric zipper’ mechanism.

Unlike classical amyloid stretches, PrDs and PrLDs are larger with minimum length of about 60 amino acids. These domains are rich in polar and aromatic residues (e.g., Tyr, Ser, Gln, Asn, and Gly). Therefore, their cryptic amyloid propensity results from many weak interactions distributed throughout this long region, allowing them to form amyloid structures under certain conditions (Alberti et al., 2009; Cristina Batlle et al., 2017; Toombs et al., 2010; Toombs et al., 2012). Studies have also discovered that repeating certain triplet motifs with tyrosine at the center play an essential role in PrLDs, especially through π-π (aromatic) interactions that give them a propensity to form amyloid-like structures (Kato et al., 2012; Kwon et al., 2013). These findings led to identification of the expanded motifs in PrLDs, with aromaticity as a defining feature, known as Low-complexity Aromatic-Rich Kinked Segments (LARKS) (Hughes et al.,

2018). These segments allow PrLDs to form highly packed cross-β structures through weak, reversible interactions due to their polar residues. This characteristic allows prion-like proteins easily to self-assemble and disassemble, functioning as a 'Velcro' due to the transient interactions. This flexibility and dynamic behaviour in LARKS attributed to the kinks due to the high levels of glycine and aromatic residues, especially tyrosine. These kinks let the protein backbone form close contacts, stabilized by π-π interactions from tyrosine, with an additional support from Van der Waals or hydrogen bonds between the sheets (Figure 5). This unique structure has also lower solvation energy compared to a classical steric zipper, making it more accessible to water and allowing the assembly to disassemble easily. This dynamic nature makes PrLDs essential for cellular functions, like the formation of membraneless organelles, while classical amyloid stretches are more rigid and prone to irreversible aggregation, typical of disease-related amyloids (Hughes et al., 2018).

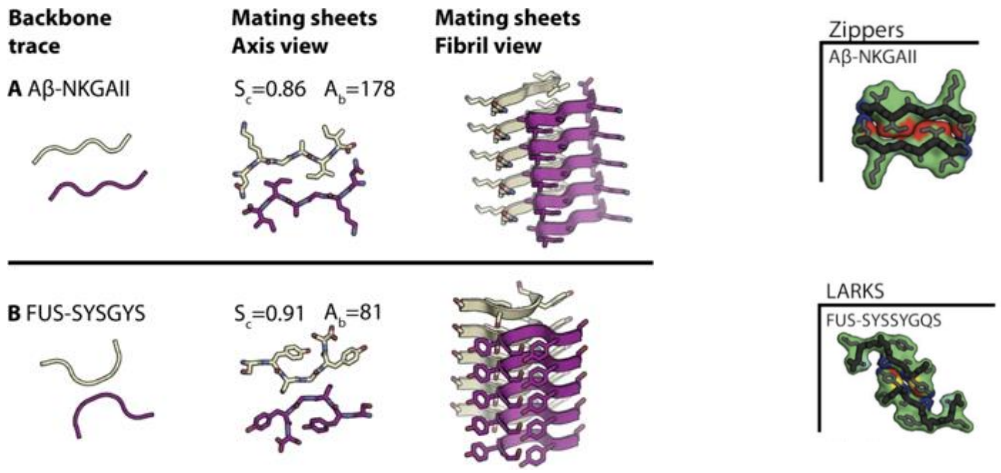

Figure 5. Structural comparison of LARKS and steric zipper. (A) Classical steric zipper from an amyloid-β peptide segment (B) FUS LARKS structure. Both structures are composed of two mating β-sheets, shown in purple and yellow. Left column: Backbone trace representation of the mated β-sheets. Second column: Atomic structure of the mating sheets viewed along the fibril axis from the end. The values represent the shape complementary score (S_c) and buried solvent-accessible area (A_b), which quantify interaction and surface burial. Third column: Cartoon representations of paired β-sheets viewed nearly perpendicular to the fibril axis. Carbon atoms are shown in purple or yellow, nitrogen in blue, and oxygen in red. Fourth column: The molecular surface, depicted in green, highlights structural motifs of the mating sheets, with red shading indicating stronger binding, yellow for intermediate, and blue for weaker binding affinities. Adapted from (Hughes et al., 2018). Reprinted with permission from Science/AAAS.

4.4. Prion-Inspired Nanomaterials

The inherent capacity of PrDs for self-assembly is generally coupled with one or more fused globular domains, which retain their functional roles within the structure. In this modular setup,

the original globular domain can be substituted with any desired functional protein without compromising the fibrillation propensity. Unlike traditional amyloids, prion and prion-like proteins show slower aggregation rates, enabling better control over the aggregation process and allowing proper folding of fused globular domains (Wang et al., 2019; Wang & Ventura, 2020). They also offer reversible processes, enabling materials to 'remember' environmental conditions and dynamically adapt, which is useful in smart biomaterials, memory storage devices, and adaptable bioengineering scaffolds, including LLPS-based materials.

In this context, yeast prion domains have been extensively exploited to develop nanomaterials based on natural prion domains tailoring function such as biosensing, catalysis and molecular recognition. Sup35 PrD is among the first instances of using natural prion domains that have been used to build prion-inspired nanomaterials such as bifunctional amyloid nanowires and improved biosensors, surpassing traditional immunodetection systems (Men et al., 2009; Men et al., 2010). Another yeast prion domain, Ure2p PrD, exploited to develop PrD-based enzyme immobilization system through fusion with enzymes like alkaline phosphatase, and horseradish peroxidase to produce enzymatic fibrils and catalytic microgels (Zhou et al., 2015; Zhou et al., 2014). PrD of Sup35 has also fused to enzymes like xylanase A, β-xylosidase, and aldose sugar dehydrogenase to develop fibrils for biocatalytic cascades, facilitating sequential enzymatic reactions. That appears practical for complex biochemical applications (Schmuck et al., 2019). PrDs of Sup35 and Ure2p fused to a dimeric form of the Z-domain, a high-affinity IgG-binding domain from *staphylococcal protein A*, resulting in Sup35p-ZZ and ZZ-Ure2p fibrils with high antibody-capturing capacity (Schmuck et al., 2017). This approach also suggests a potential high-yield antibody purification using yeast-based system (Schmuck et al., 2018). Similarly, HET-s PrD fused with rubredoxin, a redox protein that serves as an electron carrier, form a protein-only redox biofilm. This biofilm efficiently facilitates electron transfer for catalytic processes, like oxygen reduction, and offering potential for use as an effective bioelectrodes (Altamura et al., 2017).

In this context, PrLD of FUS fused with fluorescent proteins show how low complexity amino acid composition, hydrophobic tags, and environmental conditions can affect the rate and control of assembly (An et al., 2017). Also, PrLDs facilitate the formation of phase-separated microreactors from low complexity domain fused to globular proteins (Faltova et al., 2018; Küffner et al., 2020). In general, prion-inspired materials hold significant potential in

nanotechnology to create biocompatible, degradable, and multifunctional nanomaterials with a wide array of applications from biosensing to catalysis.

Recently, our group has devoted substantial efforts to developing functional amyloids, employing two strategies that harness the unique properties of the amino acid composition in prion domains. The first strategy focuses on designing synthetic peptides based on well-known motifs [Q/N/G/S]-Y-[Q/N/G/S] in PrLDs. These minimalist polar binary peptides are engineered with intrinsic amyloid and redox properties, facilitating the formation of stable β-sheet-rich, self-assembling nanofibrils (Diaz-Caballero et al., 2018). Building on this, pH-responsive peptides composed of tyrosine and histidine were designed to form reversible hydrogels with both hydrolytic and electrocatalytic functions (Díaz-Caballero et al., 2020).

The second strategy, which forms the foundation of this thesis, leverages "soft amyloid core (SAC)" technology, using cryptic amyloid sequences within prion domains to form amyloid fibrils (Figure 6) (Fernández et al., 2017; Sant'Anna et al., 2016). SAC peptides that are more polar and longer than classical amyloid peptides, allowing the expression of functional fusion proteins without losing their self-assembly ability. Using this approach, our group successfully developed a range of functional amyloids with activities such as catalysis, fluorescence, and antibody capture (Wang et al., 2021; Wang et al., 2019). It has also been shown that by adjusting the length of the linker between SAC peptides and globular domains, amyloid-like oligomers can be developed to specifically target cancer cells for methotrexate delivery (W. Wang et al., 2020).

4.5. Soft Amyloid Cores in Prion Domains and Their Use in Nanomaterials

PrDs, as discussed in the previous section, are typically over 100 residues, rely on weak, dispersed interactions for self-assembly. Therefore, the length of PrDs may hinder solubility and stability, especially when fused to smaller proteins. Studies suggest that specific stretches within PrDs and PrLDs with high amyloid propensity are sufficient to drive aggregation (Cristina Batlle et al., 2017; Fernández et al., 2017; Sant'Anna et al., 2016).

Structural analysis of 7-residue segment GNNQQNY from Sup35 PrD revealed a steric zipper formed by this short peptide through hydrogen bonds involving glutamine and asparagine, with tyrosine-mediated π-π contacts further stabilizing protofibril pairs (Nelson et al., 2005). The surrounding residues in cross-β spine formation also significantly influence the dynamic nature of assembled structures. Our group's studies confirm previous findings, termed these short

sequences within PrDs as soft-amyloid cores (SACs), which can trigger structural transitions in prion proteins, forming cross-β structure with less hydrophobicity than pathogenic amyloids (C. Batlle et al., 2017; Fernández et al., 2017; Sabate et al., 2015; Sant'Anna et al., 2016). These longer, more polar SAC aggregate only under specific conditions, effectively balancing solubility with self-assembly capabilities. The prion-like behaviour of SAC suggests that they could replace full PrD for controlled assembly in fusion proteins. The potential of SAC in engineered nanomaterials has been demonstrated by previous work from our group (W. Wang et al., 2020; Wang et al., 2021; Wang et al., 2019).

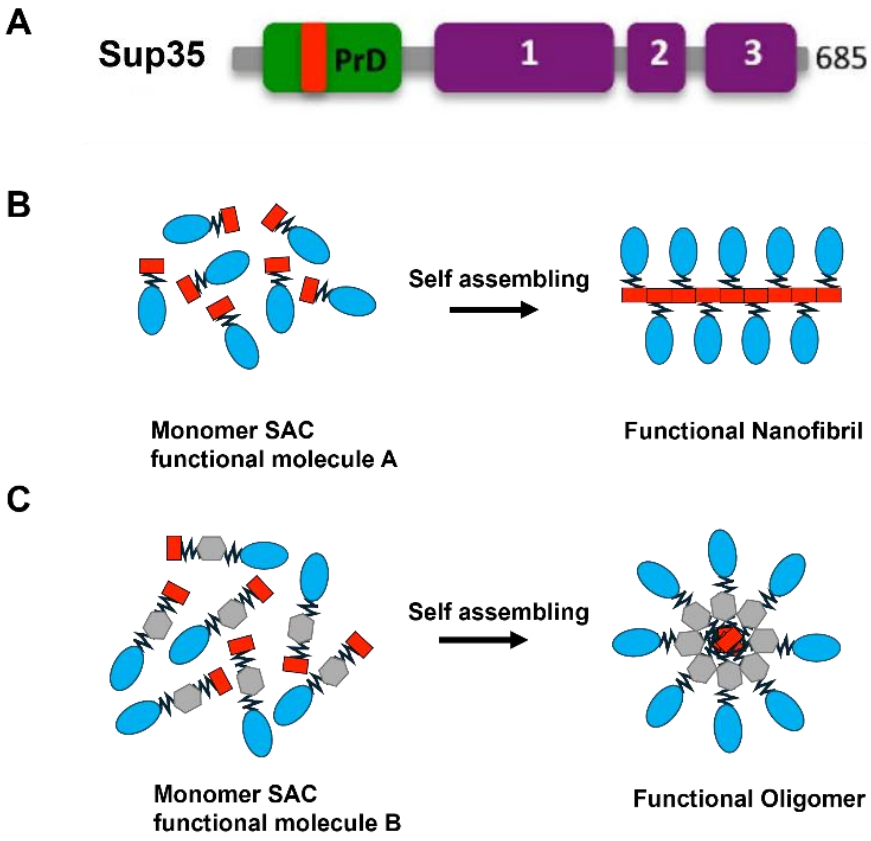

Figure 6. Schematic diagram of the construction of functional protein nanofibril and oligomer by using soft amyloid core (SAC) technology and self-assembly. (A) Sup35 sequence, including Prion domains, is shown in green, and the predicted 21-residue SAC within the prion domain is shown in red (Sant'Anna et al., 2016). (B) and (C) In the finalized functional nanofibrils and oligomers, the SAC serves as a skeleton, supporting a large number of functional molecules of interest. SAC indicated in red, linker in black/gray, and functional protein of interest in blue.

5. Targeting Severe Acute Respiratory Syndrome Coronavirus 2

With the emergence of the Severe Acute Respiratory Syndrome Coronavirus 2 (COVID-19) pandemic during this doctorate, we adapted the SAC strategy to develop two distinct nanomaterials with potential neutralizing activity against SARS-CoV-2, aiming at developing potential biotechnological tools for present and future pandemic challenges. These nanomaterials include insoluble nanofibrils, discussed in Chapter 1 (Behbahanipour et al., 2024), and soluble oligomers, discussed in Chapter 2 (Behbahanipour et al., 2023).

SARS-CoV-2 is a positive-sense single-stranded RNA virus belonging to the Coronaviridae family, responsible for the COVID-19 pandemic, with major health and economic impacts. It primarily targets the human respiratory system but can expand and affect other organs, causing severe complications especially in high-risk groups. Its structural proteins include the spike (S), membrane (M), envelope (E), and nucleocapsid (N) proteins (Machhi et al., 2020). Among these, the S protein is a transmembrane glycoprotein that plays a key role in viral entry by interacting with human angiotensin-converting enzyme 2 (hACE2) receptor, making it a key target for vaccines, antibodies, and innovative nanomaterial-based approaches. The structure of the S protein is a clover-shaped homotrimer, with each of its three protomers consisting of an S1 head for receptor recognition on host cells and a membrane-anchored S2 stalk containing the fusion machinery. The S1 region is composed of the N-terminal domain (NTD), C-terminal domain (CTD), and receptor-binding domain (RBD). The RBD adopts "up" (receptor-accessible) and "down" (receptor-inaccessible) conformations, facilitating binding to hACE2 and initiating cell entry (Mittal et al., 2020).

The majority of SARS-CoV-2 antiviral strategies aim for direct inhibition of viral entry by disrupting viral structures or targeting the viral S protein and blocking its interaction with ACE2 receptor, through different nanomaterials like silver nanoparticles (AgNPs) or biologics such as monoclonal antibodies (mAbs), ACE2 decoys, peptides, and small molecules (Cao et al., 2020; Focosi et al., 2022; Havranek et al., 2023; Jeremiah et al., 2020; X. Wang et al., 2020). The prion-inspired nanoparticles discussed in this thesis, namely OligoBinders and nanofibrils, also function through the direct primary inhibition of SARS-CoV-2 by targeting its RBD. Compared to conventional SARS-CoV-2 antiviral strategies, prion-inspired nanoparticles offer notable advantages, including modularity, biocompatibility, controlled self-assembly, multivalency, high surface-to-volume ratio, and stability (Díaz-Caballero et al., 2021; Wang et al., 2021; Wang et al., 2019). Additionally, amyloid-like nanofibrils, on the other hand, provide robust, self-assembled coatings than enable environmental SARS-CoV-2

capture via selective virus trapping. Depends on the specific application and the required balance between stability, biocompatibility, and functional versatility, prion-inspired materials may serve as a promising alternative biomaterial with antiviral properties.

Research objectives

The objective of this doctoral thesis is to develop bioengineered prion-inspired protein assemblies to neutralize SARS-CoV-2. Using the SAC peptide from the Sup35 yeast prion domain, previously shown by our group to recapitulate the entire prion domain's propensity to form various functional, protein-only materials, we built on this foundation to present a modular and generalizable method for viral naturalization. In **Chapter 1**, insoluble amyloid-based nanofibrils with high affinity for the virus's spike protein have been developed to effectively capture and neutralize the virus, with potential applications as antiviral coatings for surfaces to reduce virus transmission. In **Chapter 2**, "OligoBinders," soluble modular oligomeric nanoparticles that prevent the virus from binding to human cell receptors, are presented as a promising therapeutic approach.

Chapter 1: Bioengineered self-assembled nanofibrils for high-affinity SARS-CoV-2 capture and neutralization

The rapid transmission of SARS-CoV-2 via contaminated surfaces, which can persist for days and lead to subsequent self-inoculation, demonstrates that traditional antiviral coatings, while helpful, often suffer from non-selectivity and potential toxicity, making them unsuitable for many public and healthcare settings. The current work of this chapter was inspired by the need for safe, selective, biocompatible and highly effective materials capable of neutralizing SARS-CoV-2 on surfaces, which could add a key layer of protection in environments at risk of viral spread. To this aim, we used a prion-based nanofibril platform that exploits only the 21-residue SAC peptide from the Sup35 yeast prion domain as an assembling module, sufficient to promote the fibrillation of its fused globular domain. We engineered insoluble nanofibrils by fusing this scaffold with two different high-affinity SARS-CoV-2 binding proteins (LCB1 and LCB3). The resulting self-assembled nanofibrils, with specific binding sites for the SARS-CoV-2 spike proteins at its receptor-binding domain (RBD), are capable of preventing the virus from attaching to ACE2 receptors on human cells, effectively neutralizing it even after long time incubation at room temperature. We also showed that the final morphology of these self-assembled nanofibrils is modifiable by adjusting the salt concentration in the initial self-assembly buffer, which can also influence their functionality.

The specific main objectives of this chapter are:

- Developing biocompatible and stable antiviral materials to combat SARS-CoV-2, particularly to prevent environmental transmission via surfaces, by exploiting the SAC peptide fused to two high-affinity binders (LCB1 and LCB3) that specifically target the virus's RBD.
- Evaluating the ability of these nanofibrils to prevent SARS-CoV-2's RBD interaction with the ACE2 receptor in cell models, utilizing virus-like particles.
- Demonstrating how varying salt concentrations can modify the nanofibril assembly process, enabling fine-tuning of the structural characteristics and virus-binding efficiency of the nanofibrils.
- Exploring the coating capacities of nanofibrils on surfaces to create antiviral coatings that can capture and neutralize SARS-CoV-2 in wet environments, reducing the risk of surface-based transmission.
- Building up a molecular model for Sup35-LCB1 nanofibrils to visualize their structural organization.

Chapter 2: OligoBinders: Bioengineered Soluble Amyloid-like Nanoparticles to Bind and Neutralize SARS-CoV-2

The need for alternative SARS-CoV-2 neutralization strategies, particularly as immunity from vaccines can decrease over time and antibody therapies face limitations in stability and their delivery. The current work of this chapter focusses on developing bioengineered nanoparticles, termed "OligoBinders," inspired by amyloid-like structures to create stable, high-surface-area soluble oligomeric nanoparticles that could mimic and enhance antibody functions. By using a modular assembly approach using SAC peptide combined with dihydrofolate reductase (DHFR) forms the foundational structure for oligomerization, we designed nanoparticles that incorporate high-affinity miniproteins (LCB1 and LCB3) to the C-terminal end of this construct, which bind to the virus's RBD, effectively blocks the interaction with the ACE2 receptor on human cells, thereby preventing viral entry with strong binding affinity in the picomolar range through in vitro experiments using SARS-CoV-2 virus-like particles. Engineered nanoparticles shows stability in human plasma and are non-toxic to human cells. This approach demonstrates potential applications in diagnostics, therapeutic agents or as prophylactic solutions such as nasal sprays.

The specific goals of this chapter are:

- Incorporating two high-affinity binders (LCB1 and LCB3) that specifically target the virus's RBD, into the C terminal end of a SAC-DHFR construct to form spherical, soluble oligomeric nanoparticle with a high density of functional binding domains for SARS-CoV-2, as an alternative therapeutic and diagnostic approach.
- Evaluating the ability of these soluble oligomers to inhibit the interaction between SARS-CoV-2's RBD and the ACE2 receptor in cell-based models, utilizing virus-like particles, which is critical for viral entry.
- Demonstrating the stability of the oligomeric nanoparticles in plasma, ensuring their potential durability within biological systems
- Assessing their toxicity to confirm biocompatibility and safety for therapeutic applications.

CHAPTER 1:

Bioengineered self-assembled nanofibrils for high-affinity SARS-CoV-2 capture and neutralization

Molood Behbahanipour, Susanna Navarro, Oriol Bárcenas, Javier Garcia-Pardo, Salvador Ventura *

Journal of Colloid And Interface Science

2024

https://doi.org/10.1016/j.jcis.2024.06.175

Journal of Colloid and Interface Science 674 (2024) 753–765

Contents lists available at ScienceDirect

Journal of Colloid And Interface Science

journal homepage: www.elsevier.com/locate/jcis

Bioengineered self-assembled nanofibrils for high-affinity SARS-CoV-2 capture and neutralization

Molood Behbahanipour, Susanna Navarro, Oriol Bárcenas, Javier Garcia-Pardo, Salvador Ventura *

Institut de Biotecnologia i de Biomedicina (IBB) and Departament de Bioquímica i Biologia Molecular; Universitat Autònoma de Barcelona, 08193 Bellaterra (Barcelona), Spain

HIGHLIGHTS

- Modular bioengineered nanofibrils neutralize SARS-CoV-2 virus-like particles.
- Recombinant protein subunits spontaneously assemble into functional fibrils.
- The assembled amyloid-like nanofibrils are biocompatible.
- Mesoscopic structure and activity of the protein assembly are easily modulated.
- Surfaces coated with nanofibrils capture SARS-CoV-2 Spike in wet environments.

GRAPHICAL ABSTRACT

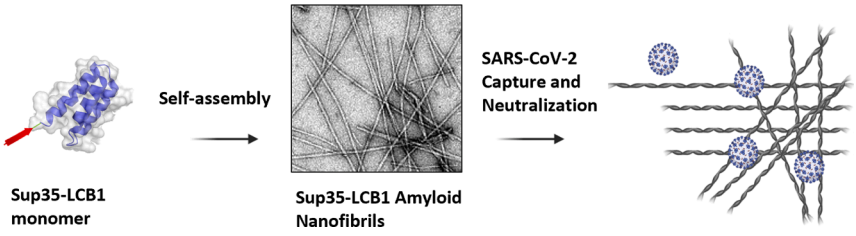

ARTICLE INFO

Keywords:
Amyloid Fibrils
SARS-CoV-2
Supramolecular Assemblies
Antiviral Biomaterials
Functional Polymers

ABSTRACT

The recent coronavirus disease 2019 (COVID-19) pandemic caused by the severe acute respiratory syndrome coronavirus 2 (SARS-CoV-2) has spurred intense research efforts to develop new materials with antiviral activity. In this study, we genetically engineered amyloid-based nanofibrils for capturing and neutralizing SARS-CoV-2. Building upon the amyloid properties of a short Sup35 yeast prion sequence, we fused it to SARS-CoV-2 receptor-binding domain (RBD) capturing proteins, LCB1 and LCB3. By tuning the reaction conditions, we achieved the spontaneous self-assembly of the Sup35-LCB1 fusion protein into a highly homogeneous and well-dispersed amyloid-like fibrillar material. These nanofibrils exhibited high affinity for the SARS-CoV-2 RBD, effectively inhibiting its interaction with the angiotensin-converting enzyme 2 (ACE2) receptor, the primary entry point for the virus into host cells. We further demonstrate that this functional nanomaterial entraps and neutralizes SARS-CoV-2 virus-like particles (VLPs), with a potency comparable to that of therapeutic antibodies. As a proof of concept, we successfully fabricated patterned surfaces that selectively capture SARS-CoV-2 RBD protein on wet environments. Collectively, these findings suggest that these protein-only nanofibrils hold promise as disinfecting coatings endowed with selective SARS-CoV-2 neutralizing properties to combat viral spread or in the development of sensitive viral sampling and diagnostic tools.

Abbreviations: COVID-19, coronavirus disease 2019; SARS-CoV-2, severe acute respiratory syndrome coronavirus 2; RBD, receptor-binding domain; ACE2r, angiotensin-converting enzyme 2 receptor; VLPs, virus-like particles; S protein, viral spike protein; SAC, soft amyloid core; IC_{50}, half-maximal inhibitory concentration; CD, circular dichroism; Na-PB, sodium phosphate buffer; BCA, bicinchoninic acid assay; Th-T, thioflavin T; CR, congo red; ATR-FTIR, attenuated total reflectance Fourier-transform infrared; NS-TEM, Negative-Stain Transmission Electron Microscopy; SDS, sodium dodecyl sulfate; APRs, regions prone to aggregation; SD, standard deviation; RT, room temperature; PVDF, polyvinylidene difluoride; PPI, protein–protein interaction.

* Corresponding author.
E-mail addresses: Molood.Behbahanipour@uab.cat (M. Behbahanipour), Susanna.Navarro.Cantero@uab.cat (S. Navarro), Oriol.Barcenas@uab.cat (O. Bárcenas), Javiergarciapardo@msn.com (J. Garcia-Pardo), Salvador.Ventura@uab.cat (S. Ventura).

https://doi.org/10.1016/j.jcis.2024.06.175
Received 19 February 2024; Received in revised form 10 June 2024; Accepted 23 June 2024
Available online 24 June 2024

1. Introduction

The coronavirus disease 2019 (COVID-19) pandemic has sparked an unprecedented global research effort to combat the severe acute respiratory syndrome coronavirus 2 (SARS-CoV-2). This multifaceted crusade encompasses a diverse array of antiviral strategies aimed at mitigating disease severity, including the development of vaccines [1], antiviral drugs [2,3], convalescence plasma therapy [4,5], RNA interference [6,7], or prophylactic measures [8]. Despite all these concerted efforts, SARS-CoV-2 has caused over 6.9 million deaths since its emergence in December 2019 (~2.0 % fatality rate) [9], stressing the need for innovative approaches to address the evolving complexities of the disease. One major challenge is the rapid environmental transmission of the SARS-CoV-2, which is primarily mediated through respiratory droplets and aerosols. Recent studies have shown that the virus contained in these droplets can persist on surfaces for several days, enabling its spread through direct contact with contaminated surfaces and subsequent self-inoculation *via* touching the eyes, nose, and mouth [10–12].

Once SARS-CoV-2 reaches the host cell, a critical step for successful viral internalization in human cells is the attachment of the receptor binding domain (RBD) from the viral spike (S) protein to the angiotensin-converting enzyme 2 receptor (ACE2r), which is highly expressed in various SARS-CoV-2 target tissues, including the lungs, heart, and gastrointestinal tract [13–16]. Different strategies have been devised to disrupt this critical interaction, including the use of small chemical molecules [17], peptide inhibitors [18], monoclonal antibodies [19–22], or oligomeric nanomaterials [23] that specifically target the SARS-CoV-2 spike protein, thereby blocking its ability to bind to ACE2r and preventing viral spread.

Despite the aforementioned advances, the high transmission rates of SARS-CoV-2 and the rapid emergence of resistant strains that evade current treatments or vaccines underscore the importance of prevention in combating COVID-19 [24,25]. Consequently, the development of new coatings, designed to act as antiviral barriers against the spread of SARS-CoV-2 through fluids, is gaining traction. Various materials, such as polymers, metals (*i.e.* Cu or Zn), metal oxides (CuO, ZnO or TiO_2), and their corresponding nanoparticles, have been investigated for developing antiviral coatings on different surfaces [8,26–29]. However, these conventional approaches are often non-selective and exhibit significant toxicity [28,30,31]. As a result, alternative biomaterials with antiviral properties are being investigated [23].

Amyloid-inspired fibrils have emerged as a cost-effective and sustainable way to produce versatile biocompatible nanomaterials [32–34] with a wide range of applications, including tissue engineering [35], pH sensors [36] or synthetic catalysts [32]. These protein-based materials typically feature densely packed amyloid cores formed by hydrogen-bonded β-sheets [34,37–39]. This distinctive supramolecular architecture provides a strong internal bonded network, translating into remarkable material properties, including high Young's modulus and tensile strength [40] and, often, remarkable resistance to chemical and proteolytic degradation [41]. A key advantage of these self-assembling materials lies in the ability to incorporate specific functionalities through straightforward protein engineering techniques [42,43].

Herein, we have engineered a novel biocompatible protein material for the targeted capture and neutralization of SARS-CoV-2 using self-assembling amyloid-based nanofibrils. We exploited the self-assembly of the Sup35 yeast prion soft amyloid core (Sup35-SAC) [44], fused to two different SARS-CoV-2 RBD-binding moieties, namely LCB1 and LCB3 [45]. These globular small α-helical domains, originally designed by David Baker's lab [45], have been exploited by our group [23] and others [46–48] to generate novel molecules that bind to SARS-CoV-2 spike protein. Using a modular approach and tailoring the self-assembly conditions, we obtained a set of Sup35-LCB1/LCB3 nanofibrils with diverse supramolecular morphologies and activities. Computational modelling and experimental data indicate that Sup35-LCB1 nanofibrils possess an amyloid-like architecture. As intended, they are non-toxic and display functional binding surfaces. Accordingly, they effectively recognize SARS-CoV-2 RBD, with a half-maximal inhibitory concentration (IC_{50}) as low as ~ 6 ng/mL. The high density of binding motifs at the fibrils surface confers avidity, enabling them to neutralize the fusion of SARS-CoV-2 virus-like particles (VLPs) to the membrane of ACE2r-expressing human cells with exceptional potency. As proof-of-concept material, the Sup35-LCB1 nanofibrils were embedded in a PVDF matrix, resulting in an amyloid-based surface coating with remarkable efficacy and selectivity in trapping SARS-CoV-2 RBD.

Overall, this study introduces a novel, protein-only fibrillar nanomaterial designed to block SARS-CoV-2 spreading, demonstrating potential as an effective biocompatible antiviral surface coating.

2. Materials and methods

2.1. Protein expression and purification

To engineer constructs that express the Sup35-LCB1/3 proteins, the cDNAs encoding the LCB1 and LCB3 protein sequences were inserted into a pET28a vector. Both proteins were fused to the C-terminus of the 21-residue-long soft amyloid core of Sup35 yeast prion protein through a flexible (SGSGS) linker. Additionally, an 6x His-tag was also added to the C-terminus to facilitate nickel affinity purification. For protein expression, BL21 (DE3) *E. coli* cells were transformed with the plasmids and grown overnight in LB medium containing 50 μg/mL kanamycin. After incubation overnight at 37 °C under constant agitation, the cultures were diluted (1:100) in fresh LB medium and grown until reaching a culture with an optical density (600 nm) of 0.4. Then, Sup35-LCB1/3 expression was induced by adding 1 mM IPTG, followed by incubation at 20 °C overnight. The cells were then collected and lysed by sonication on ice in 30 mL lysis buffer (20 mM sodium phosphate buffer (Na-PB) pH 8.0, 0.3 M NaCl, 1 mM PMSF, 1 μg/mL DNase, and EDTA-free protease inhibitor Mini Tablets) per L of culture. Subsequently, cell lysates were centrifuged at 20000 rpm for 30 min at 4 °C, and the clarified supernatants were filtered through 0.45 μm low protein binding filters. The filtered samples were loaded onto a pre-equilibrated HisTrap™ FF crude column (Cytiva), previously washed with 10 column volumes (CV) of equilibration buffer (20 mM Na-PB pH 8.0, 0.5 M NaCl with 20 mM imidazole). The recombinant proteins were eluted by applying a gradient (5 CV) of the elution buffer (20 mM Na-PB pH 8.0, 0.5 M NaCl, and 0.5 M imidazole). The eluted recombinant proteins were pooled and further purified using a size exclusion chromatography in a Superdex 75 increase 10/300 GL column (GE Healthcare, USA) and 20 mM sodium phosphate pH 8.0 buffer (Na-PB). Finally, the purified proteins were flash-frozen in liquid nitrogen and kept at −80 °C until use. The purity of the purified Sup35-LCB1/3 samples was confirmed by SDS-PAGE analysis. The final protein concentrations were determined with the bicinchoninic acid (BCA) assay (Thermo Fisher Scientific, Waltham, Massachusetts, USA).

2.2. Circular dichroism (CD) spectroscopy

The far-UV CD spectra for soluble Sup35-LCB1 and Sup35-LCB3 proteins were measured in the 200–260 nm wavelength range using a Jasco J-815 CD spectropolarimeter. The samples were diluted at a concentration of 40 μM in 20 mM Na-PB buffer at pH 8 and 25 °C. The measurements were taken with a data pitch of 0.2 nm, a bandwidth of 1 nm, and 20 accumulations at a scanning speed of 100 nm/min. To follow the changes in the CD signal during the aggregation reaction for both Sup35-LCB1 and Sup35-LCB3, we measured the CD spectrum of 20 μM samples on days 0, 3, and 6. This was done under three different Na-PB conditions.

2.3. Formation of protein nanofibrils

Fibrillation reactions for Sup35-LCB1 and Sup35-LCB3 were carried out at final protein concentration of 500 μM (5.28 mg/mL). Prior to the reaction, samples were filtered through 0.22 μm low protein binding filters and then immediately diluted in Na-PB at three different concentrations (20 mM, 150 mM, or 300 mM), at pH of 8.0 or in double-distilled Milli-Q™ water. The solutions were incubated at 37 °C with agitation at 600 rpm for 6 days. Afterwards, they were centrifuged for 1 h at 16000 g at 10 °C to separate insoluble fibrils from the soluble supernatant. The final protein concentrations in the supernatant were determined by the BCA assay and subtracted from the initial protein concentration (500 μM, 5.28 mg/mL) to estimate the amount of protein present in the amyloid fibrils after the incubation reaction.

2.4. Amyloid dye binding

The Sup35-LCB1/3 self-assembly into amyloid fibril at different salt concentration was evaluated using Thioflavin-T (Th-T) and Congo red (CR) dye binding assays. ThT fluorescence of the soluble protein and the self-assembled amyloid fibrils were assayed at a final protein concentration of 0.2 mg/mL and in the presence of 25 μM ThT. The fluorescence of these samples was recorded in the 460 to 600 nm range upon excitation at 445 nm using a Jasco FP-8200 spectrofluorometer (Jasco Corporation, Japan) (excitation/emission bandwidth of 5 nm).

CR spectral shift assays were performed using a SPECORD® 200 Plus spectrophotometer (Analytik Jena, Germany) to measure the absorption spectrum in the visible region (375–700 nm) for amyloid fibril suspensions (0.2 mg/mL) in the presence of the 20 μM CR dye. To determine the CR signal specific to protein binding, the absorption spectrum of only proteins was subtracted from that of proteins bound to CR. Buffers without protein were also evaluated as negative controls for both Th-T and CR assays.

2.5. Fourier transform infrared (FTIR) spectroscopy

Infrared spectra of fibrils formed in different salt conditions were collected using Bruker Tensor 27 FTIR spectrometer (Bruker Optics, USA) supplied with a Specac Golden Gate MKII ATR accessory. 50 μL of each fibril suspension was centrifuged for 1 h at 16100 g at 10 °C. Then, the pellet was resuspended in 10 μL Milli-Q water and placed on the diamond ATR crystal. Before analysis, the solvent was evaporated by using a stream of nitrogen. FTIR spectrum of all the samples was recorded between 1700 and 1600 cm^{-1} by performing 32 acquisitions at a resolution of 1 cm^{-1}. In all the cases, the spectra were corrected to remove background absorption. OPUS MIR Tensor 27 software (Bruker Optics, USA) was used for data normalization with the Min/Max normalization method. IR spectra were fitted employing automated peak fitting using the "AutoFit Peaks I Residuals" option with the "vary widths" condition for the autoscan procedure, until reaching iteration 7 and an $r^2 > 0.997$ using PeakFit package v4.12 (Systat Software, San Jose, CA). The area for each Gaussian curve was calculated in the amide I region from 1700 to 1600 cm^{-1} using the second derivative deconvolution approach. From the second derivative plot for each sample absorbance spectrum, peaks and local minima were identified and their numbers and positions were manually placed to deconvolute the absorbance spectra. Afterwards, the resulting area, amplitude and center values of the fitted bands were exported as a table and plotted.

2.6. Transmission Electron Microscopy (TEM)

The size and morphology of the Sup35-LCB1/3 self-assembled fibrils prepared under different salt concentration were examined using negative staining transmission electron microscopy (NS-TEM). All the samples were prepared by placing 10 μL of fibril suspensions (1:10 dilution) on carbon-coated copper grids. The excess of solution was removed after 10 min incubation with filter paper strips. The samples were then negatively stained with 10 μL of uranyl acetate solution (2 % w/v) for 1 min. The grids were imaged with a 120 kV JEOL 1400 transmission electron microscope (JEOL Ltd, Japan). Images of representative amyloid fibrils were acquired with a CCD GATAN ES1000W Erlangshen camera (Gatan Inc., USA). Fibrils width measurements were done in random positions of the grids using ImageJ software (National Institutes of Health, Bethesda, Maryland, USA). The obtained width average was a result of 30 individual measures for each sample. For group-wise comparisons, a two-way ANOVA test of the data was performed using GraphPad Prism V6.01 [49].

2.7. Sup35-LCB1/3 fibrils resistance to sodium dodecyl sulfate (SDS)

0.8 μg/μL of Sup35-LCB1 and Sup35-LCB3 fibrils, formed under three different Na-PB conditions, were taken after they had been separated from their soluble protein counterparts at the end of the fibrillation. These fibrils were then incubated in the absence and presence of 0.1 % and 1 % SDS for 30 min at 25 °C. After incubation, the samples were centrifuged at 16100 g for 45 min at 20 °C to separate the fibrillar remains from any dissociated or soluble component. Subsequently, 10 μL of the supernatants from both the control and treated samples were mixed with an equal volume of loading buffer. The mixture was then boiled for 10 min at 95 °C. Subsequently, 12 μL of each sample was loaded onto a 15 % SDS-PAGE gel for analysis.

2.8. Modelling of Sup35-LCB1 nanofibrils

Fibrils were built with a 2° left angle twist, maintaining a 4.8-angstrom translation over the Z-axis between the monomers. The LCB1 domain was extracted from the Cryo-EM structure of the mini-binder bound to the SARS-CoV-2 Spike protein (pdb entry 7JZU). However, due to the relatively low resolution of the structure (3.1 Å), the sidechains of some amino acids were not determined. Therefore, the structure was refined using the ColabFold Google notebook [50] and the original pdb as a structure template. The obtained structure contained all residues' sidechains, maintaining the structure of the original pdb. The functionalized fibril models were built from hexameric subunits of the LCB1 domain bound to the amyloid fibril through the linker. The subunit's architecture maintained equidistant and maximum spacing between the LCB1 domains and the core of the fibril. An imaginary circle around the fibrils' extreme was populated with the globular domains using sine and cosine theorems. Afterwards, the globular domains were connected to the fibril using the linker sequence, and the hexameric subunits were concatenated 15 times along the z axis to build the final fibril model, consisting of 90 monomers. Finally, the complete model was energy minimized and analyzed for steric clashes. The process of fibril building was carried out using instructions written in Python and imported into ChimeraX [51]. The linker sequences were modelled into the final structure using the loop modelling capabilities of the MODELLER suite [52]. Finally, the structure was energy-minimized using GROMACS (v. 2022.3) [53] with the AMBER99SB-ILDN [54] force field and analyzed with the PROCHECK package [55].

2.9. Cytotoxicity assay

The effect of the Sup35-LCB1 nanofibrils on the cell viability of HeLa cells was investigated by performing a resazurin-based assay using the PrestoBlue TM Cell Viability Reagent (Invitrogen) as described in other articles [56–58]. In brief, HeLa cells (American Type Culture Collection, ATCC) were cultured in Dulbecco's Modified Eagle Medium (DMEM, Gibco, Invitrogen, USA) supplemented with 10 % (v/v) fetal bovine serum in 5 % CO_2 atmosphere at 37 °C. HeLa cells were plated out in a 96-well plate at a density of 3.5×10^3 cells/well in 100 μL complete DMEM. A reference well containing only the culture media was maintained as a control condition. The plate was incubated at 37 °C in 5 %

CO_2 for 24 h to allow for cell growth and adhesion to the culture plates. Then, Sup35-LCB1 fibrils in different salt conditions, diluted to the appropriate final concentration in DMEM (20, 50, and 100 μg/mL), were added to cells and incubated for 72 h in triplicates. The control group received the same volume of sterile PBS pH 7.0 as vehicle control. After incubation, 10 μL of the PrestoBlue cell viability reagent (Invitrogen) was added to each well and the plate was further incubated for 30 min. Cell viability was determined by recording fluorescence emission at 615 nm, with an excitation wavelength at 531 nm using a Victor III Multilabel Plate Reader (Perkin Elmer). Statistical analysis of the data, specifically checking for minimal differences, was performed using GraphPad Prism V6.01 [49], and the results were determined to be not statistically significant.

2.10. Interference of the ACE2-RBD interaction

The ability of the self-assembled Sup35-LCB1 fibrils formed in different salt condition to inhibit spike RBD-ACE2 interaction was evaluated using the Lumit™ SARS-CoV-2 Spike RBD: hACE2 Immunoassay (Promega Biotech). This assay utilizes the principle of luminescence complementation between two nonfunctional fragments (LgBiT and SmBiT) of the reporter protein NanoBiT®, achieving a full-length functional reporter upon reconstitution. To perform the experiments, the Sup35-LCB1 amyloid fibrils were serially diluted and incubated with RBD-FC (Rabbit Fc) for 30 min prior to the addition of hACE2-FC (Mouse Fc) and Lumit Antibody Mix. After 1-hour incubation at RT, Lumit™ detection reagent was added, followed by incubation at RT for 30 min, according to the manufacturer instructions. NanoBiT® Luminescence was then recorded using a fluorescence microplate reader (Spark®, Tecan). The signal from the buffer alone was subtracted from all samples signal to discard the background signal contribution. As control conditions, reactions without the Sup35-LCB1 fibrils were also assayed. Then, all luminescence values were expressed as percentage (%) of the maximal ACE2-RBD protein–protein interaction (PPI) activity. The corresponding sample neutralization activity (%) was determined by subtracting the PPI activity from 100. The IC_{50} values were determined using GraphPad Prism V6.01 [49] and applying a non-linear regression (least squares) fitting method. The final values represent the mean of two independent experiments.

2.11. Interference of SARS-CoV-2 cell internalization

The capacity of the Sup35-LCB1 nanofibrils to capture SARS-CoV-2 and inhibit its entry into cells was evaluated by using a cell culture-based assay (Promega Biotech), which exploits split NanoLuc technology (LgBiT and HiBiT). This approach uses engineered SARS-CoV-2 virus-like particles (VLPs) containing a HiBiT protein, which can efficiently deliver this cargo into target cells expressing intracellular LgBiT. Upon successful viral entry, this process results in the emission of a luminescence due to the reconstitution of NanoLuc within the infected cells. Importantly, the genome-free nature of SARS-CoV-2 −VLPs eliminates the need for a biosafety level 3 (BSL3) facility. Moreover, the HiBiT technology provides the benefits of high sensitivity and convenience of a single-reagent-addition step to quantify membrane fusion and virus cell entry. Serial dilutions of the self-assembled Sup35-LCB1 amyloid fibrils prepared in different salt conditions were incubated with SARS-CoV-2 S(G614) HiBiT- pseudotype VLPs for 30 min at 37 °C, before adding to SARS-CoV-2 HEK293T (LgBiT) target cells. After 3 h of incubation at 37 °C, Nano-Glo® live cell reagent was added, and luminescence of the cells was measured after 15 min incubation at 37 °C. If the virus binds to the engineered nanofibers, it cannot interact with the ACE2 receptor and be internalized into the cell. This prevents the release of HiBiT in the cell cytoplasm and, thus, no luminescence is produced. The buffer alone was assayed to determine the basal luminescence signal. Then, by subtracting the baseline-corrected luminescence signal values from 100, the inhibition of SARS-CoV-2 HiBiT- pseudotype VLPs entry was calculated and expressed as a function of the maximal neutralization percentage. In order to calculate the IC_{50}, the acquired values were fitted to a non-linear regression curve using the least squares fitting equation from GraphPad Prism V6.01 [49].

2.12. Coating with Sup35-LCB1 nanofibrils

To demonstrate the coating capacities of the Sup35-LCB1 nanofibrils, we conducted a dot blot assay. In this assay we have deposited the fibrils following a pattern to depict our university logo by spotting dots with 4 μg from LCB1 fibrils onto the methanol activated polyvinylidene difluoride membrane (PDVF) (Immobilon-P transfer membranes, Merck Millipore, Germany). Then, non-specific sites were blocked by incubating the membrane in 5 % BSA in TBS-T (20 mM Tris-HCl, pH 7.4, 150 mM NaCl, and 1 % Tween-20) for 30 min at RT. Next, the membrane was incubated with RBD-YFP protein (0.54 ng/μL) dissolved in 0.1 % BSA/TBS-T (30 min, RT); this allowed the RBD-YFP to bind specifically to the coated nanofibrils on the membrane. Then, the membrane was thoroughly washed with TBS-T (3x 5 min) to remove any unbound or nonspecifically bound RBD-YFP. Thus, only RBD-YFP specifically bound to the fibrils remained on the membrane. Finally, the membrane was imaged using a ChemiDoc imaging system (Bio-Rad Laboratories).

3. Results and discussion

3.1. Design and structural characterization of soluble Sup35-LCB1 and Sup35-LCB3 proteins

Recently, the self-assembly properties of prion-like proteins have been harnessed for creating novel nanomaterials with fibrillar morphology and large surface-to-volume ratios [34,42,59–61]. These proteinaceous materials are typically customized by selecting an amyloidogenic domain that can spontaneously self-assemble into fibrils and integrating it with functional globular domains. This modular approach enables tailoring both the structural properties and biological activities of these nanomaterials.

In this study, we aimed to develop novel nanofibrils with a high density of SARS-CoV-2 binding moieties, creating a functional supramolecular scaffold with antiviral properties. We have previously demonstrated that the Sup35-SAC sequence (a 21-residue segment corresponding to residues 98–118 of Sup35 prion domain) spontaneously self-assembles into amyloid fibrils, while preserving the structural integrity and functionality of appended globular domains [62]. Here, Sup35-SAC was used as a scaffolding unit and fused to LCB1 and LCB3 domains, serving as SARS-CoV-2 binding modules (Fig. 1). A short and flexible linker (SGSGS) was used to bridge the Sup35-SAC unit and the globular LCB domains in the protein fusions. This 5-residue linker is expected to allow both Sup35-SAC self-assembly into amyloid fibrils and the proper folding of the LCB moieties.

Recombinant expression of the Sup35-LCB1/LCB3 fusion proteins in *E. coli* cells followed by metal ion affinity chromatography yielded 21 mg of purified Sup35-LCB1 and 48 mg of Sup35-LCB3 per liter of culture (**Figs. S1 and S2**). The secondary structure of the soluble Sup35-LCB1/LCB3 proteins was analyzed using far-UV circular dichroism (CD) spectroscopy. The resulting spectra (Fig. 1**C and D**) exhibited characteristic spectral minima at 209 nm and 222 nm, indicative of α-helical conformations. These spectral signatures aligned well with the calculated α-helical secondary structure contents for Sup35-LCB1 and Sup35-LCB3 monomeric proteins, which were estimated to be 49 % and 51 %, respectively, supporting the preservation of the native folded states of LCB domains within the fusion proteins.

3.2. Sup35-LCB1/LCB3 spontaneously self-assemble into functional amyloid-like structures

The soluble precursors of amyloidogenic proteins can be directed

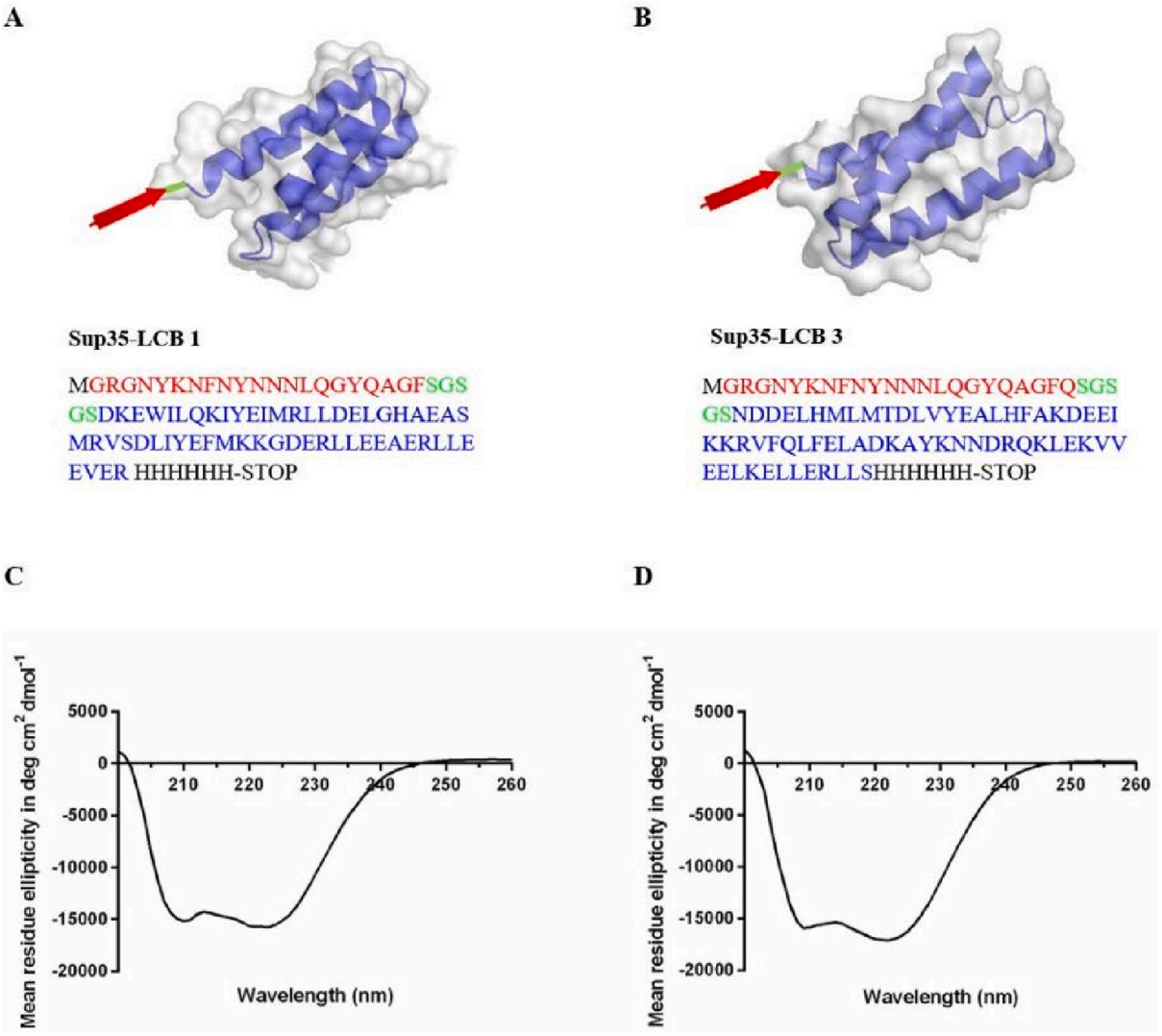

Fig. 1. Design and biophysical characterization of soluble Sup35-LCB1/LCB3 fusion proteins. (A, B) Cartoon representations and sequences of (A) Sup35-LCB1 and (B) Sup35-LCB3 fusion proteins. In these engineered proteins, the SAC of Sup35 (shown in red) is fused to either the LCB1 or LCB3 SARS-CoV-2 RBD binders (shown in blue) *via* a short S/G linker (shown in green). (C, D) Far-UV CD spectra of the purified (C) Sup35-LCB1 and (D) Sup35-LCB3 proteins recorded in the range of 200–260 nm at 25 °C in 20 mM sodium phosphate, pH 8.0, and at final protein concentration of 40 μM. (For interpretation of the references to colour in this figure legend, the reader is referred to the web version of this article.)

into distinct supramolecular structures by manipulating the assembly conditions [37,63–66]. Monomeric Sup35-LCB1/LCB3 proteins were incubated at an initial concentration of 500 μM for six days at 37 °C in varying concentrations of sodium phosphate (Na-PB) buffer at pH 8.0 (*i.e.,* 20 mM, 150 mM, and 300 mM). Unassembled monomers and prefibrillar species were removed from the reaction by centrifugation. Afterwards, protein concentrations in the insoluble fractions were estimated using the bicinchoninic acid (BCA) assay. Yields increased with increasing Na-PB concentration (**Table S1**). Fibrillation was most efficient at 300 mM Na-PB, with Sup35-LCB1 and Sup35-LCB3 yields of 58 % and 40 %, respectively, relative to the initial protein concentration in the reaction.

The amyloid-like nature of the purified protein aggregates was assessed by measuring their binding to thioflavin T (Th-T) and Congo red (CR) dyes (Fig. 2). At the same concentration, both Sup35-LCB1 and Sup35-LCB3 samples showed increased Th-T fluorescence in all assayed conditions. Notably, the Th-T fluorescence emission for the structures formed in 150 mM and 300 mM Na-PB exceeded that of those formed in 20 mM Na-PB. As expected, the soluble forms of Sup35-LCB1/LCB3 did not exhibit any Th-T binding (Fig. 2**A and B**). Similarly, the CR absorbance spectrum of the Sup35-LCB1/LCB3 aggregates displayed a clear red shift to approximately 540 nm, a characteristic feature associated with the binding of this dye to amyloid structures (Fig. 2**C and D**). This shift was consistently observed across all tested Na-PB conditions, becoming more pronounced at the highest salt concentrations.

These results collectively indicate the formation of amyloid fibrils in the Sup35-LCB1/LCB3 samples, particularly at higher salt concentrations. This suggests that charge screening may facilitate amyloid formation in these proteins. To further explore this hypothesis, we attempted to form amyloid fibrils in double-distilled Milli-Q™ water. Immediately after exchanging the buffer with water, the Sup35-LCB1/LCB3 protein solutions became cloudy and white, with a dramatic increase in the light scattering signal at 360 nm (**Fig. S3**). This indicates that protein precipitation occurs in the absence of counter ions, implying that a certain concentration of salt is necessary to sustain the solubility of the monomers and allow their slow, ordered assembly into amyloid structures.

We investigated the secondary structure content of Sup35-LCB1/LCB3 putative amyloid fibrils using attenuated total reflectance Fourier-transform infrared (ATR-FTIR) spectroscopy. The FTIR spectra

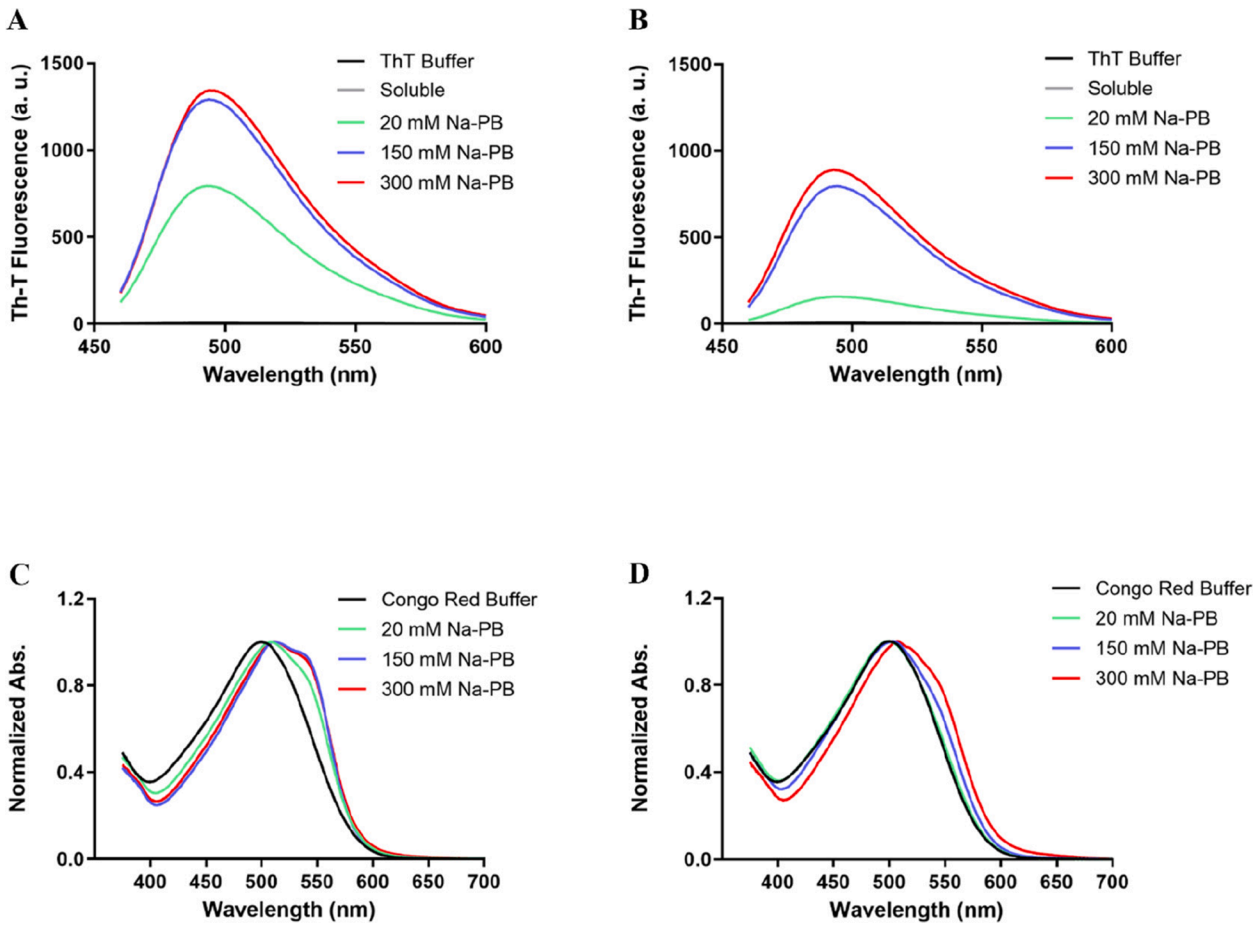

Fig. 2. Biophysical characterization of self-assembled Sup35-LCB1 and Sup35-LCB3. (A, B) Th-T fluorescence emission spectra in the presence of aggregated (A) Sup35-LCB1 and (B) Sup35-LCB3. Th-T fluorescence was recorded upon 445 nm excitation in the absence (black line) or in the presence of 0.2 mg/mL of the indicated protein samples. In (A, B), the Th-T signal of the buffer (ThT buffer) and the corresponding soluble monomeric proteins (Soluble) were evaluated as control conditions. (C, D) Congo Red (CR) normalized absorbance spectra in the absence (Congo Red Buffer) or in the presence of 0.2 mg/mL of aggregated (C) Sup35-LCB1 or (D) Sup35-LCB3. Note that CR absorbance spectra were recorded in the range from 375 to 700 nm. In figures A-D, the proteins were prepared and measured at three different Na-PB buffer concentrations, as follows: 20 mM (green solid line), 150 mM (blue solid line), and 300 mM (red solid line). (For interpretation of the references to colour in this figure legend, the reader is referred to the web version of this article.)

were recorded in the amide I region (1700 – 1600 cm^{-1}), which corresponds to the carbonyl absorption in the peptide bond. These absorbance spectra were then deconvoluted to determine the relative contributions of distinct secondary structure elements to the signal (Fig. 3). As outlined in **Table S2**, the fitted individual bands revealed three major shared contributions among the two types of assemblies at different Na-PB concentrations: ~34 % of the signal in 1626–1628 cm^{-1} range, a signature indicative of amyloid-like intermolecular β-sheets. A second major contribution occurs in the 1651/1652 cm^{-1} range, accounting for ~ 50 % of the spectra. This signal aligns well with the α-helix proportion previously detected by CD spectroscopy, suggesting the presence of properly folded LCB1/LCB3 globular domains. A third contribution, accounting for 10–20 % of the signal, is observed in the 1673–1675 cm^{-1} range, possibly arising from β-turns or random coil structures.

We monitored the secondary structure changes occurring in solution over time for both Sup35-LCB1 and Sup35-LCB3, incubated in 20 mM, 150 mM, and 300 mM Na-PB, recording the far-UV CD spectra at 0, 3, and 6 days (Fig. S4**A**). The presence of fibrils on day 6 was confirmed by microscopy (Fig. S4B).

The CD spectra of the initially soluble proteins (day 0) show two minima at 209 nm and 222 nm, indicating a predominant α-helix structure, likely contributed by the highly helical LCB1/3 domains. Interestingly, and consistent with the FTIR data, the results suggest that the globular domains remain in a helical conformation in the fraction of protein transitioning to fibrils, as the spectra of the different solutions did not exhibit major shifts toward a β-sheet-rich structure during the fibrillation reaction (Fig. S4A). The incubation of Sup35-LCB1 in 300 mM Na-PB, and of Sup35-LCB3 at 150 and 300 mM Na-PB, results in a decrease in the overall CD signal, indicating that the fibrils tend to precipitate out of the solution. However, only in the case of Sup35-LCB3 is this change in intensity accompanied by a significant decrease of the 209 nm/222 nm intensity ratio, with a reduction of 13 % and 20 % in 150 and 300 mM Na-PB, respectively (Fig. S4A). These changes likely arise from the gain of certain β-sheet structure upon incubation.

Few examples of amyloids displaying cross-α structure have been reported [67,68] These instances involved the self-assembly of amphipathic α-helical peptides with antimicrobial activity. These peptides do not share sequential or structural similarity to the short Sup35 segment we use to build up the amyloid zipper of our fibrils. Indeed, we previously demonstrated that a peptide corresponding to this region is disordered in solution and transitions to an amyloid β-sheet structure [69].

Overall, our findings suggest that, under most conditions, an amyloid-like core and properly folded LCB moieties likely coexist within self-assembled Sup35-LCB1/LCB3.

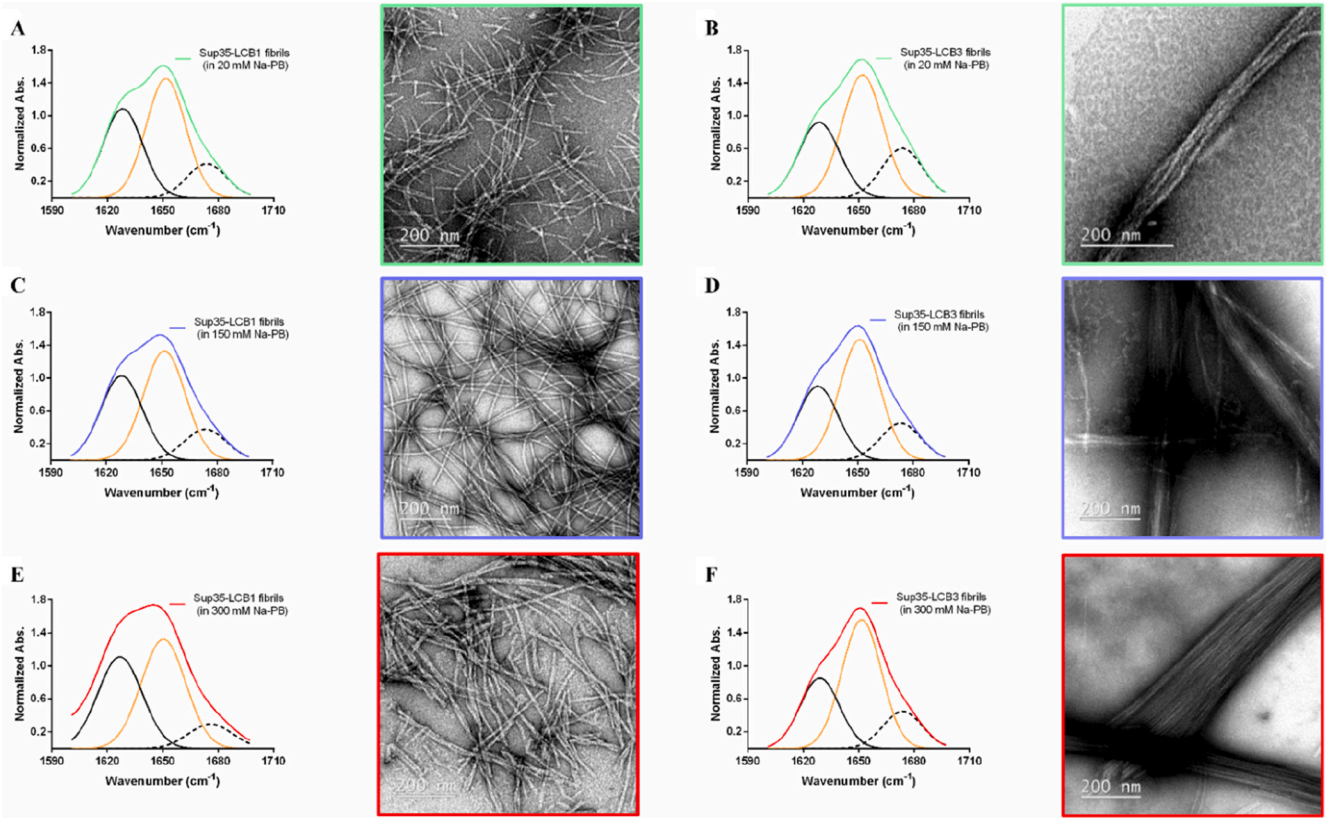

Fig. 3. Structural characterization of Sup35-LCB1 and Sup35-LCB3 self-assembled fibrils. (A-F) In the left panels, the second-derivative ATR-FTIR absorbance spectra in the amide I region are deconvoluted for: (A) Sup35-LCB1 and (B) Sup35-LCB3 fibrils formed in 20 mM Na-PB (depicted in green); (C) Sup35-LCB1 and (D) Sup35-LCB3 fibrils formed in 150 mM Na-PB (depicted in blue); (E) Sup35-LCB1 and (F) Sup35-LCB3 fibrils formed in 300 mM Na-PB (depicted in red). In each case, the fitted individual bands are indicated. The amyloid-like intermolecular β-sheet and α-helical components are shown as black and orange solid lines, respectively. In (A-F), right panels feature representative Negative-Stain Transmission Electron Microscopy (NS-TEM) images of the corresponding Sup35-LCB1/LCB3 amyloid assemblies, placed next to their respective FTIR plots. In all images, scale bar size is 200 nm. (For interpretation of the references to colour in this figure legend, the reader is referred to the web version of this article.)

3.3. Sup35-LCB1 and Sup35-LCB3 form different fibril polymorphs

It is now well-established that naturally occurring amyloid fibrils are generally polymorphic [37,64–66]. We have shown that the ionic strength of the solution not only influences the yield of Sup35-LCB1/LCB3 aggregates, but also shapes their biophysical properties. To further investigate the macromolecular organization of these insoluble structures, we used Negative-Stain Transmission Electron Microscopy (NS-TEM) (Fig. 3). Sup35-LCB1 assembled at the lowest salt concentration (*i.e.,* 20 mM Na-PB) displayed isolated, straight, unbranched, and uniform fibrils (Fig. 3**A**), with an average diameter of 10.8 ± 1.3 nm (**Fig. S5**). In contrast, at 150 mM and 300 mM Na-PB, the amyloid fibrils appeared much longer and exhibited a twisted morphology (Fig. 3**C and E**), with characteristic diameters of 12.3 ± 2.1 nm and 17.4 ± 4.2 nm, respectively (**Fig. S5**). Notably, the architecture of these amyloid scaffolds persisted even after one month of incubation at RT, suggesting that these structures are indeed stable polymorphic species (**Fig. S6**). While we cannot entirely rule out the presence of mixed fibril conformers in the samples, their uniform morphology under each specific salt condition suggests that this is not a predominant feature of Sup35-LCB1 fibril preparations.

To our surprise, TEM images of Sup35-LCB3 fibrils revealed a distinct morphology, characterized by laterally associated fibrils that coalesced into dense stacks of highly elongated structures tightly clustered together, resulting in significantly larger diameters, ranging from 70 to 190 nm (Fig. 3**B, D and F**). This behavior was particularly pronounced at higher salt concentrations. Intrigued by this discrepancy in spatial organization, we delved into the possibility that distinct stickiness properties of LCB1 and LCB3 might be at play, since regions prone to aggregation (APRs) on protein surfaces are often involved in intermolecular interactions [70–73].

We analyzed LCB1 and LCB3 domains using Aggrescan 3D 2.0 [74]. For the calculations, we utilized the X-ray crystal structures of LCB1 (PDB: 7JZU) and LCB3 (PDB: 7JZM) domains [45]. Our findings revealed that LCB3 has a lower net charge and higher surface aggregation propensity compared to LCB1, being thus more sticky (**Fig. S7**), a property that likely contributes to the tendency of filaments adorned with LCB3 to form lateral associations.

Fibril stability is often approached by evaluating the resistance to disassembly in the presence of SDS [75]. To investigate their stability, Sup35-LCB1 and Sup35-LCB3 fibrils formed under different Na-PB conditions were collected and incubated in the absence of SDS or in the presence of 0.1 % and 1 % SDS. The samples were then centrifuged, and the levels of fibril-dissociated soluble protein in the supernatant were analyzed by SDS-PAGE (**Fig. S8**).

The results revealed that Sup35-LCB3 fibrils are sensitive to both 0.1 % and 1.0 % SDS concentrations across all salt conditions. In contrast, the Sup35-LCB1 fibrils show significant resistance to SDS when formed in 300 and 150 mM Na-PB, but not at 20 mM Na-PB. These findings suggest that the interplay between sequence and solution conditions modulates fibril conformation and stability.

In light of these results, we decided to focus our subsequent experiments exclusively on the individual fibrils formed by Sup35-LCB1 since Sup35-LCB3 were generally less stable, and their lateral association might hinder SARS-CoV-2 spike protein access to the LCB3 binding site.

3.4. Molecular architecture of Sup35-LCB1 amyloid fibrils

Amyloid fibril-based materials are well-defined supramolecular assemblies with mesoscopic dimensions, often displaying elongated helicoidal dispositions [42,76]. We generated a molecular model of the Sup35-LCB1 nanofibril to inspect its general architecture and confirm the feasibility of forming a helical amyloid core with protruding LCB1 domains without steric hindrance (Fig. 4). For the parallel and in-register cross-β amyloid core, we used two structural arrangements: stacks of linear β-strands and of β-arches, both displaying a left-handed twist with an axial twist angle of 2° per 4.8 Å step [42]. The globular domains were evenly distributed, maintaining a distance of 25 Å from the central axis of rotation. These initial rigid models provided adequate separation between LCB1 domains, preventing their main chains from overlapping or intertwining. The two generated structural models comprised 90 monomers, contributing to a total helix turn of 180°. Each monomer advanced 4.9 Å, with a total displacement of 29.5 Å for a hexamer. Subsequently, we employed MODELLER [52] to incorporate the linker sequence that connected each core fibril monomer to the correspondent LCB1 domain. These models underwent energy minimization using the steepest descent algorithm of GROMACS [53] with the AMBER99SB-ILDN [54] force field, to minimize repulsive forces arising from close contacts between side chains.

Our molecular modeling analysis validated that parallel and in-register cross-β amyloid fibers allow for the accommodation of LCB1 globular domains (Fig. 4**).** We evaluated the resulting structure using the PROCHECK package [55], confirming the absence of steric clashes among the domains of the built models. These models had a diameter of 8.2 nm for the fibrils forming β-arches and 11.8 nm for the linear β-strands, compatible with the sizes we identified experimentally. However, the predominance of the α-helix signal relative to the β-sheet one in the CD spectra is in favor of the β-arches fibril mode, where the globular domain nearly fully envelops the inner amyloid zipper, shielding it from the solvent and consequently from the incoming polarized light in CD experiments.

3.5. Biocompatibility of Sup35-LCB1 amyloid nanofibrils

Sup35-LCB1 nanofibrils hold potential for material applications. However, the surfaces of amyloids can be potentially cytotoxic [78–80]. To rule out this possibility, we evaluated the cytotoxic effects of Sup35-LCB1 nanofibrils on human cells using the Prestoblue® cell viability reagent. HeLa cells were exposed to increasing concentrations of Sup35-LCB1 nanofibrils, prepared at 20, 150 or 300 mM Na-PB, and cell viability was assessed after 72 h of incubation (Fig. 5).

Notably, treatment with these synthetic amyloid fibrils did not induce any significant reduction in cell viability, even at the highest concentration of 100 μg/mL. This result underscores the non-cytotoxic nature of the various Sup35-LCB1 assemblies, indicating their suitability for developing biocompatible nanomaterials.

3.6. Sup35-LCB1 nanofibrils disrupt Spike RBD-ACE2 interaction

The interaction between the RBD of SARS-CoV-2 Spike protein and the ACE2 receptor was assessed using a Lumit immunoassay. This assay relies on the detection of the interaction between Rabbit Fc-tagged SARS-CoV-2 RBD (rFc-RBD) and Mouse Fc-tagged human ACE2 (mFc-ACE2). It employs secondary antibodies labelled with the NanoLuc luciferase LgBit and SmBit subunits. When these antibodies bind to their respective epitopes, the LgBit and SmBit fragments come into close proximity, enabling the reconstitution of an active luciferase enzyme. This enzyme subsequently emits bioluminescence, the intensity of which is directly proportional to the strength of the RBD-ACE2 interaction. Consequently, if the RBD-ACE2 interaction is hindered or blocked, the LgBit and SmBit fragments will not come together, resulting in a decreased bioluminescent signal (Fig. 6**A**). This method not only provides a quantitative measure of the RBD-ACE2 interaction but also offers a sensitive approach to screen potential inhibitors of this critical viral-host interaction, which is essential for SARS-CoV-2 infection.

We investigated the ability of Sup35-LCB1 nanofibrils to interfere with the RBD-ACE2 interaction. First, we measured the inhibitory activity of freshly prepared nanofibrils using the Lumit assay (Fig. 6**B**). These amyloid fibrils demonstrated a remarkable ability to thwart the RBD-ACE2 interaction. The inhibitory potency varied depending on the

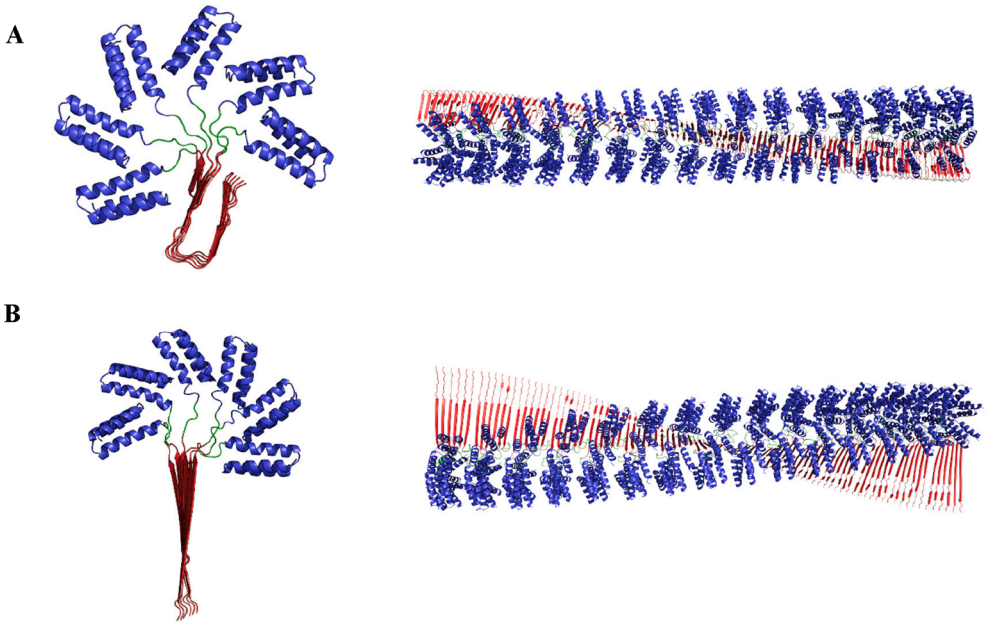

Fig. 4. Structural models of amyloid fibrils formed by the self-assembly of Sup35-LCB1 monomers. (A) Fibril formation through stacked β-arches and (B) linear β-strands. The Sup35 SAC domain, the linker, and the LCB1 domains are colored in red, green, and blue, respectively. In (A, B), left panels show the axial representation of a single fiber hexamer. The right panels display the lateral representation of the 90-monomers fibril. All representations were done using the PyMol software [77]. (For interpretation of the references to colour in this figure legend, the reader is referred to the web version of this article.)

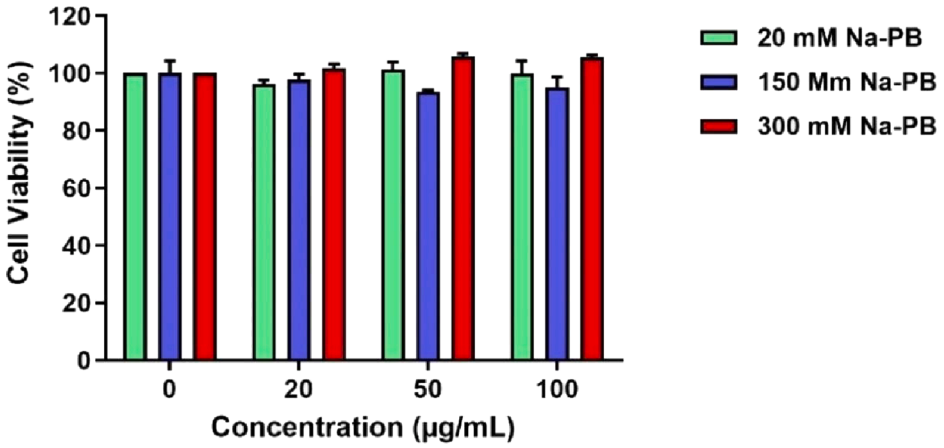

Fig. 5. Cytotoxicity of Sup35-LCB1 self-assembled nanofibrils. Cell viability of HeLa cells after 72 h of incubation in the presence of different concentrations of Sup35-LCB1 nanofibrils. Results are shown as mean ± SD (n = 3).

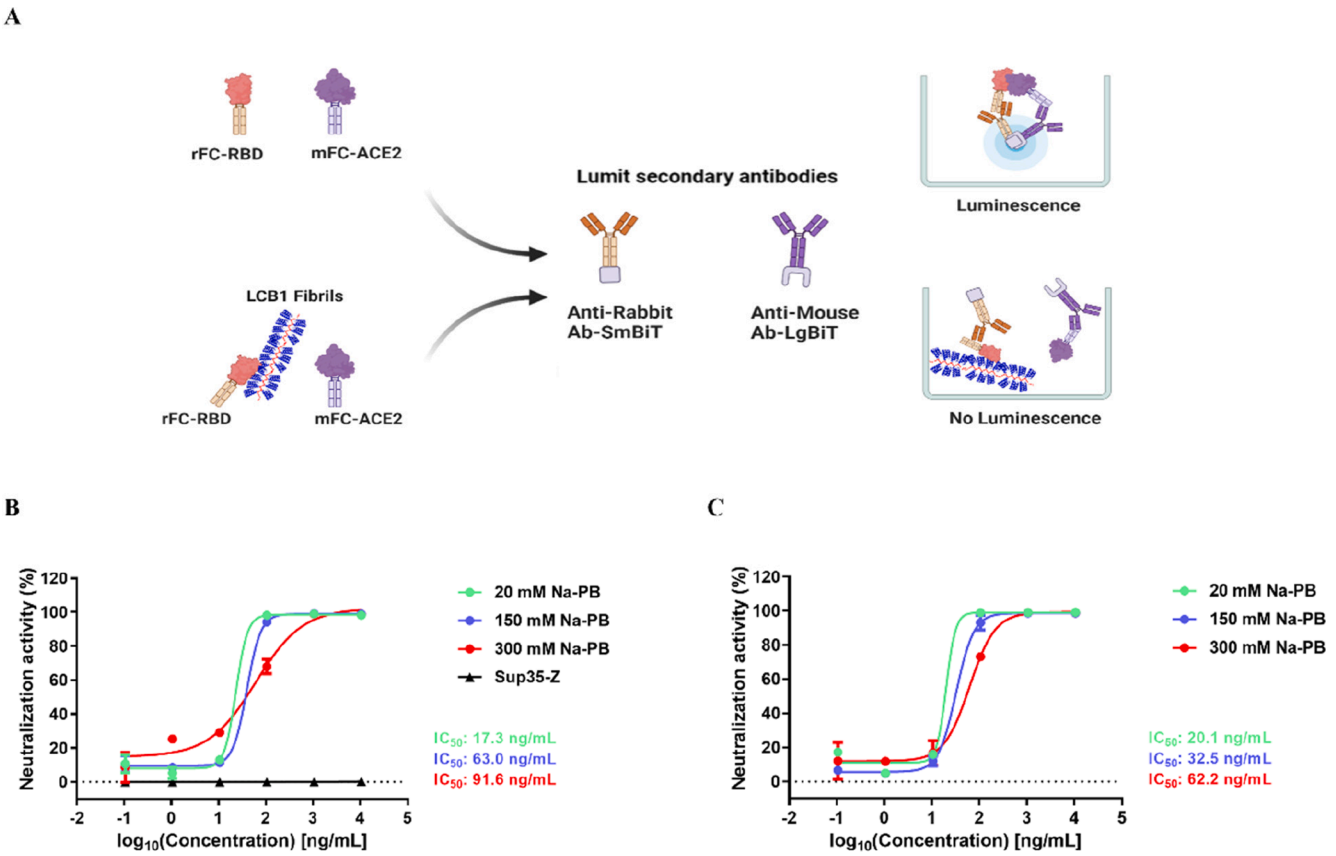

Fig. 6. Inhibition of the RBD-ACE2 interaction by Sup35-LCB1 self-assembled nanofibrils. (A) Schematic representation of the Lumit™ SARS-CoV-2 Spike RBD-ACE2 Immunoassay. Created using BioRender (BioRender.com). (B, C) The RBD-ACE2 interaction is inhibited by self-assembled Sup35-LCB1 nanofibrils. The inhibitory effect against the interaction between the RBD and ACE2 was evaluated using (B) freshly prepared nanofibrils, which includes amyloid fibrils of Sup35 SAC fused to a Z-domain (Sup35-Z) as a control condition, Additionally, (C) represents the nanofibrils after 1-month incubation at room temperature (RT). Note that the assayed Sup35-LCB1 nanofibrils were prepared under different Na-PB concentrations (*i.e.*, 20, 150, and 300 mM Na-PB). Data is presented as mean ± SD (n = 2). IC_{50} values were calculated by fitting the data to a non-linear regression (least squares) equation using GraphPad software [49].

Na-PB concentration used during fibril formation. Specifically, the IC_{50} values were determined to be 17.3 ng/mL for fibrils formed in 20 mM Na-PB, 63.0 ng/mL for those in 150 mM Na-PB, and 91.6 ng/mL for fibrils in 300 mM Na-PB (Fig. 6**B**). To assess the specificity of binding, we included fibrils formed by Sup35-SAC fused to the Z-domain (Sup35-Z) as a negative control. The Z-domain is an engineered protein analog of the B domain of *Staphylococcus aureus* protein A, which was selected for its similar size (approximately 6.5 kDa) and α-helical fold to the LCB1 domain [44] (**Fig. S9**). This comparative analysis confirmed the specific inhibitory effect of Sup35-LCB1 nanofibrils on the RBD-ACE2 interaction.

In a second Lumit experiment, we evaluated the same amyloid fibrils after one month of incubation at room RT (Fig. 6**C**). The results confirmed that the nanostructures' SARS-CoV-2 binding activity was

preserved, proving that Sup35-LCB1 nanofibrils are durable and reliable functional materials.

3.7. SARS-CoV-2 trapping and neutralization using Sup35-LCB1 nanofibrils

To evaluate the efficacy of Sup35-LCB1 nanofibrils in capturing and neutralizing SARS-CoV-2, we investigated their ability to impede viral entry into mammalian cells. To circumvent the risks associated with handling live viruses, we employed a SARS-CoV-2 HiBiT- pseudotype VLP assay, based on Promega Biotech's NanoBiT® technology (Fig. 7**A**). This bioassay utilizes a bioluminescent reporter cell-based approach and is routinely used to evaluate the neutralization capacity of ligands and antibodies that specifically target SARS-CoV-2 entry into the host cells [23].

In this assay, pseudotyped HiBiT-tagged virus-like particles (VLPs) bearing the trimeric SARS-CoV-2 Spike protein were pre-incubated with increasing concentrations of Sup35-LCB1 nanofibrils (ranging from 0.1 to 10,000 ng/mL) formed at 20, 150, and 300 mM Na-PB concentrations. After incubation with the nanofibrils, they were added to the hACE2-HEK293T (LgBiT) target cells, allowing for the determination of the neutralizing activity of these nanomaterials (Fig. 7**B**). The calculated IC_{50} values for the neutralizing activity of Sup35-LCB1 nanofibrils were determined to be 5.6 ng/mL, 22.4 ng/mL, and 34.1 ng/mL for the samples produced at 20 mM, 150 mM, and 300 mM Na-PB concentrations, respectively. The ranking of neutralization activities is consistent with this of the binding results obtained in the Lumit assay, supporting the specific activity of these fibrillar structures against the RBD-ACE2 interaction. The 3-fold higher potencies displayed in this assay likely stem from an avidity effect, where three LCB1 domains can simultaneously bind to the trimeric Spike protein.

The results indicate a dose-dependent neutralization effect and demonstrate a high potency of Sup35-LCB1 nanofibrils in preventing the fusion of pseudotyped SARS-CoV-2 VLPs with the membrane of human ACE2-expressing cells. Importantly, they display lower neutralization IC_{50} values than those reported for therapeutic antibodies like bamlanivimab, imdevimab, and etesevimab tested in the same assay (Table 1).

Taken together, our data unequivocally demonstrate that Sup35-LCB1 nanofibrils constitute a functional nanostructure capable of capturing and neutralizing SARS-CoV-2 viruses through selective interactions with RBD of the spike protein. This immediately suggests their potential applicability in creating novel functional surface coatings with selective antiviral properties.

3.8. Surface coating with functional Sup35-LCB1 nanofibrils

Recent reports demonstrated that surface contact can spread SARS-CoV-2, thus contributing to its rapid transmission [82], with wet surfaces being associated with longer virus survival times [83]. Consequently, eradicating surface transmission, particularly on wet surfaces, is essential in curbing the spread of COVID-19. This entails developing novel materials with intrinsic antiviral properties. In this regard, the ability of fibrils to form densely packed networks and solid thin films, facilitates their selective application and deposition onto specific areas of a given surface substrate. As proof-of-concept, we applied Sup35-LCB1 nanofibrils onto a polyvinylidene difluoride (PVDF) membrane (Fig. 8**A**). Our objective was crafting our university logo by immobilizing the fibrils onto the PVDF matrix. To gauge the functionality of this patterned surface, we evaluated its capacity to bind a fluorescent YFP-conjugated version of the spike protein RBD domain (YFP-RBD) [84]. This provides a means for rapidly visualizing the nanofibril/RBD interaction at the PVDF surface using a standard Fluorescence Imaging System.

Table 1
SARS-CoV-2 HiBiT- pseudotype VLP assay response to neutralizing antibodies and Sup35-LCB1 nanofibrils.

SARS-CoV-2 Spike Neutralizing mAb / material	IC_{50} (ng/mL)
Bamlanivimab	34.0*
Imdevimab	72.0*
Etesevimab	230.0*
LCB1 Fibrils (20 mM Na-PB)	5.6
LCB1 Fibrils (150 mM Na-PB)	22.4
LCB1 Fibrils (300 mM Na-PB)	34.1

* Experimental data provided by Promega Biotech Ibérica, S.L.

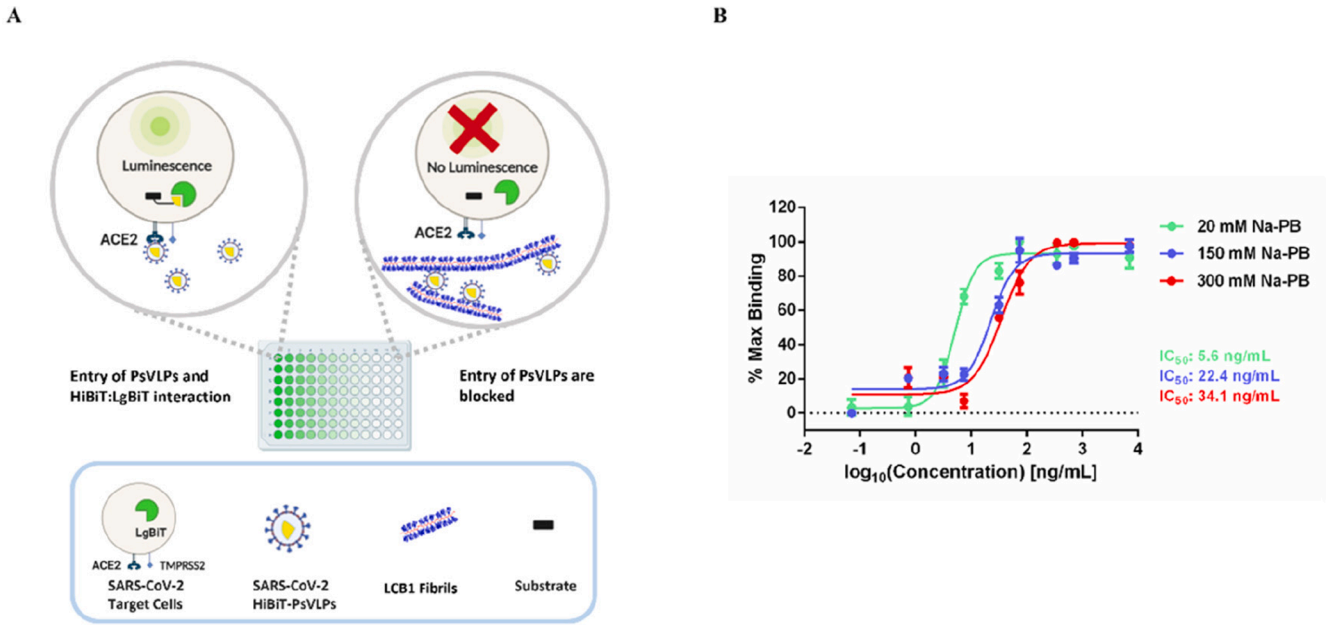

Fig. 7. SARS-CoV-2 trapping and neutralization effect of Sup35-LCB1 self-assembled nanofibrils. (A) Schematic representation of the SARS-CoV-2 HiBiT- pseudotype VLPs assay that uses Promega Biotech's NanoBiT® technology [23,81]. Created using BioRender (BioRender.com). (B) Detection of cell entry of pseudotyped VLPs into the SARS-CoV-2 HEK 293 T target cells containing the LgBiT protein reporter. Data represents the percentage of neutralization (%), and values are presented as mean ± SD (n = 2). IC_{50} values were calculated by fitting the experimental data to a non-linear regression (least squares) equation using GraphPad software [49].

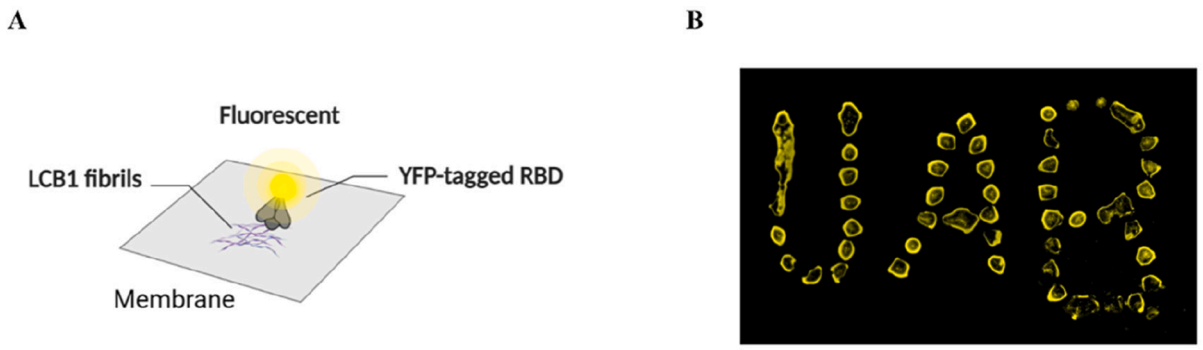

Fig. 8. Surface coating of PVDF membranes using Sup35-LCB1 nanofibrils. (A) Schematic representation of the PVDF surface decoration with Sup35-LCB1 amyloid nanofibrils and their subsequent binding to the fluorescently labeled YFP-RBD protein in the aqueous phase. (B) YFP fluorescence image of the printed PVDF surface, demonstrating the specific binding of the YFP-RBD to the nanofibril-coated areas.

As depicted in Fig. 8**B**, the resulting fluorescence image clearly conveys the intended logo, showcasing the successful printing of fibrils onto the PVDF matrix and the efficient binding of the YFP-RBD to the nanofibril-coated surface. This application of Sup35-LCB1 nanofibrils illustrates the potential of our modular strategy in creating functionalized surfaces which can be customized to meet specific requirements, including antiviral applications.

4. Conclusion

The COVID-19 pandemic has posed unprecedented challenges to global health, prompting the accelerated development of novel therapeutics, exemplified by mRNA vaccines, which have substantially mitigated the risk of severe illness, hospitalization, and death. However, vaccination does not guarantee complete protection against infection. Vaccinated individuals can still contract SARS-CoV-2 and transmit the virus to others primarily through aerosols, droplets, or contaminated surfaces [10–12]. As a result, the development of materials and surface coatings with SARS-CoV-2 antiviral properties has garnered increasing attention [27,85]. However, most of the reported approaches still rely on toxic substances that lack virus specificity [28,30,31].

Drawing inspiration from the modular nature of yeast prions, we have genetically engineered a novel fibrillar biomaterial that leverages the Sup35-SAC domain as a scaffold and the high-affinity SARS-CoV-2 of LCB1/LCB3 binders as functional domains. This fusion technology enables efficient protein production at high yields, making it cost-effective and scalable. The self-assembly of these polypeptides into amyloid-like nanofibrils occurs spontaneously and the structural and functional properties of the final assemblies can be controlled by modulating the ionic strength of the solution.

In particular, Sup35-LCB1 assembles into discreet, regular, non-toxic amyloid-like structures, forming interwoven fibrillar networks. These biocompatible nanofibrils exhibit a high aspect ratio, displaying the LCB1 binding motif in its folded and functional form at a high density on their surfaces, which confers remarkable avidity. This proves instrumental in effectively inhibiting the interaction between the SARS-CoV-2 Spike RBD and the ACE2 receptor, a critical step in viral entry into host cells. Accordingly, our engineered nanofibrils demonstrated potent SARS-CoV-2 neutralizing activity in a cellular model of infection, with neutralization IC_{50} values as low as 5.6 ng/mL, surpassing the performance of existing therapeutic antibodies in the same assay.

Furthermore, we successfully imprinted these nanofibrils onto a PVDF membrane, creating functionalized surfaces capable of capturing the SARS-CoV-2 Spike in wet environments. This exemplifies the potential of the nanofibrils to serve as a safe functional surface coating materials to contain viral spread and increase safety of personal protective equipment. Additionally, the polymer fibrils could potentially replace antibodies in existing tests at a lower cost. They may also find utility in concentrating and isolating viral particles for individual testing or environmental sampling. Importantly, due to the modularity of our strategy, replacing the LCB1 moiety with alternative virus binders would allow tailoring the viral specificity of the nanostructure.

In conclusion, the Sup35-LCB1 amyloid-based nanofibrils represent a promising functional material in the fight against COVID-19 and other viral pandemics, offering potential prophylactic and diagnostic applications.

CRediT authorship contribution statement

Molood BehBahanipour: Writing – review & editing, Writing – original draft, Visualization, Methodology, Investigation, Funding acquisition, Formal analysis. **Susanna Navarro:** Writing – original draft, Validation, Supervision, Methodology. **Oriol Bárcenas:** Writing – review & editing, Visualization, Software, Methodology, Funding acquisition, Formal analysis. **Javier Garcia-Pardo:** Writing – review & editing, Validation, Funding acquisition. **Salvador Ventura:** Writing – review & editing, Validation, Supervision, Resources, Project administration, Funding acquisition, Conceptualization.

Declaration of competing interest

The authors declare that they have no known competing financial interests or personal relationships that could have appeared to influence the work reported in this paper.

Data availability

Data will be made available on request.

Acknowledgements

This work was funded by the Spanish Ministry of Science and Innovation (MICINN, Spain) PID2022-137963OB-I00 to S.V.; By ICREA, (ICREA-Academia 2020, Spain) and by EU (PhasAge H2020-WIDESPREAD-2020-5, EU) to S.V. J.G.-P. was supported by the Spanish Ministry of Science and Innovation with a Juan de la Cierva Incorporacion (IJC2019-041039-I, Spain) M.B. was supported by the Spanish Ministry of Science and Innovation (PRE2020-092634, Spain). This article is partially based upon work from COST Action ML4NGP, CA21160, supported by COST (European Cooperation in Science and Technology, European Union). O. B. was supported by the Spanish Ministry of Science and Innovation via a doctoral grant (FPU22/03656, Spain). We thank Dr. Roger M Benoit for gently providing us with the RBD-YFP protein.

Appendix A. Supplementary data

Supplementary data to this article can be found online at https://doi.org/10.1016/j.jcis.2024.06.175.

References

[1] Z.-R. Yang, Y.-W. Jiang, F.-X. Li, D. Liu, T.-F. Lin, Z.-Y. Zhao, et al., Efficacy of SARS-CoV-2 vaccines and the dose–response relationship with three major antibodies: a systematic review and meta-analysis of randomised controlled trials, The Lancet Microbe. (2023), https://doi.org/10.1016/S2666-5247(22)00390-1.

[2] L. Riva, S. Yuan, X. Yin, L. Martin-Sancho, N. Matsunaga, L. Pache, et al., Discovery of SARS-CoV-2 antiviral drugs through large-scale compound repurposing, Nature 586 (2020) 113–119, https://doi.org/10.1038/s41586-020-2577-1.

[3] D.E. Gordon, G.M. Jang, M. Bouhaddou, J. Xu, K. Obernier, K.M. White, et al., A SARS-CoV-2 protein interaction map reveals targets for drug repurposing, Nature 583 (2020) 459–468, https://doi.org/10.1038/s41586-020-2286-9.

[4] M.J. Joyner, R.E. Carter, J.W. Senefeld, S.A. Klassen, J.R. Mills, P.W. Johnson, et al., Convalescent plasma antibody levels and the risk of death from covid-19, N Engl. J. Med. 384 (2021) 1015–1027, https://doi.org/10.1056/NEJMoa2031893.

[5] R. Libster, G. Perez Marc, D. Wappner, S. Coviello, A. Bianchi, V. Braem, et al., Early high-titer plasma therapy to prevent severe covid-19 in older adults, N Engl. J. Med. 384 (2021) 610–618, https://doi.org/10.1056/NEJMoa2033700.

[6] N.A.J. McMillan, K.V. Morris, A. Idris, RNAi to treat SARS-CoV-2-variant proofing the next generation of therapies, EMBO Mol. Med. 14 (2022) e15811, https://doi.org/10.15252/emmm.202215811.

[7] B. Berber, C. Aydin, F. Kocabas, G. Guney-Esken, K. Yilancioglu, M. Karadag-Alpaslan, et al., Gene editing and RNAi approaches for COVID-19 diagnostics and therapeutics, Gene Ther. 28 (2021) 290–305, https://doi.org/10.1038/s41434-020-00209-7.

[8] Z. Tang, N. Kong, X. Zhang, Y. Liu, P. Hu, S. Mou, et al., A materials-science perspective on tackling COVID-19, Nat. Rev. Mater. 5 (2020) 847–860, https://doi.org/10.1038/s41578-020-00247-y.

[9] B. Wichmann, R. Moreira Wichmann, Big data evidence of the impact of COVID-19 hospitalizations on mortality rates of non-COVID-19 critically ill patients, Sci. Rep. 13 (2023) 13613, https://doi.org/10.1038/s41598-023-40727-z.

[10] Y. Bai, L. Yao, T. Wei, F. Tian, D.Y. Jin, L. Chen, M. Wang, Presumed asymptomatic carrier transmission of COVID-19, JAMA 323 (2020) 1406–1407, https://doi.org/10.1001/jama.2020.2565.

[11] N. van Doremalen, T. Bushmaker, D.H. Morris, M.G. Holbrook, A. Gamble, B. N. Williamson, et al., Aerosol and surface stability of SARS-CoV-2 as compared with SARS-CoV-1, N Engl. J. Med. 382 (2020) 1564–1567, https://doi.org/10.1056/NEJMc2004973.

[12] S.Y. Ren, W.B. Wang, Y.G. Hao, H.R. Zhang, Z.C. Wang, Y.L. Chen, R.D. Gao, Stability and infectivity of coronaviruses in inanimate environments, World J. Clin. Cases. 8 (2020) 1391–1399, https://doi.org/10.12998/wjcc.v8.i8.1391.

[13] M. Letko, A. Marzi, V. Munster, Functional assessment of cell entry and receptor usage for SARS-CoV-2 and other lineage B betacoronaviruses, Nat. Microbiol. 5 (2020) 562–569, https://doi.org/10.1038/s41564-020-0688-y.

[14] M. Hoffmann, H. Kleine-Weber, S. Schroeder, N. Kruger, T. Herrler, S. Erichsen, et al., SARS-CoV-2 cell entry depends on ACE2 and TMPRSS2 and is blocked by a clinically proven protease inhibitor, Cell 181 (2020) 271–280 e278, https://doi.org/10.1016/j.cell.2020.02.052.

[15] F. Liu, X. Long, B. Zhang, W. Zhang, X. Chen, Z. Zhang, ACE2 expression in pancreas may cause pancreatic damage after SARS-CoV-2 infection, Clin. Gastroenterol. Hepatol. 18 (2020) 2128–2130 e2122, https://doi.org/10.1016/j.cgh.2020.04.040.

[16] K. Nepali, R. Sharma, S. Sharma, A. Thakur, J.P. Liou, Beyond the vaccines: a glance at the small molecule and peptide-based anti-COVID19 arsenal, J. Biomed. Sci. 29 (2022) 65, https://doi.org/10.1186/s12929-022-00847-6.

[17] S.K. Nayak, Inhibition of S-protein RBD and hACE2 interaction for control of SARSCoV- 2 infection (COVID-19), Mini Rev. Med. Chem. 21 (2021) 689–703, https://doi.org/10.2174/1389557520666201117111259.

[18] Y. Han, P. Kral, Computational design of ACE2-based peptide inhibitors of SARS-CoV-2, ACS Nano. 14 (2020) 5143–5147, https://doi.org/10.1021/acsnano.0c02857.

[19] Y. Wu, F. Wang, C. Shen, W. Peng, D. Li, C. Zhao, et al., A noncompeting pair of human neutralizing antibodies block COVID-19 virus binding to its receptor ACE2, Science 368 (2020) 1274–1278, https://doi.org/10.1126/science.abc2241.

[20] X. Chi, R. Yan, J. Zhang, G. Zhang, Y. Zhang, M. Hao, et al., A neutralizing human antibody binds to the N-terminal domain of the spike protein of SARS-CoV-2, Science 369 (2020) 650–655, https://doi.org/10.1126/science.abc6952.

[21] L. Liu, P. Wang, M.S. Nair, J. Yu, M. Rapp, Q. Wang, et al., Potent neutralizing antibodies against multiple epitopes on SARS-CoV-2 spike, Nature 584 (2020) 450–456, https://doi.org/10.1038/s41586-020-2571-7.

[22] R. Shi, C. Shan, X. Duan, Z. Chen, P. Liu, J. Song, et al., A human neutralizing antibody targets the receptor-binding site of SARS-CoV-2, Nature 584 (2020) 120–124, https://doi.org/10.1038/s41586-020-2381-y.

[23] M. Behbahanipour, R. Benoit, S. Navarro, S. Ventura, OligoBinders: bioengineered soluble amyloid-like nanoparticles to bind and neutralize SARS-CoV-2, ACS Appl. Mater Interfaces. 15 (2023) 11444–11457, https://doi.org/10.1021/acsami.2c18305.

[24] A. Aleem, A.B. Akbar Samad, S. Vaqar, Emerging Variants of SARS-CoV-2 and Novel Therapeutics Against Coronavirus (COVID-19), StatPearls, Treasure Island (FL), 2023, https://www.ncbi.nlm.nih.gov/pubmed/34033342.

[25] W. Zhou, W. Wang, Fast-spreading SARS-CoV-2 variants: challenges to and new design strategies of COVID-19 vaccines, Signal Transduct. Target Ther. 6 (2021) 226, https://doi.org/10.1038/s41392-021-00644-x.

[26] S. Behzadinasab, A. Chin, M. Hosseini, L. Poon, W.A. Ducker, A surface coating that rapidly inactivates SARS-CoV-2, ACS Appl. Mater Interfaces. 12 (2020) 34723–34727, https://doi.org/10.1021/acsami.0c11425.

[27] P.D. Rakowska, M. Tiddia, N. Faruqui, C. Bankier, Y.W. Pei, A.J. Pollard, et al., Antiviral surfaces and coatings and their mechanisms of action, Communications Mater. 2 (2021), https://doi.org/10.1038/s43246-021-00153-y.

[28] A.L. Kubo, G. Vasiliev, H. Vija, J. Krishtal, V. Tougu, M. Visnapuu, et al., Surface carboxylation or PEGylation decreases CuO nanoparticles' cytotoxicity to human cells in vitro without compromising their antibacterial properties, Arch. Toxicol. 94 (2020) 1561–1573, https://doi.org/10.1007/s00204-020-02720-7.

[29] R.H. Bianculli, J.D. Mase, M.D. Schulz, Antiviral polymers: past approaches and future possibilities, Macromolecules 53 (2020) 9158–9186, https://doi.org/10.1021/acs.macromol.0c01273.

[30] J.A. Lemire, J.J. Harrison, R.J. Turner, Antimicrobial activity of metals: mechanisms, molecular targets and applications, Nat. Rev. Microbiol. 11 (2013) 371–384, https://doi.org/10.1038/nrmicro3028.

[31] E. Oliveira, H.M. Santos, J. Garcia-Pardo, M. Diniz, J. Lorenzo, B. Rodríguez-González, et al., Synthesis of functionalized fluorescent silver nanoparticles and their toxicological effect in aquatic environments (Goldfish) and HEPG2 cells, Front. Chem. 1 (2013), https://doi.org/10.3389/fchem.2013.00029.

[32] S. Navarro, M. Diaz-Caballero, F. Peccati, L. Roldan-Martin, M. Sodupe, S. Ventura, Amyloid fibrils formed by short prion-inspired peptides are metalloenzymes, ACS Nano. 17 (2023) 16968–16979, https://doi.org/10.1021/acsnano.3c04164.

[33] T.P. Knowles, R. Mezzenga, Amyloid fibrils as building blocks for natural and artificial functional materials, Adv. Mater. 28 (2016) 6546–6561, https://doi.org/10.1002/adma.201505961.

[34] M. Diaz-Caballero, S. Navarro, I. Fuentes, F. Teixidor, S. Ventura, Minimalist prion-inspired polar self-assembling peptides, ACS Nano. 12 (2018) 5394–5407, https://doi.org/10.1021/acsnano.8b00417.

[35] S. Das, R.S. Jacob, K. Patel, N. Singh, S.K. Maji, Amyloid fibrils: versatile biomaterials for cell adhesion and tissue engineering applications, Biomacromolecules 19 (2018) 1826–1839, https://doi.org/10.1021/acs.biomac.8b00279.

[36] M. Díaz-Caballero, S. Navarro, M. Nuez-Martínez, F. Peccati, L. Rodríguez-Santiago, M. Sodupe, et al., pH-responsive self-assembly of amyloid fibrils for dual hydrolase-oxidase reactions, ACS Catal. 11 (2021) 595–607, https://doi.org/10.1021/acscatal.0c03093.

[37] J. Garcia-Pardo, S. Ventura, Cryo-EM structures of functional and pathological amyloid ribonucleoprotein assemblies, Trends. Biochem. Sci. (2023), https://doi.org/10.1016/j.tibs.2023.10.005.

[38] J. Garcia-Pardo, A. Bartolome-Nafria, A. Chaves-Sanjuan, M. Gil-Garcia, C. Visentin, M. Bolognesi, et al., Cryo-EM structure of hnRNPDL-2 fibrils, a functional amyloid associated with limb-girdle muscular dystrophy D3, Nat. Commun. 14 (2023) 239, https://doi.org/10.1038/s41467-023-35854-0.

[39] T.R. Jahn, O.S. Makin, K.L. Morris, K.E. Marshall, P. Tian, P. Sikorski, L.C. Serpell, The common architecture of cross-beta amyloid, J. Mol. Biol. 395 (2010) 717–727, https://doi.org/10.1016/j.jmb.2009.09.039.

[40] T.P. Knowles, A.W. Fitzpatrick, S. Meehan, H.R. Mott, M. Vendruscolo, C. M. Dobson, M.E. Welland, Role of intermolecular forces in defining material properties of protein nanofibrils, Science 318 (2007) 1900–1903, https://doi.org/10.1126/science.1150057.

[41] A.K. Buell, Stability matters, too - the thermodynamics of amyloid fibril formation, Chem. Sci. 13 (2022) 10177–10192, https://doi.org/10.1039/d1sc06782f.

[42] W. Wang, S. Navarro, R.A. Azizyan, M. Bano-Polo, S.A. Esperante, A.V. Kajava, S. Ventura, Prion soft amyloid core driven self-assembly of globular proteins into bioactive nanofibrils, Nanoscale 11 (2019) 12680–12694, https://doi.org/10.1039/c9nr01755k.

[43] W. Wang, M. Gil-Garcia, S. Ventura, Dual antibody-conjugated amyloid nanorods to promote selective cell-cell interactions, ACS Appl. Mater Interfaces. 13 (2021) 14875–14884, https://doi.org/10.1021/acsami.0c21996.

[44] W. Wang, R.A. Azizyan, A. Garro, A.V. Kajava, S. Ventura, Multifunctional amyloid oligomeric nanoparticles for specific cell targeting and drug delivery, Biomacromolecules 21 (2020) 4302–4312, https://doi.org/10.1021/acs.biomac.0c01103.

[45] L. Cao, I. Goreshnik, B. Coventry, J.B. Case, L. Miller, L. Kozodoy, et al., De novo design of picomolar SARS-CoV-2 miniprotein inhibitors, Science 370 (2020) 426–431, https://doi.org/10.1126/science.abd9909.

[46] J.B. Case, R.E. Chen, L. Cao, B. Ying, E.S. Winkler, M. Johnson, et al., Ultrapotent miniproteins targeting the SARS-CoV-2 receptor-binding domain protect against infection and disease, Cell Host Microbe. 29 (2021) 1151–1161, https://doi.org/10.1016/j.chom.2021.06.008 (e1155).

[47] R. Chattaraj, C.Y. Kim, D. Lee, D.A. Hammer, Recombinant protein micelles to block transduction by SARS-CoV-2 pseudovirus, ACS Nano 16 (2022) 17466–17477, https://doi.org/10.1021/acsnano.2c09015.

[48] Y. Zhu, M. Li, N. Liu, T. Wu, X. Han, G. Zhao, Y. He, Development of highly effective LCB1-based lipopeptides targeting the spike receptor-binding motif of SARS-CoV-2, Antiviral Res. 211 (2023) 105541, https://doi.org/10.1016/j.antiviral.2023.105541.

[49] GraphPad Prism version 10.0.0 for Windows, GraphPad Software, Boston, Massachusetts USA, www.graphpad.com.

[50] M. Mirdita, K. Schütze, Y. Moriwaki, L. Heo, S. Ovchinnikov, M. Steinegger, ColabFold: making protein folding accessible to all, Nat. Methods 19 (2022) 679-+, https://doi.org/10.1038/s41592-022-01488-1.
[51] E.C. Meng, T.D. Goddard, E.F. Pettersen, G.S. Couch, Z.J. Pearson, J.H. Morris, T. E. Ferrin, U.C.S.F. ChimeraX, Tools for structure building and analysis, Protein Sci. 32 (2023), https://doi.org/10.1002/pro.4792.
[52] A. Sali, T.L. Blundell, Comparative protein modelling by satisfaction of spatial restraints, J. Mol. Biol. 234 (1993) 779–815, https://doi.org/10.1006/jmbi.1993.1626.
[53] S. Pronk, S. Páll, R. Schulz, P. Larsson, P. Bjelkmar, R. Apostolov, et al., GROMACS 4.5: a high-throughput and highly parallel open source molecular simulation toolkit, Bioinformatics 29 (2013) 845–854, https://doi.org/10.1093/bioinformatics/btt055.
[54] D.A. Case, H.M. Aktulga, K. Belfon, D.S. Cerutti, G.A. Cisneros, V.W.D. Cruzeiro, et al., The AMBERTOOLs, J. Chem. Inf. Model. (2023), https://doi.org/10.1021/acs.jcim.3c01153.
[55] R.A. Laskowski, M.W. Macarthur, D.S. Moss, J.M. Thornton, Procheck - a program to check the stereochemical quality of protein structures, J. Appl. Cryst. 26 (1993) 283–291, https://doi.org/10.1107/S0021889892009944.
[56] T. Maculins, J. Garcia-Pardo, A. Skenderovic, J. Gebel, M. Putyrski, A. Vorobyov, et al., Discovery of protein-protein interaction inhibitors by integrating protein engineering and chemical screening platforms, Cell Chem. Biol. 27 (2020) 1441–1451 e1447, https://doi.org/10.1016/j.chembiol.2020.07.010.
[57] F. Nador, K. Wnuk, J. García-Pardo, J. Lorenzo, R. Solorzano, D. Ruiz-Molina, F. Novio, Dual-fluorescent nanoscale coordination polymers via a mixed-ligand synthetic strategy and their use for multichannel imaging, ChemNanoMat. 4 (2018) 183–193, https://doi.org/10.1002/cnma.201700311.
[58] J. Garcia-Pardo, R. Grana-Montes, M. Fernandez-Mendez, A. Ruyra, N. Roher, F. X. Aviles, et al., Amyloid formation by human carboxypeptidase D transthyretin-like domain under physiological conditions, J. Biol. Chem. 289 (2014) 33783–33796, https://doi.org/10.1074/jbc.M114.594804.
[59] M. Diaz-Caballero, M.R. Fernandez, S. Navarro, S. Ventura, Prion-based nanomaterials and their emerging applications, Prion 12 (2018) 266–272, https://doi.org/10.1080/19336896.2018.1521235.
[60] M. Diaz-Caballero, S. Navarro, S. Ventura, Functionalized prion-inspired amyloids for biosensor applications, Biomacromolecules 22 (2021) 2822–2833, https://doi.org/10.1021/acs.biomac.1c00222.
[61] J. Li, F. Zhang, Amyloids as building blocks for macroscopic functional materials: designs, applications and challenges, Int. J. Mol. Sci. 22 (2021), https://doi.org/10.3390/ijms221910698.
[62] M.S. Rubel, S.A. Fedotov, A.V. Grizel, J.V. Sopova, O.A. Malikova, Y.O. Chernoff, A.A. Rubel, Functional mammalian amyloids and amyloid-like proteins, Life (Basel). 10 (2020), https://doi.org/10.3390/life10090156.
[63] D. Willbold, B. Strodel, G.F. Schroder, W. Hoyer, H. Heise, Amyloid-type protein aggregation and prion-like properties of amyloids, Chem. Rev. 121 (2021) 8285–8307, https://doi.org/10.1021/acs.chemrev.1c00196.
[64] C. Seuring, J. Verasdonck, P. Ringler, R. Cadalbert, H. Stahlberg, A. Bockmann, et al., Amyloid fibril polymorphism: almost identical on the atomic level, mesoscopically very different, J. Phys. Chem. B. 121 (2017) 1783–1792, https://doi.org/10.1021/acs.jpcb.6b10624.
[65] W. Close, M. Neumann, A. Schmidt, M. Hora, K. Annamalai, M. Schmidt, et al., Physical basis of amyloid fibril polymorphism, Nat. Commun. 9 (2018) 699, https://doi.org/10.1038/s41467-018-03164-5.
[66] S. Lovestam, D. Li, J.L. Wagstaff, A. Kotecha, D. Kimanius, S.H. McLaughlin, et al., Disease-specific tau filaments assemble via polymorphic intermediates, Nature (2023), https://doi.org/10.1038/s41586-023-06788-w.
[67] E. Tayeb-Fligelman, O. Tabachnikov, A. Moshe, O. Goldshmidt-Tran, M.R. Sawaya, N. Coquelle, et al., The cytotoxic Staphylococcus aureus PSMα3 reveals a cross-α amyloid-like fibril, Science 355 (2017) 831–833, https://doi.org/10.1126/science.aaf4901.
[68] N. Salinas, E. Tayeb-Fligelman, M.D. Sammito, D. Bloch, R. Jelinek, D. Noy, et al., The amphibian antimicrobial peptide uperin 3.5 is a cross-α/cross-β chameleon functional amyloid, Proc. Natl. Acad. Sci. 118 (2021) e2014442118, https://doi.org/10.1073/pnas.2014442118.
[69] R. Sant'Anna, M.R. Fernandez, C. Batlle, S. Navarro, N.S. de Groot, L. Serpell, S. Ventura, Characterization of amyloid cores in prion domains, Sci. Rep. 6 (2016) 34274, https://doi.org/10.1038/srep34274.
[70] A.E. Badaczewska-Dawid, J. Garcia-Pardo, A. Kuriata, J. Pujols, S. Ventura, S. Kmiecik, A3D database: structure-based predictions of protein aggregation for the human proteome, Bioinformatics 38 (2022) 3121–3123, https://doi.org/10.1093/bioinformatics/btac215.
[71] A.E. Badaczewska-Dawid, A. Kuriata, C. Pintado-Grima, J. Garcia-Pardo, M. Burdukiewicz, V. Iglesias, et al., A3D model organism database (A3D-MODB): a database for proteome aggregation predictions in model organisms, Nucleic Acids Res. (2023), https://doi.org/10.1093/nar/gkad942.
[72] J. Garcia-Pardo, A.E. Badaczewska-Dawid, C. Pintado-Grima, V. Iglesias, A. Kuriata, S. Kmiecik, S. Ventura, A3DyDB: exploring structural aggregation propensities in the yeast proteome, Microb. Cell Fact. 22 (2023) 186, https://doi.org/10.1186/s12934-023-02182-3.
[73] V. Castillo, S. Ventura, Amyloidogenic regions and interaction surfaces overlap in globular proteins related to conformational diseases, PLoS Comput. Biol. 5 (2009) e1000476, https://doi.org/10.1371/journal.pcbi.1000476.
[74] A. Kuriata, V. Iglesias, J. Pujols, M. Kurcinski, S. Kmiecik, S. Ventura, Aggrescan3D (A3D) 2.0: prediction and engineering of protein solubility, Nucleic Acids Res. 47 (2019) W300–W307, https://doi.org/10.1093/nar/gkz321.
[75] T.A. Belashova, A.A. Valina, E.I. Sysoev, M.E. Velizhanina, A.A. Zelinsky, A. P. Galkin, Search and identification of amyloid proteins, Methods and Protocols. 6 (2023) 16, https://doi.org/10.3390/mps6010016.
[76] B.H. Toyama, J.S. Weissman, Amyloid structure: conformational diversity and consequences, Annu. Rev. Biochem. 80 (2011) 557–585, https://doi.org/10.1146/annurev-biochem-090908-120656.
[77] L. Schrödinger, W. DeLano, The PyMOL Molecular Graphics System, Schrödinger, LLC, 2020.
[78] V. Novitskaya, O.V. Bocharova, I. Bronstein, I.V. Baskakov, Amyloid fibrils of mammalian prion protein are highly toxic to cultured cells and primary neurons, J. Biol. Chem. 281 (2006) 13828–13836, https://doi.org/10.1074/jbc.M511174200.
[79] M. Bucciantini, D. Nosi, M. Forzan, E. Russo, M. Calamai, L. Pieri, et al., Toxic effects of amyloid fibrils on cell membranes: the importance of ganglioside GM1, FASEB J. 26 (2012) 818–831, https://doi.org/10.1096/fj.11-189381.
[80] R. Cascella, A. Bigi, N. Cremades, C. Cecchi, Effects of oligomer toxicity, fibril toxicity and fibril spreading in synucleinopathies, Cell Mol. Life Sci. 79 (2022) 174, https://doi.org/10.1007/s00018-022-04166-9.
[81] A. Reyes-Alcaraz, E.Y. Lucero Garcia-Rojas, E.A. Merlinsky, J.Y. Seong, R.A. Bond, B.K. McConnell, A NanoBiT assay to monitor membrane proteins trafficking for drug discovery and drug development, Commun. Biol. 5 (2022) 212, https://doi.org/10.1038/s42003-022-03163-9.
[82] J. Xu, C. Xu, R. Chen, Y. Yin, Z. Wang, K. Li, et al., Stability of SARS-CoV-2 on inanimate surfaces: a review, Microbiol. Res. 272 (2023) 127388, https://doi.org/10.1016/j.micres.2023.127388.
[83] Y. Geng, Y. Wang, Stability and transmissibility of SARS-CoV-2 in the environment, J. Med. Virol. 95 (2023) e28103, https://doi.org/10.1002/jmv.28103.
[84] T. Bierig, G. Collu, A. Blanc, E. Poghosyan, R.M. Benoit, Design, expression, purification, and characterization of a YFP-tagged 2019-nCoV spike receptor-binding domain construct, Front. Bioeng. Biotechnol. 8 (2020) 618615, https://doi.org/10.3389/fbioe.2020.618615.
[85] M.C. Sportelli, M. Izzi, E.A. Kukushkina, S.I. Hossain, R.A. Picca, N. Ditaranto, N. Cioffi, Can nanotechnology and materials science help the fight against SARS-CoV-2? Nanomaterials (Basel). 10 (2020) https://doi.org/10.3390/nano10040802.

CHAPTER 2:

OligoBinders: Bioengineered Soluble Amyloid-like Nanoparticles to Bind and Neutralize SARS-CoV-2

Molood Behbahanipour, Roger Benoit, Susanna Navarro*, and Salvador Ventura*

ACS Applied Materials & Interfaces

2023

https://doi.org/10.1021/acsami.2c18305

ACS APPLIED MATERIALS & INTERFACES

www.acsami.org

Research Article

OligoBinders: Bioengineered Soluble Amyloid-like Nanoparticles to Bind and Neutralize SARS-CoV-2

Molood Behbahanipour, Roger Benoit, Susanna Navarro,* and Salvador Ventura*

Cite This: *ACS Appl. Mater. Interfaces* 2023, 15, 11444−11457

Read Online

ACCESS | Metrics & More | Article Recommendations | Supporting Information

ABSTRACT: The coronavirus disease 2019 (COVID-19) pandemic caused by severe acute respiratory syndrome coronavirus 2 (SARS-CoV-2) infection has become a primary health concern. Molecules that prevent viral entry into host cells by interfering with the interaction between SARS-CoV-2 spike (S) protein and the human angiotensin-converting enzyme 2 receptor (ACE2r) opened a promising avenue for virus neutralization. Here, we aimed to create a novel kind of nanoparticle that can neutralize SARS-CoV-2. To this purpose, we exploited a modular self-assembly strategy to engineer OligoBinders, soluble oligomeric nanoparticles decorated with two miniproteins previously described to bind to the S protein receptor binding domain (RBD) with high affinity. The multivalent nanostructures compete with the RBD−ACE2r interaction and neutralize SARS-CoV-2 virus-like particles (SC2-VLPs) with IC_{50} values in the pM range, preventing SC2-VLPs fusion with the membrane of ACE2r-expressing cells. Moreover, OligoBinders are biocompatible and significantly stable in plasma. Overall, we describe a novel protein-based nanotechnology that might find application in SARS-CoV-2 therapeutics and diagnostics.

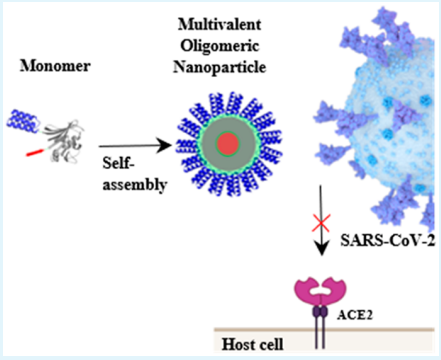

KEYWORDS: *SARS-CoV-2, spike protein, coronavirus, nanoparticles, soluble oligomers, protein assemblies, virus inactivation, antiviral agents*

INTRODUCTION

The coronavirus disease 2019 (COVID-19) has become a global pandemic and one of humanity's major health challenges. Although it seems that the most substantial impact of the pandemic has already happened, as of September 30, 2022, there were still over 600 million confirmed cases worldwide, including 6.5 million deaths documented (https://covid19.who.int/). Moreover, COVID-19 has been reported to be related to an increasing prevalence of anxiety and depression,[1] and suggested to be connected with neurodegenerative disorders.[2]

The rapid development of mRNA vaccines to protect against severe acute respiratory syndrome coronavirus 2 (SARS-CoV-2) has rendered the most effective therapy against COVID-19. However, although they elicit a robust antibody response to viral proteins, after the dose, the antibody levels decline six months postvaccination, indicating a waning of the immune response over time.[3]

The intense research effort during these past two years has allowed us to gain comprehensive knowledge of the disease biology and the structural determinants responsible for SARS-CoV-2 internalization in human cells. The virus entry in host cells is mediated by the interaction between the receptor binding domain (RBD) from viral spike (S) protein and the cell surface angiotensin-converting enzyme 2 receptor (ACE2r) expressed by nasal ciliated cells, pneumocytes, exocrine pancreas, intestinal tract, seminal vesicle, epididymis, proximal renal tubules, heart muscle, and thyroid gland.[4−7] As the first step in the viral replication cycle, developing neutralizing agents that interfere with the S protein−ACE2r interaction has gained significant interest. These reagents include antibodies, peptides, small molecules, and DNA aptamers.[8,9] However, except for antibodies, these molecules tend to exhibit moderate binding affinity.

High-affinity monoclonal antibodies (mAbs) developed utilizing B cells from COVID-19 patients have been at the forefront of neutralizing therapies.[10−13] However, monomeric antibodies suffer from rapid clearance and short lung retention time,[14,15] which may restrict the efficacy of mAb-based treatments, particularly for local delivery. Furthermore, clinical experiences showed that effective treatments of COVID-19 require a high density of inhibitory domains to maximize blockage efficiency.[16] Nanoparticle-based strategies provide alternatives to using mAbs alone for virus capture and neutralization, because they exhibit longer retention times and allow high-density clustering of binding domains.[11,17−19]

Received: October 14, 2022
Accepted: February 9, 2023
Published: February 22, 2023

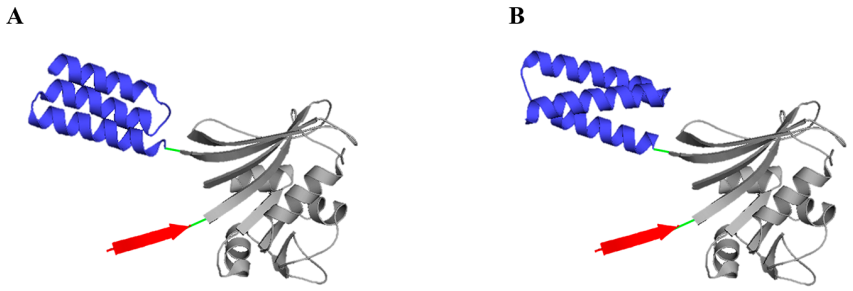

Sup35-DHFR-LCB 1

MGNYKNFNYNNNLQGYQAGFQSGSGSMISLIAAL
AVDRVIGMENAMPWNLPADLAWFKRNTLNKPVI
MGRHTWESIGRPLPGRKNIILSSQPGTDDRVTWVK
SVDEAIAACGDVPEIMVIGGGRVYEQFLPKAQKLY
LTHIDAEVEGDTHFPDYEPDDWESVFSEFHDADA
QNSHSYCFEILERRSGGSGDKEWILQKIYEIMRLLD
ELGHAEASMRVSDLIYEFMKKGDERLLEEAERLL
EEVER HHHHHH-STOP

Sup35-DHFR-LCB 3

MGNYKNFNYNNNLQGYQAGFQSGSGSMISLIAAL
AVDRVIGMENAMPWNLPADLAWFKRNTLNKPVI
MGRHTWESIGRPLPGRKNIILSSQPGTDDRVTWVK
SVDEAIAACGDVPEIMVIGGGRVYEQFLPKAQKLY
LTHIDAEVEGDTHFPDYEPDDWESVFSEFHDADAQ
NSHSYCFEILERRSGGSGNDDELHMLMTDLVYEAL
HFAKDEEIKKRVFQLFELADKAYKNNDRQKLEKV
VEELKELLERLLS HHHHHH-STOP

Figure 1. Schematic representation and sequence of Sup35-DHFR-LCB1/LCB3 fusion proteins. (A, B) Cartoon representation and sequence of Sup35-DHFR-LCB1/LCB3 fusion proteins. The SAC (residues 100−118 of Sup35 protein) fused to DHFR followed by LCB1/LCB3 SARS-CoV-2-RBD minibinders (PDB: 7JZU and 7JZM) are shown in red, gray, and blue, respectively. The three different moieties are linked by S/G linkers shown in green.

Amyloid-inspired nanomaterials are gaining momentum in nanotechnology because of their modularity, controlled self-assembly, stability, biocompatibility, and high surface/volume ratios.[20−26] A key benefit of these protein-based materials is the possibility to incorporate the desired functionality through straightforward genetic redesign, provided that the integrated domain remains folded and functionally active upon self-assembly. Despite these advantages, the large majority of developed amyloid-based materials correspond to large, insoluble, and rigid fibrils of variable length, making them not suitable for biomedical applications that require the action of the embedded protein activity to occur in human body fluids, such as in circulating SARS-CoV-2 virus capture, an application in which spherical nanoparticles functionalized with either ACE2 recombinant proteins or neutralizing antibodies are becoming an alternative to the use of individual mAbs.[17]

In this study, we took advantage of our expertise in protein design to develop highly pure and homogeneous spherical nanoparticles of an amyloid-like nature able to block the interaction between the SARS-CoV-2 spike-RBD protein and the host receptor ACE2, which we named OligoBinders. We exploited the self-assembly ability of the soft amyloid core (SAC) of Sup35 protein[27−29] and the steric impediment imposed by an adjacent globular domain[30] to generate biocompatible soluble and stable oligomers of defined size, which we engineered to display the *de novo* designed protein minibinders LCB1 and LCB3 in a favorable orientation. These two domains were developed by David Baker's lab, inspired by the minimal part of the ACE2r, but designed entirely from scratch.[16] They are small, highly stable, all-α domains consisting of 3 α-helices (Figure 1A,B) through broad shape complementary interfaces mediated by two of the three α-helices. The LCB1 and LCB3 binding sites, like in ACE2, are hidden in the closed S conformational state and need at least two RBDs to open to allow simultaneous recognition of all three binding sites. LCB1 and LCB3 form many hydrogen bonds and salt bridges with the RBD, consistent with their high potency, displaying IC_{50} values ranging from 24 pM[16] to 14 nM,[31] depending on the assay.

The employed modular approach rendered two types of spherical particles that share an amyloid-like nature but expose different folded and active minibinder domains, recognizing the S protein with half-maximal inhibitory concentration (IC_{50}) values in the pM range. Accordingly, these multivalent and high-density decorated nanostructures neutralized the fusion of SARS-CoV-2 virus-like particles (SC2-VLPs) to the membrane of ACE2r-expressing human cells with very high potency. Our OligoBinders are biocompatible, stable, effective, and easily produced, purified, and assembled, representing a conceptually novel and convenient alternative to abrogate SARS-CoV-2 internalization into human tissues.

RESULTS AND DISCUSSION

Design and Conformational Characterization of Soluble Sup35-DHFR-LCB Proteins. Soluble oligomeric amyloid-like particles have advantages for *in vivo* applications relative to the insoluble and infinite assemblies formed by amyloid fibrils. Both structures share an intermolecular β-sheet architecture,[32] and their formation is governed by the same type of contacts, with hydrophobicity, net charge, and secondary structure propensity being the main intrinsic properties determining the amyloid propensity.[33] In this scenario, because fibrils constitute a thermodynamic minimum,[34,35] obtaining homogeneous and stable oligomers that do not evolve into fibrils with time is challenging.[36,37] Some natural proteins form fibrils in which globular domains hang from the amyloid core,[38] but a long linker always separates the two regions to avoid steric repulsion, which can prevent the formation of the in-register cross-β amyloid fibrils. Recently, a general relationship between the size of the globular domains and the length of the linkers that would allow infinite fibril growth was established.[39] Using this relationship, we proposed that if the linker between the amyloid and the globular sequences is short enough but still flexible,

https://doi.org/10.1021/acsami.2c18305
ACS Appl. Mater. Interfaces 2023, 15, 11444−11457

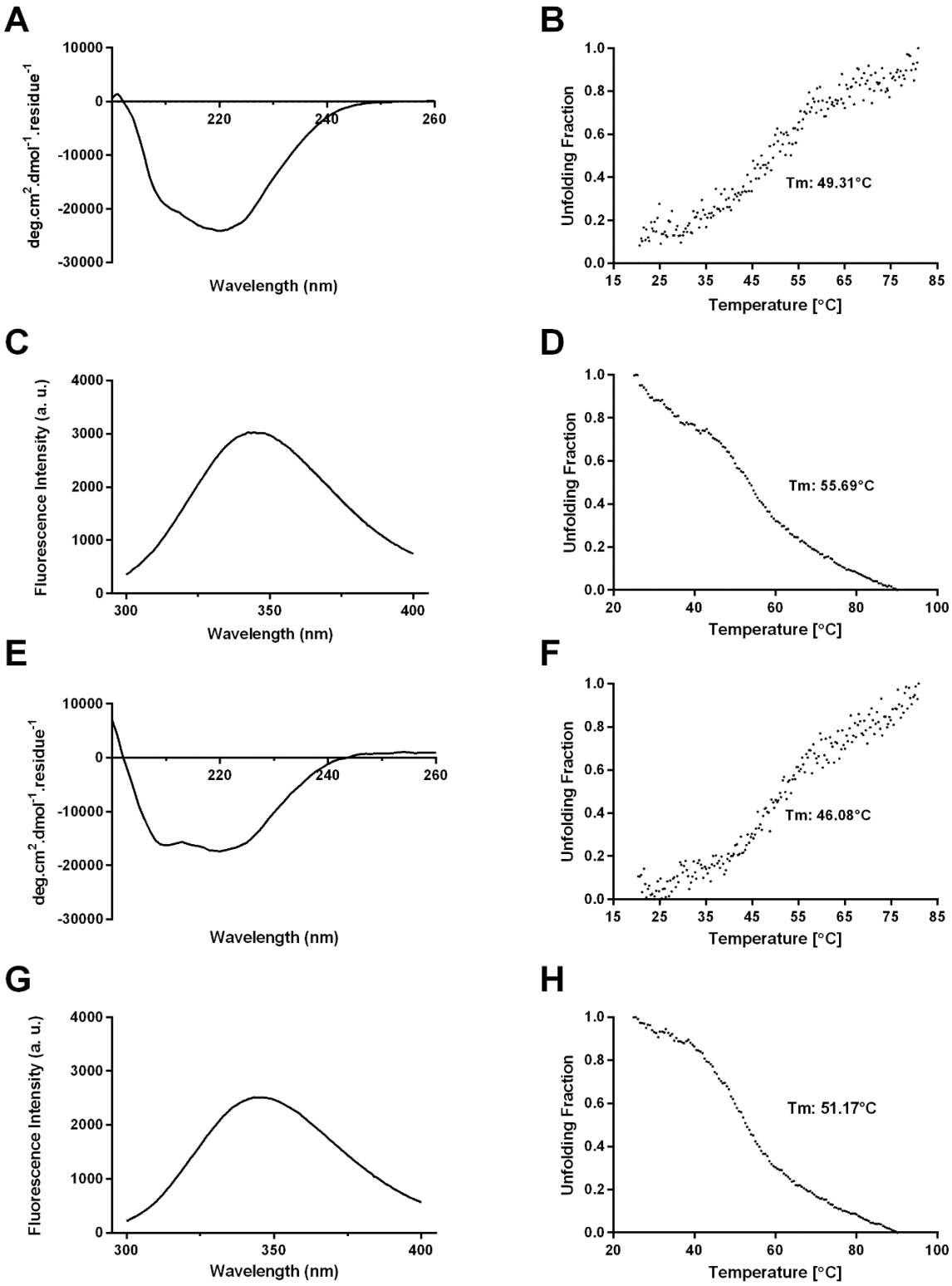

Figure 2. Biophysical characterization of soluble Sup35-DHFR-LCB1/LCB3 fusion proteins. Far-UV CD spectra of Sup35-DHFR-LCB1 (A) and Sup35-DHFR-LCB3 (E) were recorded from 200−260 nm at 25 °C in PBS pH 7.4. Normalized thermal denaturation curves of Sup35-DHFR-LCB1 (B) and Sup35-DHFR-LCB3 (F) were monitored by following the CD signal at 222 nm from 20 to 80 °C in PBS pH 7.4. Intrinsic Trp fluorescence emission spectra of Sup35-DHFR-LCB1 (C) and Sup35-DHFR-LCB3 (G) were measured in the range 300−400 nm at 25 °C after excitation at 280 nm. Normalized intrinsic fluorescence of Trp residues for Sup35-DHFR-LCB1 (D) and Sup35-DHFR-LCB3 (H) were recorded at 350 nm in the 25−90 °C temperature range using 280 nm excitation in PBS pH 7.4. Soluble Sup35-DHFR-LCB1 and Sup35-DHFR-LCB3 proteins were prepared at 10 μM in PBS.

https://doi.org/10.1021/acsami.2c18305
ACS Appl. Mater. Interfaces 2023, 15, 11444−11457

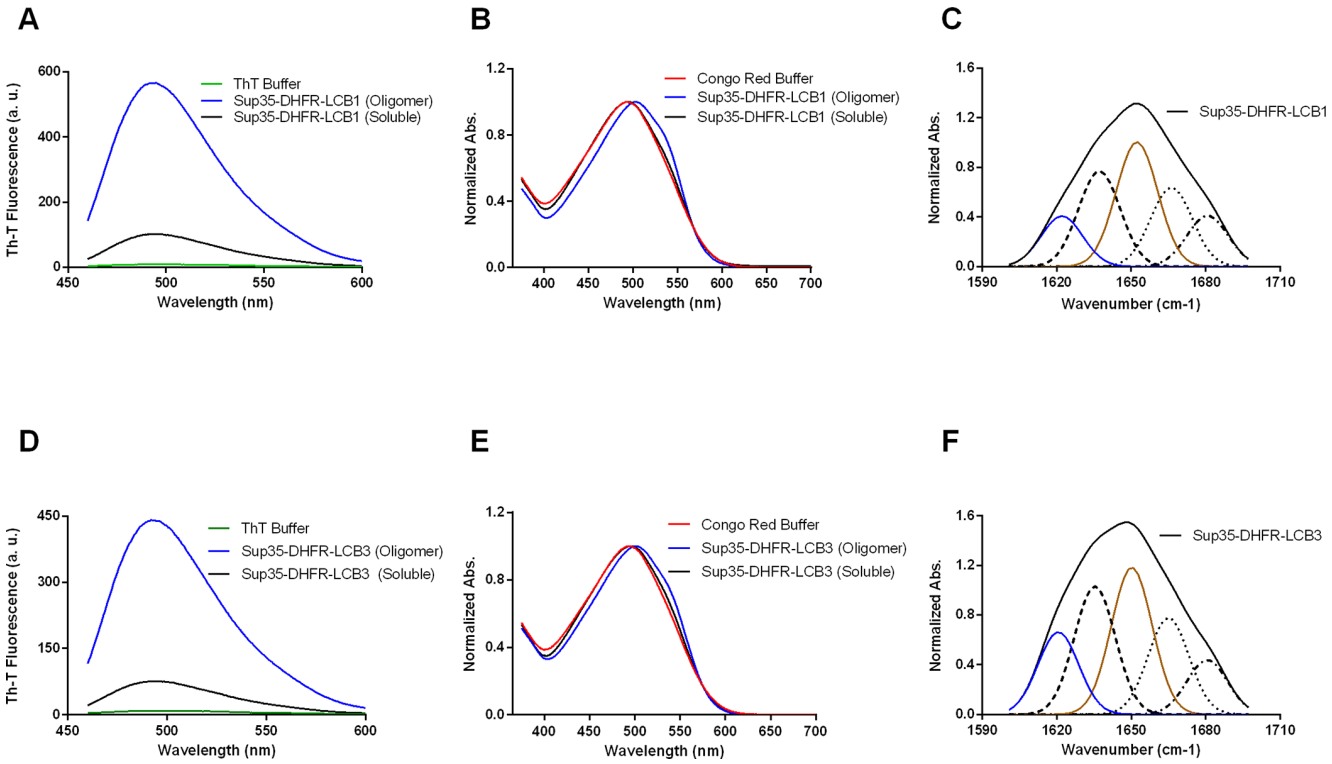

Figure 3. Biophysical characterization of oligomeric Sup35-DHFR-LCB1/LCB3 fusion proteins. (A, D) Fluorescence emission spectra of Th-T were recorded upon 445 nm excitation in the absence (green line) and the presence of 20 μM monomeric (black) and oligomeric (blue) proteins. (B, E) CR normalized absorbance spectra were recorded in the range 375−700 nm in the absence (red line) and the presence of 20 μM monomeric (black) and oligomeric (blue) proteins. (C, F) The secondary structure of oligomeric particles was derived from the deconvolution of the second-derivative ATR-FTIR absorbance spectra in the amide I region (solid black line); the fitted individual bands are indicated. Amyloid-like intermolecular β-sheet and α-helical components are shown in blue and brown, respectively.

these molecules will not assemble into amyloid fibrils; instead, they would form oligomers with a defined and limited size.[40]

Using full-atom and coarse-grained targeted molecular dynamics together with rigid body simulations, we rationalized that fusing the 19-residue SAC of the Sup35 protein (residues 100−118) to a globular protein of ∼20 kDa through a short 5-residue Gly/Ser (SGSGS) flexible linker would sterically hinder the formation of a fibrillar zipper and result in the assembly of amyloid-like oligomers of defined dimensions in which the embedded protein can remain in a folded conformation.[40] Subsequently, we demonstrated the accuracy of these predictions using dihydrofolate reductase (DHFR) as a model protein, with the Sup35-DHFR fusion forming enzymatically active oligomeric structures.[27]

The above-described strategy permits the generation of tailored spherical nanoparticles for different purposes. With the intention of targeting and neutralizing SARS-CoV-2, we incorporated LCB1 or LCB3 minibinders at the C-terminus of Sup35-5aa-DHFR construct. LCB molecules are *de novo* designed small and stable proteins that can tightly bind SARS-CoV-2-S-RBD.[16] Therefore, the resulting plasmid encoded a tripartite fusion construct consisting of Sup35-SAC, DHFR, and LCB1/LCB3 domains, separated by Gly/Ser-based linkers. The primary sequence and cartoon representation of Sup35-DHFR-LCB1 and Sup35-DHFR-LCB3 constructs are detailed in Figure 1A,B.

The two Sup35-DHFR-LCB1/LCB3 monomeric proteins were recombinantly expressed and purified from the soluble cellular fraction of *Escherichia coli BL21* cells using metal ion affinity chromatography (Ni-NTA chromatography) with a yield of 83 and 134 mg/L, respectively (Figures S1A,B and S2A,B).

The secondary structure of soluble recombinant Sup35-DHFR-LCB1/LCB3 proteins was analyzed by far-UV circular dichroism (CD) in the 200−260 nm range (Figure 2A,E). For both molecules, α-helical signals at 208 and 222 nm were evident. This is consistent with α-helix conformations accounting for 35% and 38% of the secondary structure in LCB1- and LCB3-containing constructs, respectively (Figure 1). Next, the tryptophan (Trp) intrinsic fluorescent signal was used as a probe for the Sup35-DHFR-LCB1/LCB3 tertiary structure. For both proteins, the intrinsic fluorescence emission spectra showed a maximum at ∼345 nm, indicative of Trp residues being partially hidden from the solvent as expected for the native conformations of DHFR and LCB1 (as a note, LCB3 does not have Trp) (Figure 2C,G).

The stability of soluble Sup35-DHFR-LCB1/LCB3 proteins against thermal unfolding was evaluated by monitoring the changes in CD and fluorescence emission upon heating. The CD signal was measured at 222 nm, to report on α-helical secondary structure (Figure 2B,F) and the fluorescence signal at 350 nm to monitor changes in the local environment of Trp residues (Figure 2D,H). Sup35-DHFR-LCB1/LCB3 proteins' thermal denaturation curves evidenced cooperative but multistate unfolding profiles, as expected for multidomain fusions, with overall mid transitions occurring at ∼50 °C.

https://doi.org/10.1021/acsami.2c18305
ACS Appl. Mater. Interfaces 2023, 15, 11444−11457

Overall, the biophysical analysis of soluble Sup35-DHFR-LCB1/LCB3 proteins suggested a folded conformation for the purified polypeptides.

Sup35-DHFR-LCB1/LCB3 Spontaneously Self-Assembles into Amyloid-like Oligomers. Monomeric Sup35-DHFR-LCB1/LCB3 proteins were incubated at an initial concentration of 150 μM in 20 mM sodium phosphate buffer pH 8 for 4 days at 37 °C. To obtain a pure oligomeric fraction, highly aggregated and monomeric species were removed at the end of the reaction. To this aim, samples were first ultracentrifuged to remove insoluble aggregates and later filtered through a 100 kDa filter to eliminate nonassembled monomers. By absorbance measurements, an oligomeric yield of 93% and 57% was estimated, relative to the initial protein concentration in the reaction for LCB1 and LCB3 protein fusions, respectively. The purity of the oligomers was confirmed by native-PAGE (Figures S1C and S2C).

The amyloid-like nature of the purified assemblies was assessed by monitoring the binding to the amyloid-specific dye thioflavin-T (Th-T) (Figure 3). The oligomeric Sup35-DHFR-LCB1/LCB3 fraction exhibited a significant fluorescence signal, whereas their soluble counterparts had negligible Th-T binding (Figure 3A,D). The Congo red (CR) dye was used to corroborate the amyloid nature of the assemblies. In agreement with Th-T data, the CR absorbance spectrum displayed a red-shift to ~540 nm typical of amyloid binding for both oligomeric fractions, which was absent in the respective soluble forms (Figure 3B,E).

Next, we assessed these assemblies' secondary structure content, employing attenuated total reflectance Fourier-transform infrared (ATR-FTIR) spectroscopy. FTIR spectra were recorded in the amide I region (1700−1600 cm^{-1}), corresponding to the absorption of the main chain carbonyl group. The maxima of the deconvoluted curves under the absorbance spectra allowed for correlating the wavenumber with defined secondary structure elements (Figure 3C,F, Table 1).

Table 1. Secondary Structure Assignments of Amide I Band Components in Purified Assemblies by ATR-FTIR Spectroscopy[a]

band assignment	Sup35-DHFR-LCB1 wavenumber (cm^{-1})	area (%)	Sup35-DHFR-LCB3 wavenumber (cm^{-1})	area (%)
intermolecular β-sheet	1622.1	13%	1620.6	16%
intramolecular β-sheet	1637.2	23%	1635.4	25%
α-helix	1652.4	31%	1650.2	29%
β-turn/loop + turn	1666.3	19%	1665	19%
β-sheet	1680.8	13%	1680.6	10%

[a]The percentage of contribution to the total area of the absorbance spectra is indicated for the different types of secondary structure elements, as estimated from the deconvolution of the spectra shown in Figure 3C,F.

As was expected from the dye binding properties, we could detect a signal at 1621/1622 cm^{-1}, which can be assigned to the intermolecular β-sheet structure characteristic of amyloids. Importantly, in addition to the band at 1635/1637 cm^{-1}, attributable to the native β-sheet in the DHFR moiety, we identified a band accounting for 29−30% of the spectra at 1650/1652 cm^{-1} indicative of an α-helical conformation in the oligomers, despite their amyloid-like features, the majority of which would necessarily correspond to the LCB domains, suggesting that they were folded correctly and potentially active in the oligomeric state.

Sup35-DHFR-LCB1/LCB3 Oligomers are Spherical Nanoparticles. To investigate the macromolecular nature of Sup35-DHFR-LCB1/LCB3 amyloid-like soluble oligomers, they were imaged by transmission electron microscopy (TEM) (Figure 4). Samples were deposited onto copper grids and negatively stained with 2% uranyl acetate. Representative TEM images evidenced the presence of abundant isolated spherical nanoparticles of 21/22 nm in diameter (Figure 4A,C, Table 2).

The homogeneity and size distribution of the nanoparticles was then analyzed by dynamic light scattering (DLS) (Figure 4B,D). In good agreement with TEM images, DLS measurements rendered an average size of 20/22 nm, with 99.9% homogeneity and a polydispersity index of 0.3 for both proteins (Table 2). We named the highly homogeneous spherical nanoparticles displaying the LCB1 and LCB3 domains as OligoBinder-1 and OligoBinder-3, respectively.

The molecular weight (MW) for OligoBinder-1 and OligoBinder-3, as derived from the mass distribution DLS data, was estimated using an empirical mass vs size calibration curve, obtaining average sizes of 731 and 791 kDa, respectively. Considering the MW of their monomeric constituents, OligoBinder-1 and OligoBinder-3 were calculated to consist of 25 and 27 subunits on average, respectively.

We tested the stability of the two nanoparticles when incubated at different pHs. The size of OligoBinder-1 and OligoBinder-3 before and after 24 h of incubation was evaluated at pH 6.5, 7.0, 7.5, and 8.0 by DLS (Figure S3) and TEM (Figure S4). Except for OligoBinder-3 at pH 6.5, for which a discrete increase in size was observed, no changes in the diameter of the particles were evidenced under any of the conditions. To further confirm that oligomeric nanoparticles were not disassembled during incubation, samples incubated for 24 h at the different pHs were loaded onto native-PAGE gels (Figure S3). The analysis confirmed the absence of monomeric molecules for both OligoBinders in all assayed conditions. Consistent with the DLS data, a high-molecular-weight band was observed for OligoBinder-3 at pH 6.5, indicating partial association at this pH. This likely responds to the fact that the pI of LCB3 (5.9) is higher than that of LCB1 (5.3).

OligoBinders Effectively Compete with the Spike RBD−ACE2 Receptor Interaction. The interaction between the RBD from viral S glycoprotein homotrimers and cellular ACE2 receptors is indispensable for SARS-CoV-2 to enter the host cell. Accordingly, it is assumed that molecules able to compete with S protein−ACE2r interaction would exert a neutralizing effect. To elucidate the binding capacity of our multivalent bioengineered particles, OligoBinder-1 and OligoBinder-3 were immobilized onto a membrane, in the concentration range from 0.04 to 0.4 μg, and incubated with recombinantly produced S protein RBD, N-terminally tagged with YFP (0.5 ng/μL),[41] as a fluorescent reporter (YFP-S-RBD). As shown in Figure 5, OligoBinders can bind S-RBD protein in a concentration-dependent manner. In order to discard potential unspecific binding of YFP-S-RBD to non-LCB domains in the fusion, a construct containing Sup35-SAC fused to DHFR and the Z-domain (Sup35-DHFR-Z) was produced. The Z-domain is an engineered analogue of the B domain of *Staphylococcus aureus*,[42] selected because of its size, about 6.5

https://doi.org/10.1021/acsami.2c18305
ACS Appl. Mater. Interfaces 2023, 15, 11444−11457

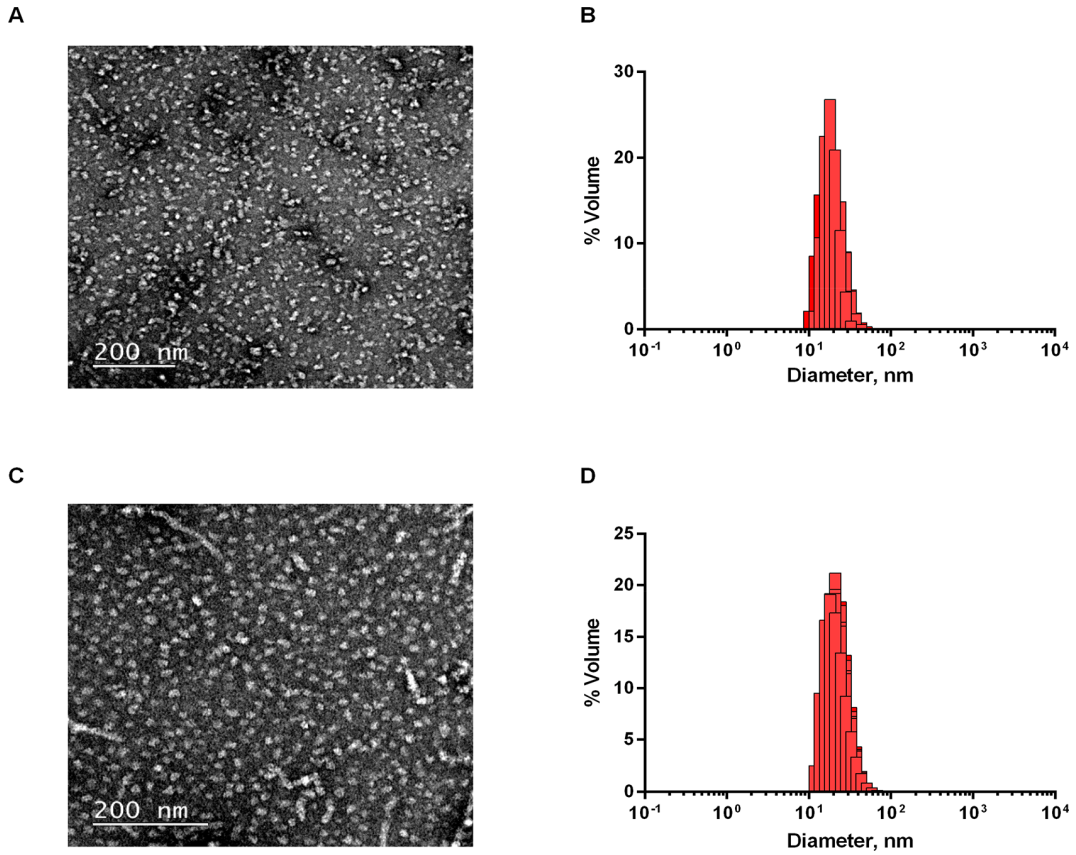

Figure 4. Morphology characterization and size distribution of Sup35-DHFR-LCB1/LCB3 oligomeric assemblies. Transmission electron micrographs of negatively stained Sup35-DHFR-LCB1 (A) and Sup35-DHFR-LCB3 (C) oligomer solutions. The scale bar is 200 nm in size. Size distribution of Sup35-DHFR-LCB1 (B) and Sup35-DHFR-LCB3 (D) oligomeric assemblies characterized by DLS.

Table 2. Size of Purified Amyloid Oligomeric Nanoparticles Determined by TEM Micrographs and DLS[a]

nanoparticle	TEM (nm)	DLS (nm)
OligoBinder-1	21.6 ± 4.7	20.3 ± 5.8
OligoBinder-3	21.0 ± 6.4	21.9 ± 8.0

[a]The diameter of particles visualized by TEM was determined by ImageJ software [mean ± standard deviation (SD)], and DLS mean size values ± SD were obtained by considering the volume-based distribution.

kDa, and its fold. The Z-domain adopts a helical bundle-like structure formed by 3 α-helices topologically equivalent to those of LCB1 and LCB3 (Figure S5).

To guarantee that Sup35-DHFR-Z constructs share a similar oligomeric disposition, they were biophysically characterized (Figure S5). The Z-domain is an antibody high-affinity binder, and as such, in contrast to oligomers decorated with LCB1 and LCB3 minibinders, Sup35-DHFR-Z nanoparticles did not retain any fluorescent signal upon incubation with YFP-S-RBD, pointing to the specificity of the LCB1 and LCB3 domains displayed in OligoBinders as the moieties recognizing the viral S protein RBD domain (Figure 5). To validate this extent, we assayed as positive control a rabbit polyclonal antibody raised against SARS-CoV-2 spike (IC_{50} for RBD binding: 5.4−11.4 nM); as expected, binding of YFP-S-RBD to the antibody in the membrane was observed. However, when used at the same concentration, the fluorescent signal was lower than that for OligoBinders, which suggests that the nanoparticles bind better to the target in this qualitative assay. As a trend, OligoBinder-1 dots exhibit a higher fluorescent signal than OligoBinder-3. However, the differences in intensities are only statistically significant at the highest tested nanoparticle quantities.

Next, for quantifying the interaction between S-RBD and ACE2r in the presence of OligoBinder-1 and OligoBinder-3, we used a homogeneous bioluminescent immunoassay based on the interaction between Fc-tagged SARS-CoV-2 spike RBD and human ACE2r, and its detection by secondary antibodies labeled with NanoLuc luciferase fragments LgBit and SmBit.[43] Briefly, the interaction of S-RBD and ACE2r, incubated with their corresponding secondary antibodies bearing one subunit of NanoBiT Luciferase, reconstitutes the active enzyme to generate light (Figure 6A).

In the presence of neutralizing compounds, the luminescent signal decreases inversely proportional to the strength of the S-RBD−molecule interaction, since this contact competes with the S-RBD−ACE2r one and impedes luciferase reconstitution. In this way, serially diluted OligoBinder-1 and OligoBinder-3 were incubated with SARS-CoV-2 RBD-rabbit Fc (rFc-RBD) and human ACE2r-mouse Fc (mFc-ACE2), followed by the addition of an antibody mix containing anti-mouse Ab-LgBiT and anti-rabbit Ab-SmBiT and revealed with the Lumit detection reagent. OligoBinder-1 and OligoBinder-3 showed IC_{50} values of 57.2 and 49.4 pM in this assay, respectively (Figure 6B). These values are in the same range as or better than the ones recorded with the same assay for four different investigational anti-SARS-CoV-2 spike RBD antibodies of chimeric mouse/human (Sino Biological 40150-D001 and

https://doi.org/10.1021/acsami.2c18305
ACS Appl. Mater. Interfaces 2023, 15, 11444−11457

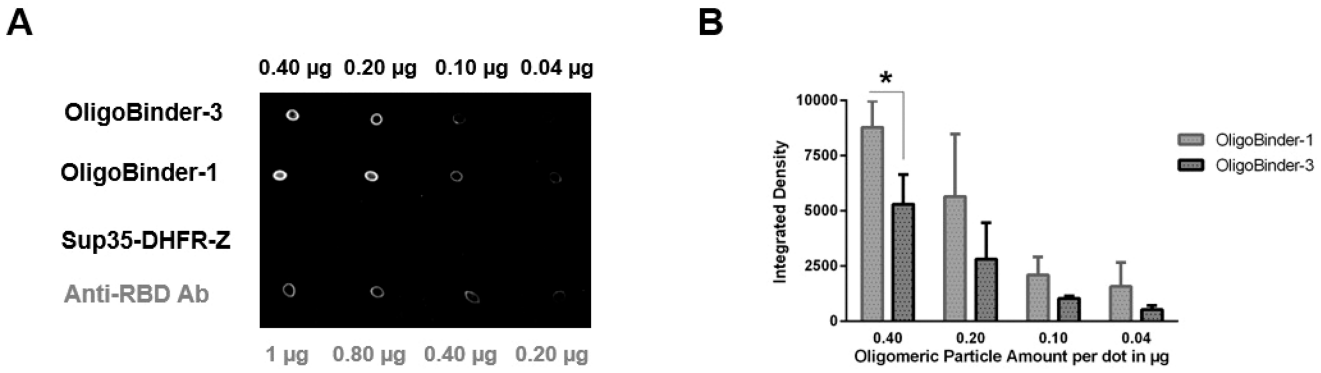

Figure 5. Functional assessment of amyloid oligomeric nanoparticles. (A) Dot blot of amyloid OligoBinder-1 and OligoBinder-3 nanoparticles in different amounts (0.40, 0.20, 0.10, and 0.04 μg), loaded onto a membrane. Negative control corresponds to the amyloid-like oligomer of Sup35-DHFR-Z, which shares conformation with OligoBinders. The positive control is a rabbit anti-RBD antibody. The membrane was incubated with the YFP-S-RBD construct (0.5 ng/μL). (B) Bar charts representing the mean of the fluorescence of each dot over the corresponding integrated area. SD was calculated from three independent dot blot assays. * indicates p value <0.05.

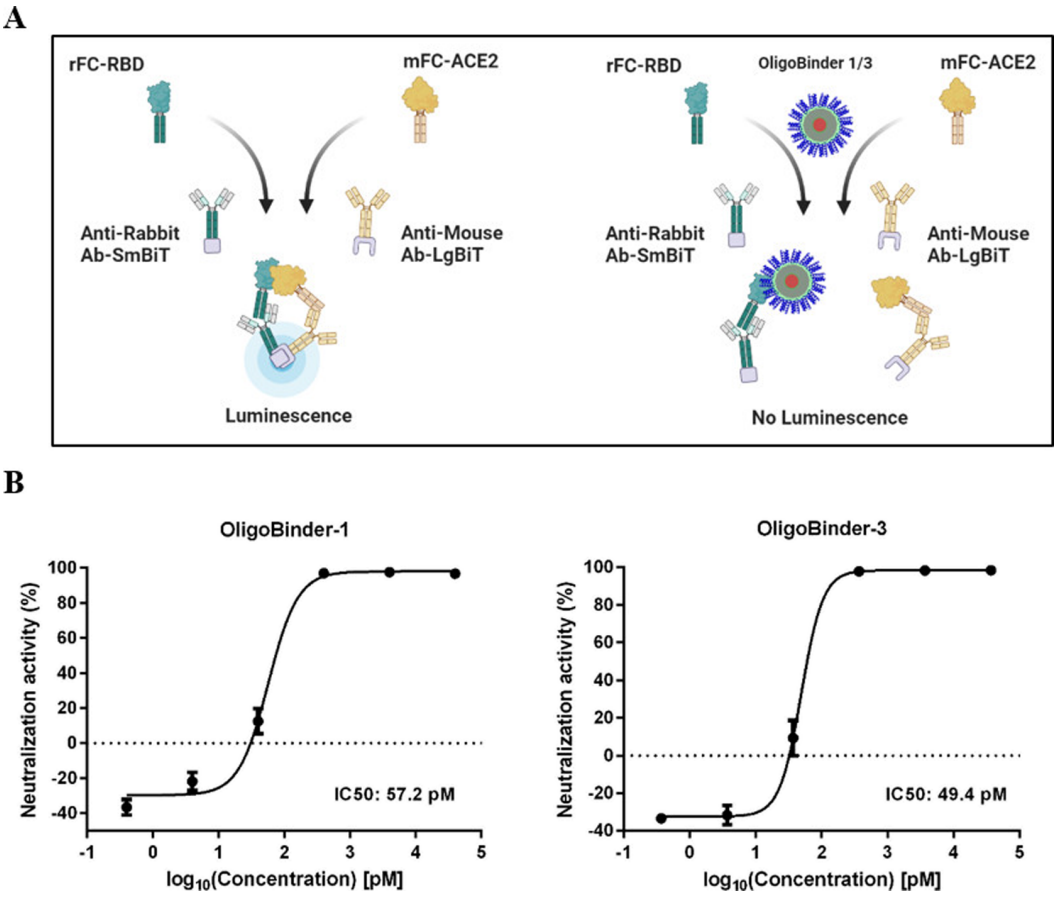

Figure 6. Neutralization effect of OligoBinder-1/3 nanoparticles against RBD:hACE2r interaction. (A) Schematic representation of the Lumit SARS-CoV-2 spike RBD:hACE2r immunoassay. Created by BioRender.com. (B) Interfering effect of amyloid oligomeric nanoparticles for RBD:hACE2r with the Lumit SARS-CoV-2 spike RBD:hACE2r immunoassay. Results come from the mean calculation of two technical replicates ± SD. IC_{50} values were calculated using a nonlinear regression (least-squares) fitting method.

40150-D002) and human origin (Active Motif 91361 and Biolegend 938502), which exhibited IC_{50} values of 1870, 250, 430, and 370 pM, respectively.

Overall, our results indicated that the multivalent OligoBinder-1 and OligoBinder-3 efficiently use the previously described high affinity of LCB1 and LCB3 domains[16] to bind SARS-CoV-2 spike RBD with a potency equivalent to the one shown by investigational antibodies.

OligoBinder-1 and OligoBinder-3 Block Viral Entry. Similar to neutralizing antibodies, molecules able to bind the S glycoprotein on the viral surface might prevent the entry of the virus into the host cell, thus offering protection against infections. Therefore, we investigated the ability of Oligo-

https://doi.org/10.1021/acsami.2c18305
ACS Appl. Mater. Interfaces 2023, 15, 11444−11457

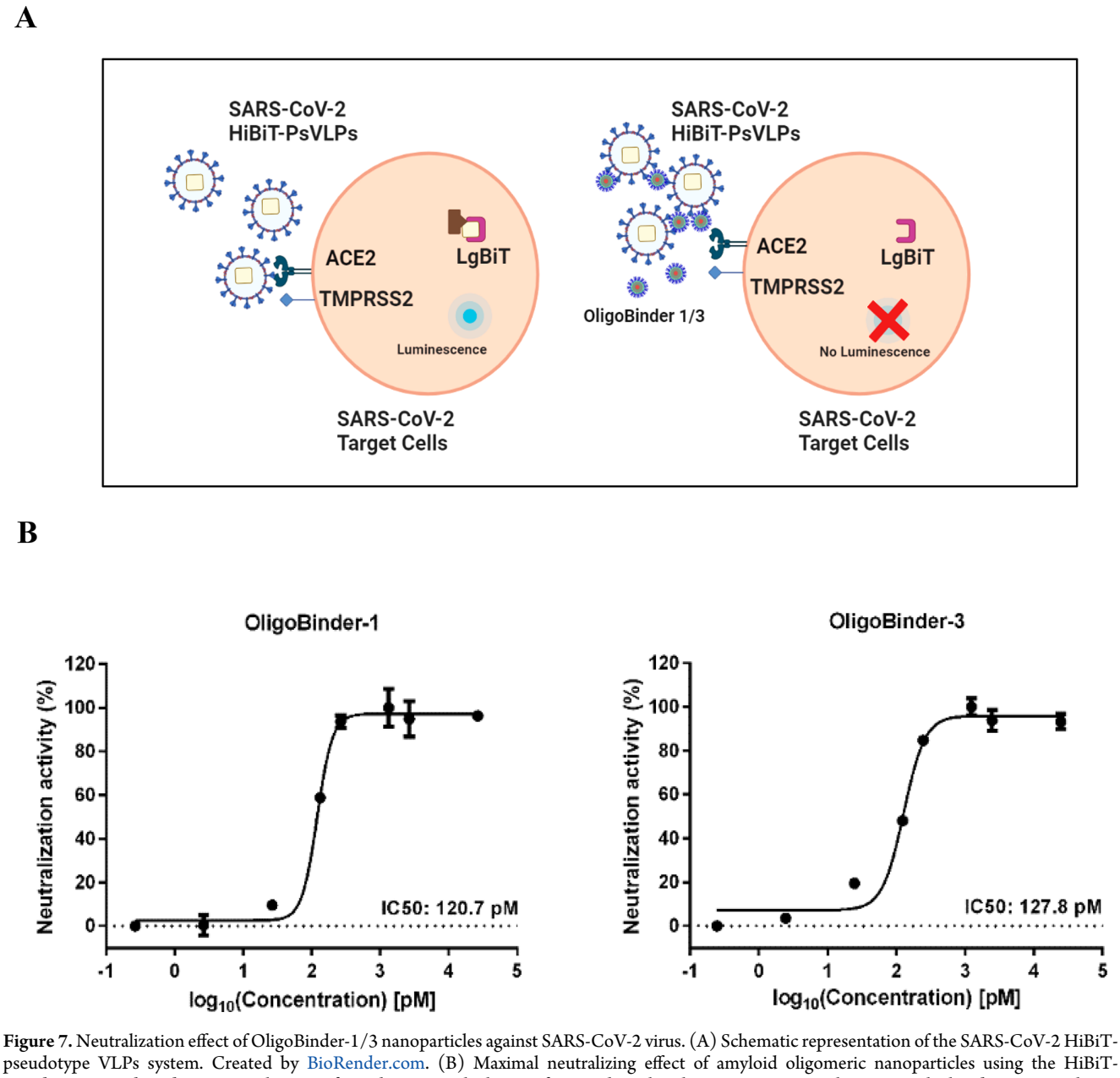

Figure 7. Neutralization effect of OligoBinder-1/3 nanoparticles against SARS-CoV-2 virus. (A) Schematic representation of the SARS-CoV-2 HiBiT-pseudotype VLPs system. Created by BioRender.com. (B) Maximal neutralizing effect of amyloid oligomeric nanoparticles using the HiBiT-pseudotype VLP-based assay. Results come from the mean calculation of two technical replicates ± SD. IC_{50} values were calculated using a nonlinear regression (least-squares) fitting method.

Binder-1 and OligoBinder-3 to block the entry of the virus into human cells.

Because of safety restrictions to work with SARS-CoV-2 at our institution, we used HiBiT bioluminescence technology instead, which is a well-validated technology for SARS-CoV-2 investigation.[44−46] It employs SARS-CoV-2 pseudotyped virus-like particles (SC2-VLPs)[47] that resemble the virus structurally and contain the spike protein at their surface but are noninfectious due to the lack of viral genetic material. Briefly, when HiBiT-tagged VLPs pseudotyped with SARS-CoV-2 S protein are added to engineered human ACE2-HEK293T cells that stably express ACE2r at its surface and LgBiT in their cytosol, the spike−ACE2r interaction results in membrane fusion, and HiBiT is released into target cells, where it binds to LgBiT to generate a luminescent signal in the presence of substrate. However, in the presence of molecules interfering with SARS-CoV-2 entry, the entry/fusion processes of SC2-VLPs are blocked, thereby preventing HiBiT internalization, and no luminescence is produced (Figure 7A).

To assess the neutralizing potency of our nanoparticles, SARS-CoV-2 S (G614) HiBiT-pseudotype VLPs were incubated with OligoBinder-1 and OligoBinder-3 in the range 0.2−40000 pM and then added to the hACE2-HEK293T (LgBiT) target cells, and the neutralizing IC_{50} values were determined (Figure 7B). Consistent with the binding data obtained in the previous assays, the neutralization IC_{50} values were 120.7 and 127.8 pM for OligoBinder-1 and OligoBinder-3, respectively. These values are in the same range as or better than the IC_{50} values obtained for bamlanivimab,[48] imdevimab,[49] or etesevimab,[50] when tested using the same HiBiT assay (Table 3). These are mAbs against the spike (S) protein of SARS-CoV-

https://doi.org/10.1021/acsami.2c18305
ACS Appl. Mater. Interfaces 2023, 15, 11444−11457

2 that are being used individually or in combination as treatment and prophylaxis for COVID-19.[51]

Table 3. SARS-CoV-2 HiBiT-PsVLP Assay Response to Neutralizing Antibodies and OligoBinders

anti-SARS-CoV-2 spike mAb/binder	IC_{50} (ng/mL)	IC_{50} (pM)
bamlanivimab[a]	34	232.9
imdevimab[a]	72	499.5
etesevimab[a]	230	1629.1
OligoBinder-1	88.2	120.7
OligoBinder-3	101.1	127.8

[a]Data as provided by Promega Biotech Ibérica, S.L.

Biocompatibility and Stability of OligoBinder-1/3 Nanoparticles. Every nanomaterial intended for biomedical purposes should be biocompatible. It has been reported that certain amyloid-based nanomaterials might elicit cytotoxicity, especially in the oligomeric states.[52] We wanted to discard this possibility for our nanoparticles. Therefore, we determined the metabolic activity of human cells treated with OligoBinder-1 and OligoBinder-3. To this aim, purified oligomers were added to HeLa cultured cells and nontumor MRC-5 cells at different concentrations, ranging from 1 to 10 μM. After 72 h of incubation, the assemblies' toxicity was assessed using the PrestoBlue fluorescent reagent, a cell-permeable resazurin-based solution that is reduced by metabolically active cells, with fluorescence being a quantitative measure of cell viability. Figure 8 shows that, compared to the control group, OligoBinders did not reduce cell viability at any of the tested concentrations, meaning that these spherical nanostructures are biocompatible.

The bioavailability of active protein-based materials is critical for their biomedical use, since polypeptides are intrinsically vulnerable to plasma proteolytic enzymes. Therefore, we investigated the stability of OligoBinder-1 and OligoBinder-3 in plasma for 48 h at room temperature (RT). Nanoparticles in plasma at time zero were used as a positive control, and plasma alone was loaded to discard any unspecificity of the used anti-His tag antibodies. The His tag is at the C-terminus of the two tripartite fusions, and proteolysis should be easily monitored if it occurs. As shown in Figure S6, OligoBinder-1 and OligoBinder-3 remained stable for 24 h in plasma.

Once confirmed that OligoBinders were not proteolytically processed in plasma, we further monitored their stability in this biological fluid by measuring their eventual disassembly into their intact individual subunits. To this aim, first, we injected OligoBinder-1 or OligoBinder-3, as well as their monomers, into a calibrated SEC column to map the fractions in which the natively assembled particles and potential dissociated monomers would elute. Both oligomers and monomers rendered a single peak, indicative of their homogeneity (Figure S7A,B). Molecular weights of 813 and 851 kDa were calculated for OligoBinder-1 and OligoBinder-3, in good agreement with the sizes obtained from DLS analysis.

In a next step, we added the oligomers to plasma and, at time 0 h and after 24 h of incubation, chromatographed the mixture and collected the fractions corresponding to native oligomers and potential monomers (Figure S7C−F). We then detected Sup35-DHFR-LCB1/LCB3 subunits in these fractions by immunoblotting using an anti-His tag antibody. The experiment confirmed that the integrity of the oligomeric particles did not change upon incubation in plasma, since the signals corresponding to the oligomers do not vary significantly with time, and no monomers were detected for either of the two nanoparticles (Figure S7I,J).

CONCLUSION

As we enter the third year of the COVID-19 pandemic, we are still far from the end of it. An incredible effort has been put into developing therapeutic agents such as new vaccines against SARS-CoV-2 or antiviral repurposed drugs. There is no doubt that vaccines represent the first barrier of protection against the virus. Vaccination conveys less severe illness and is associated with lower patient mortality, but older adults and other people with compromised immune systems might not develop or maintain an adequate immune response to vaccines. In addition, repurposing antiviral drugs usually takes a long time.[53−55]

Therefore, we will only succeed in defeating the pandemic by combining existing treatments with novel approaches. Because COVID-19 disease manifests when SARS-CoV-2 enters into host cells through the interaction between the S protein and ACE2r, research is focused on discovering molecules intended to target them, thus interfering with their binding.[56,57]

Our strategy produced highly pure assemblies of defined size by incorporating the LCB1 and LCB3 domains through a short linker at the C-terminus of the Sup35-DHFR construct. This strategy has been previously shown to generate spherical nanoparticles of an amyloid-like nature but devoid of any toxicity and having mesoscopic properties of interest.[27] We exploited the self-assembling properties of this tripartite fusion to generate high-surface/volume-ratio functionalized nanostructures that can target and neutralize SARS-CoV-2.

OligoBinders are biocompatible soluble oligomeric particles exposing functional LCB minibinders, whose properties endorse

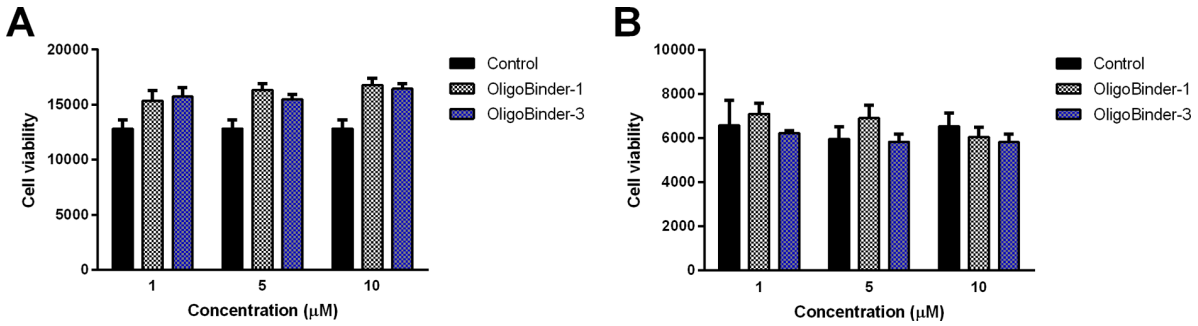

Figure 8. Cytotoxicity of OligoBinders. Cell viability of HeLa cells (A) and MRC-5 cells (B) after 72 h of incubation in the presence of different concentrations of oligomeric nanoparticles. Results are presented as means ± SD, $n = 3$.

https://doi.org/10.1021/acsami.2c18305
ACS Appl. Mater. Interfaces 2023, 15, 11444−11457

this nanomaterial with the ability to bind to the S protein RBD and inhibit the RBD/ACE2-receptor protein−protein interaction in the pM range, interfering with the fusion of SC2-VLPs to human host cells with higher potency than that observed for neutralizing mAbs in the same assay. The amyloid-like nature of the assembly provides these nanoparticles with high stability, as shown by their resistance to proteolysis and dissociation in plasma. The trick resides in taking advantage of the strength of the short intermolecular contacts that characterize the amyloid fold without forming large insoluble fibrillar assemblies. The spherical shape and defined size of OligoBinders make them comparable to other nanostructures of inorganic origin, with the unique property that they display functional protein domains in active conformations ready for binding. In addition, these assemblies have a multimeric nature that might potentially enable engagement of all 3 RBDs in a single S trimer; whether this is the reason for the higher apparent neutralizing potency of OligoBinders relative to therapeutic antibodies in the HiBiT-PsVLP assay should be further investigated.

LCB1 and LCB3 bind to the viral glycoprotein in different modes,[16] but our assays did not detect significant differences in their neutralizing activities; in the absence of structural information reporting on the conformation of these domains in the oligomer and the way they bind to the trimeric spike protein, the reason for this similar activity remains uncertain; still, the fact that the two domains dock with opposing orientations in the crevice created by the RBD motif suggests that they might be used in combination.

Importantly, the monomeric components of OligoBinders are amenable to large-scale production in microbial cell factories, like *E. coli*, and their assembly occurs spontaneously after incubation, enabling their cost-effective manufacture; moreover, they might not require cold chain storage due to their stability. Altogether, the two novel functional protein-based nanoparticles we describe here might be potentially exploited for applications in biomedicine, such as self-administered nasal treatment, or biotechnology, including the development of SARS-CoV-2 diagnostic kits, or as potential prophylactic agents.

In conclusion, our strategy is simple, modular, and can be adapted to target any virus of interest by incorporating the corresponding inhibitory domain in the fusion. Furthermore, it offers the possibility to engineer oligomeric nanoparticles combining two or more functional domains that simultaneously target different binders or diverse binding sites in the same protein, to create potentiated antiviral molecules in the future.

MATERIALS AND METHODS

Protein Expression and Purification. The cDNA of LCB1 and LCB3 protein sequences[16] were subcloned into a pET28a vector (Addgene), containing the sequence for SAC Sup35-linker-DHFR with a 6x-His-tag (see the complete sequence in Figure 1).

The two plasmids were transformed into *E. coli* BL21 (DE3) strain. Then, the transformed cells were grown overnight in LB medium containing 50 μg/mL kanamycin at 37 °C with agitation. Then, 1:100 dilutions from overnight cultures were used to inoculate fresh LB medium containing 50 μg/mL kanamycin, and cultures were grown at 37 °C with agitation until reaching an optical density (OD 600 nm) of 0.6 and induced using 1 mM IPTG at 20 °C for 16 h. Samples from noninduced and induced cultures were taken to analyze soluble and insoluble fractions by 15% SDS-PAGE. Cells were harvested by centrifugation at 6238*g* for 20 min at 4 °C. The cell pellet was washed in 30 mL of phosphate buffered saline (PBS, pH 7.4) by centrifugation at 3220*g* for 20 min at 4 °C and kept at −80 °C. Then, the collected cell pellet was resuspended in lysis buffer [30 mM Tris-HCl pH 8.0, 300 mM NaCl, EDTA-free protease inhibitor cocktail tablets (Thermo Scientific), 1 mM PMSF, and 1 μg/mL DNase]. Cells were then lysed by sonication on ice. Lysates were centrifuged at 27216*g* for 30 min at 4 °C, and the clarified supernatants were filtered through a 0.45 μm filter and loaded into a Ni-NTA nickel column pre-equilibrated with wash buffer (30 mM Tris-HCl pH 8.0, 300 mM NaCl, 20 mM imidazole) and eluted with elution buffer (30 mM Tris-HCl pH 8.0, 300 mM NaCl, 500 mM imidazole). Eluted samples were loaded into a Superdex 75 increase 10/300 GL (GE Healthcare) size exclusion column using PBS pH 7.4.

The protein fraction of cell homogenates and purity of the samples were confirmed by 15% SDS-PAGE. Protein concentration was determined by measuring absorbance at 280 nm in a SPECORD 200 Plus spectrophotometer (Analytik Jena, Jena, Germany). Fractions containing purified proteins were snap-frozen in liquid nitrogen and stored at −80 °C.

Circular Dichroism Spectroscopy. Sup35-DHFR-LCB1 and Sup35-DHFR-LCB3 proteins were diluted at 10 μM in 1× PBS. Far-UV CD spectra were acquired in the range 200−260 nm, at 25 °C, in a Jasco J-815 CD spectropolarimeter (Jasco Corporation). The CD spectra were obtained from the average of 12 accumulations by continuous scanning at 0.5 nm intervals, a response time of 1 s at a scanning speed of 100 nm/min, and a bandwidth of 1 nm.

To study the thermal stability by far-UV CD, Sup35-DHFR-LCB1 and Sup35-DHFR-LCB3 proteins were prepared at 10 μM in PBS pH 7.4. The ellipticity at 222 nm, corresponding to the α-helical conformation, was registered at 1 °C intervals, with a heating rate of 0.5 °C min^{-1} from 20 to 80 °C in a Jasco J-815 CD spectropolarimeter (Jasco Corporation) equipped with a Peltier Jasco CDF-426S/15 temperature controller and Jasco MCB-100 mini water circulation bath. To determine the T_m, transition curves were normalized and fitted using Kaleida Graph software.

Intrinsic Tryptophan Fluorescence. Intrinsic tryptophan fluorescence spectra of Sup35-DHFR-LCB1 and Sup35-DHFR-LCB3 at 10 μM were analyzed at 25 °C in PBS pH 7.4 using a Jasco FP-8200 spectrofluorometer (Jasco Corporation). The average of 3 accumulations were measured in the range 300−400 nm every 0.5 nm, with 0.1 s response time, using an excitation wavelength of 280 nm.

Thermal denaturation was followed by intrinsic fluorescence emission of Trp recorded at 350 nm, after an excitation wavelength of 280 nm, with a heating rate of 0.5 °C min^{-1} from 25 to 90 °C and 0.5 °C intervals, in a Jasco FP-8200 spectrofluorometer (Jasco Corporation) equipped with a Jasco ETC-814 Peltier temperature control system and Jasco MCB-100 water circulation minibath. Transition curves were normalized and fitted using Kaleida Graph software to calculate the T_m.

Preparation of Oligomeric Particles. For the preparation of oligomeric particles of Sup35-DHFR-LCB1 and Sup35-DHFR-LCB3, proteins in 20 mM sodium phosphate buffer pH 8, at a final concentration of 150 μM, were filtered through 0.22 μm filters. Samples were incubated at 37 °C with agitation (600 rpm) for 4 days.

After incubation, the solution was ultracentrifuged for 1 h at 400000*g* at 20 °C to eliminate any insoluble aggregates. Then, to remove remaining monomers, 500 μL of supernatant was collected into an Amicon Ultra cellulose membrane centrifugal filter of 100 kDa (Millipore) and centrifuged at 9600*g* for 2 min. The concentrated solution was then washed 3 times with 400 μL of 20 mM sodium phosphate buffer and concentrated down to 100 μL.

Buffer exchange of Oligobinder-1 and OligoBinder-3 was performed by diluting samples 20× in the corresponding buffer with different pH values (6.5, 7.0, 7.5, and 8.0) and centrifuging them in Amicon Ultra cellulose membrane centrifugal filters of 100 kDa at 9600*g* for 75 s. This procedure was repeated five times, obtaining a final volume of about 100 μL.

Native Polyacrylamide Gel Electrophoresis (Native-PAGE). A discontinuous Tris-glycine polyacrylamide gel system consisting of 4% stacking and 8% separation gel was used to check the purity and integrity of soluble oligomeric particles at different pH values. Based on the isoelectric point of OligoBinder-1 and OligoBinder-3 (~5.1 and 5.3, respectively), the most suitable buffer system was Tris-HCl, with a

https://doi.org/10.1021/acsami.2c18305
ACS Appl. Mater. Interfaces 2023, 15, 11444−11457

separating gel of 0.375 M Tris-HCl (pH = 8.8) and a stacking gel of 0.375 mM Tris-HCl (pH = 6.8). The native gels were run in a Mini-PROTEAN electrophoresis chamber (BioRad) in running buffer (25 mM Tris, 192 mM glycine, pH ∼8.8).

Dynamic Light Scattering. The size and molecular weight of oligomers were estimated using a Malvern Zetasizer Nano S90 ZEN1690 instrument. 100 μL of the oligomeric samples were prepared in 20 mM sodium phosphate buffer at different pH values (6.5, 7.0, 7.5, and 8.0) at 25 °C. The measurement for each sample corresponded to 30 averaged acquisitions repeated 3 times. The estimated molecular weight for OligoBinder-1 and OligoBinder-3 was calculated from the mass distribution results using an empirical mass vs globular protein calibration curve, provided by Malvern.

Amyloid Dye Binding. The fluorescence signal of the thioflavin-T (Th-T) and absorbance changes of the Congo red (CR) dyes were measured to determine the formation of amyloid assemblies. For the Th-T binding assay, aggregated and soluble proteins at a final concentration of 20 μM were mixed with 25 μM Th-T. Samples were excited at 445 nm, and emission fluorescence was recorded between 460 and 600 nm with an emission bandwidth of 5 nm using a Jasco FP-8200 spectrofluorometer (Jasco Corporation).

To evaluate the CR spectral shift, aggregated and soluble proteins at a final concentration of 20 μM were incubated with 20 μM CR. Absorbance spectra were recorded at the range from 375 to 700 nm in a SPECORD 200 Plus spectrophotometer (Analytik Jena, Jena, Germany). Spectra of proteins alone were acquired to subtract their contribution to the CR signal. Buffers without protein were used as the baseline signal for Th-T and CR.

Transmission Electron Microscopy. To obtain transmission electron microscopy images, 10 μL of aggregated samples in the presence of 20 mM sodium phosphate buffer with different pH values (6.5, 7.0, 7.5, and 8.0) was deposited into carbon-coated copper grids for 10 min. Grids were negatively stained with 10 μL of 2% (w/v) uranyl acetate solution and wiped out after 1 min with filter paper strips. Resulting grids were visualized using a JEOL 1400 (JEOL Ltd.) TEM instrument at 120 kV, and images were acquired with a CCD GATAN ES1000W Erlangshen camera (Gatan Inc.). Size measurements were performed using ImageJ software (U.S. National Institutes of Health, Bethesda, MD), averaging 10 individual measurements for each oligomeric nanoparticle in 20 mM sodium phosphate buffer pH 8.

Fourier Transform Infrared Spectroscopy. To obtain the IR spectra, 10 μL of purified OligoBinder-1 and OligoBinder-3 was loaded on the diamond crystal of a Bruker Tensor 27 FTIR spectrometer (Bruker Optics) supplied with a Specac MKII Golden Gate ATR accessory, and solvent was evaporated in a stream of nitrogen. FTIR spectra were recorded between 1700 and 1600 cm^{-1} in 32 scans at a resolution of 1 cm^{-1}. Spectra were corrected for the background absorption and normalized with the Min/Max normalization method using OPUS MIR Tensor 27 software (Bruker Optics). IR spectra were fitted employing a nonlinear peak-fitting equation using PeakFit package v4.12 (Systat Software, San Jose, CA). The area for each Gaussian curve was calculated in the amide I region from 1700 to 1600 cm^{-1} using the "AutoFit Peaks I Residuals" option, manually as the starting condition as many peaks as minima were identified in the second derivative. The resulting area, amplitude, and center values of the fitted bands were exported as a table and plotted.

Functional Assessment of OligoBinders. The capacity of OligoBinders to bind SARS-CoV-2-S-RBD protein was explored by a dot blot assay. For this purpose, 10 μL of purified oligomeric particles of 0.40, 0.20, 0.10, and 0.04 μg were spotted onto methanol activated polyvinylidene difluoride membranes (PVDF) (Immobilon-P transfer membranes, Merck Millipore). Sup35-DHFR-Z oligomers at the same concentration range were used as a negative control. A positive control was performed by using rabbit anti-SARS-CoV-2 spike S1 subunit primary antibody (Sino Biological, 40150-T62) at 1, 0.8, 0.4, and 0.2 μg.

The membrane was blocked with 5% BSA/TBST (20 mM Tris-HCl, pH 7.4, and 150 mM NaCl, 1% Tween-20) buffer for 30 min at RT. Next, the membrane was incubated with YFP-S-RBD protein (0.54 ng/μL) dissolved in 0.1% BSA/TBST buffer for 30 min at RT. The membrane was washed with TBST buffer (3 × 5 min), and YFP fluorescence intensity was visualized using a ChemiDoc imaging system (Bio-Rad) and quantified with ImageJ software (U.S. National Institutes of Health, Bethesda, MD). The mean and SD of fluorescence intensity were calculated from three independent membrane blots, and values were plotted with GraphPad Prism software V6.01. For group-wise comparisons, the two-sample (independent groups) t test was performed using IBM SPSS software, version 23.0 (SPSS Inc., Chicago, IL).

The ability of OligoBinders to disrupt the spike RBD−ACE2r interaction was assessed with the Lumit SARS-CoV-2 spike RBD:hACE2r immunoassay (Promega), which is a combination of immunodetection and NanoLuc binary technology (NanoBiT). According to the manufacturer's instructions, 10× oligomeric particles were diluted in 1× immunoassay reaction buffer at a ratio of 10:1 and incubated with 1.5 nM SARS-CoV-2 RBD (Rabbit Fc) for 30 min at RT prior to the addition of 1.5 nM hACE2r-Fc (Mouse Fc) and Lumit antibody mix. After 1 h of incubation at RT, 12.5 μL of Lumit detection reagent was added, followed by incubation at RT for 30 min. Luminescence was recorded using a Spark Tecan fluorescence multimode microplate reader. Lumit reagent buffers with RBD/ACE2r were used as positive control signal, and only buffer was used as negative controls to subtract the background signal contribution. Then, signal fold changes were calculated by dividing sample luminescence by positive control values and converted to % neutralization by subtracting from 100. Concentrations in the range 0.2−40000 pM were $\log_{10}$ transformed and final values represented by the mean of two independent experiments. IC_{50} values were calculated using a nonlinear regression (least-squares) fitting method using GraphPad Prism V6.01 (GraphPad Software, Inc.).

Virus Neutralization. To examine the capacity of OligoBinders to prevent the infection of cells by SARS-CoV-2, we employed a cell-based screening assay using HiBiT-tagged PsVLP from Promega Biotech. The genome-free nature of SC2-VLPs eliminates the need for biosafety level 3 (BSL3) facilities during handling. HiBiT technology provides the benefits of high sensitivity and convenience of a single-reagent-addition step, all while overcoming the disadvantage of difficulty quantifying PsVLP cell entry and membrane fusion.

Serial dilutions of OligoBinder-1 and OligoBinder-3 were prepared in the range 0.2−40000 pM. Next, 4× OligoBinder-1 and OligoBinder-3 were incubated with SARS-CoV-2 S(G614) HiBiT-SC2-VLPs dissolved in assay buffer for 30 min at 37 °C. Next, SARS-CoV-2 HEK293T (LgBiT) target cells were thawed and transferred to a 96-well plate containing HiBiT-SC2-VLPs and OligoBinders. After 3 h of incubation at 37 °C, 25 μL of 5× Nano-Glo live cell reagent was added to each well, and luminescence was measured after 15 min of incubation at 37 °C. In the presence of inhibitory particles, SC2-VLP entry and fusion with target cells were blocked; therefore, this prevented HiBiT release, and no luminescent signal was produced. Assay buffer was used to calculate the baseline signal. Next, maximum entry values of SC2-VLPs into cells were calculated by dividing baseline-corrected values by values from control samples containing no oligomeric particle. The obtained luminescence values were normalized to neutralization%, where the highest luminescence value was defined as 0%, and the lowest luminescence values were defined as 100%. GraphPad Prism V6.01 (GraphPad Software, Inc.) was used to fit the obtained values to a nonlinear regression curve (least-squares fitting method) to determine the IC_{50}.

Cytotoxicity Assay. HeLa and MRC-5 cell lines were acquired from American Type Culture Collection (ATCC). Cells were maintained in DMEM medium supplemented with 10% fetal bovine serum at 37 °C in a 5% CO_2 atmosphere. HeLa cells were seeded onto a 96-well plate at a density of 3500 cells/well, and MRC-5 cells were seeded at 2000 cells/well with 100 μL of culture medium. After 24 h, cells were incubated with OligoBinder-1 and OligoBinder-3 particles in the range 1−10 μM in triplicate. The control group received the same volume of sterile PBS as vehicle. After 72 h of incubation, 10 μL of Prestoblue cell viability reagent (Invitrogen) was added for 30 min. The fluorescence emission was recorded at 615 nm, with an excitation

https://doi.org/10.1021/acsami.2c18305
ACS Appl. Mater. Interfaces 2023, 15, 11444−11457

wavelength of 531 nm using a Victor III multilabel plate reader (PerkinElmer).

Stability of OligoBinders in Plasma. OligoBinder nanoparticles were dissolved in 100 μL of plasma at a final concentration of 16 μM into each of four 0.5 mL low protein binding microtubes and incubated at 25 °C. Aliquots at 0, 24, and 48 h were removed, and 4× loading buffer was added into each sample and immediately stored frozen at −20 °C until analyzed. Plasma without oligomeric particles was used as a control.

To analyze samples, 7 μL of each sample was mixed with 5 μL of Milli Q water and incubated at 90 °C for 5 min, and 12 μL (9.3 μM) of the incubated samples was loaded onto a 15% SDS-PAGE gel. The protein was electrophoretically transferred to a methanol activated PVDF membrane (Immobilon-P transfer membranes, Merck Millipore) in a trans-blot cell (Bio-Rad) with transfer buffer 1× (0.05 M Tris-HCl, 0.04 M glycine, 0.04% SDS, 20% methanol) at 100 V for 1 h. The membrane was then blocked for 1 h with 1X TBST buffer containing 10% nonfat dried milk. After blocking, the membrane was incubated with 1:2000 anti-His tag mouse monoclonal antibody (Invitrogen, MA1-21315) overnight at 4 °C. The membrane was then washed with TBST 1× (3 × 10 min) and incubated with 1:10000 anti-mouse IgG conjugated to horseradish peroxidase (Bio-RAD, 170-6516) for 1 h. The membrane was revealed with Immobilon Forte Western HRP substrate (Millipore Corporation) for 5 min. Images were captured using a ChemiDoc imaging system−Bio-Rad with an exposure time of 500 s.

Analytical Size Exclusion Chromatography (SEC). OligoBinder nanoparticles were incubated in the presence of human plasma at a final concentration of 16 μM for 24 h at room temperature. Next, 100 μL of OligoBinder-1 and OligoBinder-3 incubated in human plasma was injected separately into a Superdex 200 10/300 GL column using 20 mM sodium phosphate buffer, pH 8.0, at room temperature. In addition, the elution profiles of human plasma alone, Oligobinder-1 and OligoBinder-3, and Sup35-DHFR-LCB1 and Sup35-DHFR-LCB3 in sodium phosphate buffer were analyzed.

For size reference, an elution pattern was performed using different proteins as calibrators (carbonic anhydrase 29 kDa, β-amylase 200 kDa, ferritin 440 kDa, thyroglobuline 669 kDa) in a Superdex 200 10/300 GL column (GE Healthcare), using a flow rate of 0.5 mL/min in 20 mM sodium phosphate buffer, pH 8.0.

Immunoblotting Analysis of SEC Samples. The elution fractions corresponding to monomeric and oligomeric forms were further detected by SDS-PAGE immunoblotting. For this purpose, collected SEC fractions were concentrated 100× for monomeric forms using 10,000 MWCO cellulose membrane centrifugal filters (Millipore) and 30× for oligomeric forms using 100,000 MWCO centrifugal filters (Millipore). 4× loading buffer was added into each sample, and 16 μL sample fractions were loaded on 15% SDS-PAGE and blotted onto a PVDF membrane. Soluble monomeric Sup35-DHFR-LCB1, Sup35-DHFR-LCB3, OligoBinder-1, and OligoBinder-3 in sodium phosphate buffer were used as positive controls, and plasma without added OligoBinders was used as negative control. The antibodies employed were 1:1000 primary 6x-His Tag monoclonal antibody (Invitrogen, MA1-21315) and 1:10000 secondary anti-mouse IgG-HRP conjugate (Bio-RAD, 170-6516). The membranes were developed with Immobilon Forte Western HRP substrate (Millipore), and images were captured using a ChemiDoc imaging system−Bio-Rad with an exposure time of 500 s.

■ ASSOCIATED CONTENT

Supporting Information

The Supporting Information is available free of charge at https://pubs.acs.org/doi/10.1021/acsami.2c18305.

Expression and purification of soluble and oligomeric Sup35-DHFR-LCB1 fusion protein and Sup35-DHFR-LCB3 fusion protein; characterization of size distribution of OligoBinder-1 and OligoBinder-3 at different pHs at time 0 and after 24 h of incubation; TEM images; schematic representation and biophysical characterization of oligomeric Sup35-DHFR-Z fusion protein; stability of OligoBinders in plasma; and characterization of OligoBinders' size and stability in plasma (PDF)

■ AUTHOR INFORMATION

Corresponding Authors

Susanna Navarro − *Institut de Biotecnologia i de Biomedicina (IBB) and Departament de Bioquímica i Biologia Molecular, Universitat Autònoma de Barcelona, 08193 Barcelona, Spain;* orcid.org/0000-0001-8160-9536; Email: Susanna.Navarro.Cantero@uab.cat

Salvador Ventura − *Institut de Biotecnologia i de Biomedicina (IBB) and Departament de Bioquímica i Biologia Molecular, Universitat Autònoma de Barcelona, 08193 Barcelona, Spain;* orcid.org/0000-0002-9652-6351; Email: salvador.ventura@uab.cat

Authors

Molood Behbahanipour − *Institut de Biotecnologia i de Biomedicina (IBB) and Departament de Bioquímica i Biologia Molecular, Universitat Autònoma de Barcelona, 08193 Barcelona, Spain*

Roger Benoit − *Laboratory of Nanoscale Biology, Division of Biology and Chemistry, Paul Scherrer Institute, 5232 Villigen PSI, Switzerland;* orcid.org/0000-0001-9420-7739

Complete contact information is available at: https://pubs.acs.org/10.1021/acsami.2c18305

Author Contributions

S.V. conceived the project. S.N. and S.V. designed the experiments. M.B. and S.N. performed the experiments. M.B. and S.N. analyzed the data. R.B. produced YFP-S-RBD. M.B., S.N., and S.V. wrote the manuscript. All authors have given approval to the final version of the manuscript.

Notes

The authors declare no competing financial interest.

■ ACKNOWLEDGMENTS

This work was funded by the Spanish Ministry of Science and Innovation (PID2019-105017RB-I00) and by ICREA, ICREA-Academia 2020, to S.V. M.B. was supported by the Spanish Ministry of Science and Innovation (PRE2020-092634). We thank Promega Biotech Ibérica SL for providing us with the NanoBiT technology.

■ ABBREVIATIONS

SARS-CoV-2, severe acute respiratory syndrome coronavirus 2
COVID-19, coronavirus disease 2019
RBD, receptor binding domain
ACE2r, angiotensin-converting enzyme 2 receptor
mAb, monoclonal antibody
SAC, soft amyloid core
DHFR, dihydrofolate reductase
IC_{50}, half-maximal inhibitory concentration
CD, circular dichroism
Trp, tryptophan
Th-T, thioflavin-T
CR, congo red
FTIR, Fourier-transform infrared
TEM, transmission electron microscopy
DLS, dynamic light scattering

SC2-VLPs, SARS-CoV-2 virus-like particles
SD, standard deviation
BSL3, biosafety level 3
PBS, phosphate buffered saline
PVDF, polyvinylidene difluoride membranes
RT, room temperature

REFERENCES

(1) Santomauro, D. F.; Herrera, A. M. M.; Shadid, J.; Zheng, P.; Ashbaugh, C.; Pigott, D. M.; Abbafati, C.; Adolph, C.; Amlag, J. O.; Aravkin, A. Y. Global Prevalence and Burden of Depressive and Anxiety Disorders in 204 Countries and Territories in 2020 Due to the Covid-19 Pandemic. *Lancet* **2021**, *398*, 1700−1712.

(2) Hu, Y.; Yang, H.; Hou, C.; Chen, W.; Zhang, H.; Ying, Z.; Hu, Y.; Sun, Y.; Qu, Y.; Feychting, M. Covid-19 Related Outcomes among Individuals with Neurodegenerative Diseases: A Cohort Analysis in the Uk Biobank. *BMC neurology* **2022**, *22*, 1−12.

(3) Naaber, P.; Tserel, L.; Kangro, K.; Sepp, E.; Jürjenson, V.; Adamson, A.; Haljasmägi, L.; Rumm, A. P.; Maruste, R.; Kärner, J. Dynamics of Antibody Response to Bnt162b2 Vaccine after Six Months: A Longitudinal Prospective Study. *Lancet Regional Health-Europe* **2021**, *10*, 100208.

(4) Letko, M.; Marzi, A.; Munster, V. Functional Assessment of Cell Entry and Receptor Usage for Sars-Cov-2 and Other Lineage B Betacoronaviruses. *Nature microbiology* **2020**, *5*, 562−569.

(5) Hoffmann, M.; Kleine-Weber, H.; Schroeder, S.; Krüger, N.; Herrler, T.; Erichsen, S.; Schiergens, T. S.; Herrler, G.; Wu, N.-H.; Nitsche, A. Sars-Cov-2 Cell Entry Depends on Ace2 and Tmprss2 and Is Blocked by a Clinically Proven Protease Inhibitor. *cell* **2020**, *181*, 271−280.

(6) Jackson, C. B.; Farzan, M.; Chen, B.; Choe, H. Mechanisms of Sars-Cov-2 Entry into Cells. *Nat. Rev. Mol. Cell Biol.* **2022**, *23*, 3−20.

(7) Liu, F.; Long, X.; Zhang, B.; Zhang, W.; Chen, X.; Zhang, Z. Ace2 Expression in Pancreas May Cause Pancreatic Damage after Sars-Cov-2 Infection. *Clinical Gastroenterology and Hepatology* **2020**, *18*, 2128−2130.

(8) Nepali, K.; Sharma, R.; Sharma, S.; Thakur, A.; Liou, J. P. Beyond the Vaccines: A Glance at the Small Molecule and Peptide-Based Anti-Covid19 Arsenal. *J. Biomed Sci.* **2022**, *29*, 65.

(9) Lin, Y.-C.; Chen, W.-Y.; Hwu, E.-T.; Hu, W.-P. In-Silico Selection of Aptamer Targeting Sars-Cov-2 Spike Protein. *International Journal of Molecular Sciences* **2022**, *23*, 5810.

(10) Wu, Y.; Wang, F.; Shen, C.; Peng, W.; Li, D.; Zhao, C.; Li, Z.; Li, S.; Bi, Y.; Yang, Y.; Gong, Y.; Xiao, H.; Fan, Z.; Tan, S.; Wu, G.; Tan, W.; Lu, X.; Fan, C.; Wang, Q.; Liu, Y.; Zhang, C.; Qi, J.; Gao, G. F.; Gao, F.; Liu, L. A Noncompeting Pair of Human Neutralizing Antibodies Block Covid-19 Virus Binding to Its Receptor Ace2. *Science* **2020**, *368*, 1274−1278.

(11) Chi, X.; Yan, R.; Zhang, J.; Zhang, G.; Zhang, Y.; Hao, M.; Zhang, Z.; Fan, P.; Dong, Y.; Yang, Y.; Chen, Z.; Guo, Y.; Zhang, J.; Li, Y.; Song, X.; Chen, Y.; Xia, L.; Fu, L.; Hou, L.; Xu, J.; Yu, C.; Li, J.; Zhou, Q.; Chen, W. A Neutralizing Human Antibody Binds to the N-Terminal Domain of the Spike Protein of Sars-Cov-2. *Science* **2020**, *369*, 650−655.

(12) Liu, L.; Wang, P.; Nair, M. S.; Yu, J.; Rapp, M.; Wang, Q.; Luo, Y.; Chan, J. F.; Sahi, V.; Figueroa, A.; Guo, X. V.; Cerutti, G.; Bimela, J.; Gorman, J.; Zhou, T.; Chen, Z.; Yuen, K. Y.; Kwong, P. D.; Sodroski, J. G.; Yin, M. T.; Sheng, Z.; Huang, Y.; Shapiro, L.; Ho, D. D. Potent Neutralizing Antibodies against Multiple Epitopes on Sars-Cov-2 Spike. *Nature* **2020**, *584*, 450−456.

(13) Shi, R.; Shan, C.; Duan, X.; Chen, Z.; Liu, P.; Song, J.; Song, T.; Bi, X.; Han, C.; Wu, L.; Gao, G.; Hu, X.; Zhang, Y.; Tong, Z.; Huang, W.; Liu, W. J.; Wu, G.; Zhang, B.; Wang, L.; Qi, J.; Feng, H.; Wang, F. S.; Wang, Q.; Gao, G. F.; Yuan, Z.; Yan, J. A Human Neutralizing Antibody Targets the Receptor-Binding Site of Sars-Cov-2. *Nature* **2020**, *584*, 120−124.

(14) Koussoroplis, S. J.; Paulissen, G.; Tyteca, D.; Goldansaz, H.; Todoroff, J.; Barilly, C.; Uyttenhove, C.; Van Snick, J.; Cataldo, D.; Vanbever, R. Pegylation of Antibody Fragments Greatly Increases Their Local Residence Time Following Delivery to the Respiratory Tract. *J. Controlled Release* **2014**, *187*, 91−100.

(15) Guillon, A.; Pardessus, J.; Lhommet, P.; Parent, C.; Respaud, R.; Marchand, D.; Montharu, J.; De Monte, M.; Janiak, P.; Boixel, C.; Audat, H.; Huille, S.; Guillot, E.; Heuze-Vourc'h, N. Exploring the Fate of Inhaled Monoclonal Antibody in the Lung Parenchyma by Microdialysis. *MAbs* **2019**, *11*, 297−304.

(16) Cao, L.; Goreshnik, I.; Coventry, B.; Case, J. B.; Miller, L.; Kozodoy, L.; Chen, R. E.; Carter, L.; Walls, A. C.; Park, Y. J.; Strauch, E. M.; Stewart, L.; Diamond, M. S.; Veesler, D.; Baker, D. De Novo Design of Picomolar Sars-Cov-2 miniprotein Inhibitors. *Science* **2020**, *370*, 426−431.

(17) Medhi, R.; Srinoi, P.; Ngo, N.; Tran, H. V.; Lee, T. R. Nanoparticle-Based Strategies to Combat Covid-19. *Acs Appl. Nano Mater.* **2020**, *3*, 8557−8580.

(18) Weiss, C.; Carriere, M.; Fusco, L.; Capua, I.; Regla-Nava, J. A.; Pasquali, M.; Scott, J. A.; Vitale, F.; Unal, M. A.; Mattevi, C.; Bedognetti, D.; Merkoçi, A.; Tasciotti, E.; Yilmazer, A.; Gogotsi, Y.; Stellacci, F.; Delogu, L. G. Toward Nanotechnology-Enabled Approaches against the Covid-19 Pandemic. *ACS Nano* **2020**, *14*, 6383−6406.

(19) Cai, X.; Chen, M.; Prominski, A.; Lin, Y.; Ankenbruck, N.; Rosenberg, J.; Nguyen, M.; Shi, J.; Tomatsidou, A.; Randall, G.; Missiakas, D.; Fung, J.; Chang, E. B.; Penaloza-MacMaster, P.; Tian, B.; Huang, J. A Multifunctional Neutralizing Antibody-Conjugated Nanoparticle Inhibits and Inactivates Sars-Cov-2. *Adv. Sci. (Weinh)* **2022**, *9*, No. e2103240.

(20) Riek, R.; Eisenberg, D. S. The Activities of Amyloids from a Structural Perspective. *Nature* **2016**, *539*, 227−235.

(21) Das, S.; Jacob, R. S.; Patel, K.; Singh, N.; Maji, S. K. Amyloid Fibrils: Versatile Biomaterials for Cell Adhesion and Tissue Engineering Applications. *Biomacromolecules* **2018**, *19*, 1826−1839.

(22) Diaz-Caballero, M.; Navarro, S.; Fuentes, I.; Teixidor, F.; Ventura, S. Minimalist Prion-Inspired Polar Self-Assembling Peptides. *ACS Nano* **2018**, *12*, 5394−5407.

(23) Diaz-Caballero, M.; Navarro, S.; Ventura, S. Functionalized Prion-Inspired Amyloids for Biosensor Applications. *Biomacromolecules* **2021**, *22*, 2822−2833.

(24) Wang, W.; Gil-Garcia, M.; Ventura, S. Dual Antibody-Conjugated Amyloid Nanorods to Promote Selective Cell-Cell Interactions. *ACS Appl. Mater. Interfaces* **2021**, *13*, 14875−14884.

(25) Wang, W.; Navarro, S.; Azizyan, R. A.; Bano-Polo, M.; Esperante, S. A.; Kajava, A. V.; Ventura, S. Prion Soft Amyloid Core Driven Self-Assembly of Globular Proteins into Bioactive Nanofibrils. *Nanoscale* **2019**, *11*, 12680−12694.

(26) Knowles, T. P.; Mezzenga, R. Amyloid Fibrils as Building Blocks for Natural and Artificial Functional Materials. *Adv. Mater.* **2016**, *28*, 6546−61.

(27) Wang, W.; Azizyan, R. A.; Garro, A.; Kajava, A. V.; Ventura, S. Multifunctional Amyloid Oligomeric Nanoparticles for Specific Cell Targeting and Drug Delivery. *Biomacromolecules* **2020**, *21*, 4302−4312.

(28) Sant'Anna, R.; Fernandez, M. R.; Batlle, C.; Navarro, S.; de Groot, N. S.; Serpell, L.; Ventura, S. Characterization of Amyloid Cores in Prion Domains. *Sci. Rep* **2016**, *6*, 34274.

(29) Batlle, C.; de Groot, N. S.; Iglesias, V.; Navarro, S.; Ventura, S. Characterization of Soft Amyloid Cores in Human Prion-Like Proteins. *Sci. Rep* **2017**, *7*, 12134.

(30) Schnell, J. R.; Dyson, H. J.; Wright, P. E. Structure, Dynamics, and Catalytic Function of Dihydrofolate Reductase. *Annual review of biophysics and biomolecular structure* **2004**, *33*, 119−140.

(31) Han, Y.; Yang, Z.; Hu, H.; Zhang, H.; Chen, L.; Li, K.; Kong, L.; Wang, Q.; Liu, B.; Wang, M.; Lin, J.; Chen, P. R. Covalently Engineered Protein Minibinders with Enhanced Neutralization Efficacy against Escaping Sars-Cov-2 Variants. *J. Am. Chem. Soc.* **2022**, *144*, 5702−5707.

(32) Sabate, R.; Ventura, S. Cross-Beta-Sheet Supersecondary Structure in Amyloid Folds: Techniques for Detection and Characterization. *Methods Mol. Biol.* **2013**, *932*, 237−57.

https://doi.org/10.1021/acsami.2c18305
ACS Appl. Mater. Interfaces 2023, 15, 11444−11457

(33) Navarro, S.; Ventura, S. Computational Methods to Predict Protein Aggregation. *Curr. Opin Struct Biol.* **2022**, *73*, 102343.
(34) Invernizzi, G.; Papaleo, E.; Sabate, R.; Ventura, S. Protein Aggregation: Mechanisms and Functional Consequences. *Int. J. Biochem. Cell Biol.* **2012**, *44*, 1541−54.
(35) Buell, A. K. Stability Matters, Too - the Thermodynamics of Amyloid Fibril Formation. *Chem. Sci.* **2022**, *13*, 10177−10192.
(36) Chen, S. W.; Drakulic, S.; Deas, E.; Ouberai, M.; Aprile, F. A.; Arranz, R.; Ness, S.; Roodveldt, C.; Guilliams, T.; De-Genst, E. J.; Klenerman, D.; Wood, N. W.; Knowles, T. P.; Alfonso, C.; Rivas, G.; Abramov, A. Y.; Valpuesta, J. M.; Dobson, C. M.; Cremades, N. Structural Characterization of Toxic Oligomers That Are Kinetically Trapped During Alpha-Synuclein Fibril Formation. *Proc. Natl. Acad. Sci. U. S. A.* **2015**, *112*, No. e1994-2003.
(37) Santos, J.; Gracia, P.; Navarro, S.; Pena-Diaz, S.; Pujols, J.; Cremades, N.; Pallares, I.; Ventura, S. Alpha-Helical Peptidic Scaffolds to Target Alpha-Synuclein Toxic Species with Nanomolar Affinity. *Nat. Commun.* **2021**, *12*, 3752.
(38) Wasmer, C.; Schutz, A.; Loquet, A.; Buhtz, C.; Greenwald, J.; Riek, R.; Bockmann, A.; Meier, B. H. The Molecular Organization of the Fungal Prion Het-S in Its Amyloid Form. *J. Mol. Biol.* **2009**, *394*, 119−27.
(39) Azizyan, R. A.; Garro, A.; Radkova, Z.; Anikeenko, A.; Bakulina, A.; Dumas, C.; Kajava, A. V. Establishment of Constraints on Amyloid Formation Imposed by Steric Exclusion of Globular Domains. *J. Mol. Biol.* **2018**, *430*, 3835−3846.
(40) Azizyan, R. A.; Wang, W.; Anikeenko, A.; Radkova, Z.; Bakulina, A.; Garro, A.; Charlier, L.; Dumas, C.; Ventura, S.; Kajava, A. V. Amyloidogenicity as a Driving Force for the Formation of Functional Oligomers. *J. Struct Biol.* **2020**, *212*, 107604.
(41) Bierig, T.; Collu, G.; Blanc, A.; Poghosyan, E.; Benoit, R. M. Design, Expression, Purification, and Characterization of a Yfp-Tagged 2019-Ncov Spike Receptor-Binding Domain Construct. *Frontiers in Bioengineering and Biotechnology* **2020**, *8*, 1442.
(42) Tashiro, M.; Tejero, R.; Zimmerman, D. E.; Celda, B.; Nilsson, B.; Montelione, G. T. High-Resolution Solution Nmr Structure of the Z Domain of Staphylococcal Protein A. *J. Mol. Biol.* **1997**, *272*, 573−90.
(43) Alves, J.; Engel, L.; de Vasconcelos Cabral, R.; Rodrigues, E. L.; de Jesus Ribeiro, L.; Higa, L. M.; da Costa Ferreira Júnior, O.; Castiñeiras, T. M. P.; de Carvalho Leitão, I.; Tanuri, A. A Bioluminescent and Homogeneous Sars-Cov-2 Spike Rbd and Hace2 Interaction Assay for Antiviral Screening and Monitoring Patient Neutralizing Antibody Levels. *Sci. Rep.* **2021**, *11*, 1−15.
(44) Marcink, T. C.; Kicmal, T.; Armbruster, E.; Zhang, Z.; Zipursky, G.; Golub, K. L.; Idris, M.; Khao, J.; Drew-Bear, J.; McGill, G.; Gallagher, T.; Porotto, M.; des Georges, A.; Moscona, A. Intermediates in Sars-Cov-2 Spike-Mediated Cell Entry. *Sci. Adv.* **2022**, *8*, No. eabo3153.
(45) Qing, E.; Kicmal, T.; Kumar, B.; Hawkins, G. M.; Timm, E.; Perlman, S.; Gallagher, T. Dynamics of Sars-Cov-2 Spike Proteins in Cell Entry: Control Elements in the Amino-Terminal Domains. *mBio* **2021**, *12*, No. e0159021.
(46) Qing, E.; Li, P.; Cooper, L.; Schulz, S.; Jack, H. M.; Rong, L.; Perlman, S.; Gallagher, T. Inter-Domain Communication in Sars-Cov-2 Spike Proteins Controls Protease-Triggered Cell Entry. *Cell Rep* **2022**, *39*, 110786.
(47) Miyakawa, K.; Jeremiah, S. S.; Ohtake, N.; Matsunaga, S.; Yamaoka, Y.; Nishi, M.; Morita, T.; Saji, R.; Nishii, M.; Kimura, H.; Hasegawa, H.; Takeuchi, I.; Ryo, A. Rapid Quantitative Screening Assay for Sars-Cov-2 Neutralizing Antibodies Using Hibit-Tagged Virus-Like Particles. *J. Mol. Cell Biol.* **2021**, *12*, 987−990.
(48) Zuo, L.; Ao, G.; Wang, Y.; Gao, M.; Qi, X. Bamlanivimab Improves Hospitalization and Mortality Rates in Patients with Covid-19: A Systematic Review and Meta-Analysis. *J. Infect* **2022**, *84*, 248−288.
(49) Recovery Collaborative Group. Casirivimab and Imdevimab in Patients Admitted to Hospital with Covid-19 (Recovery): A Randomised, Controlled, Open-Label, Platform Trial. *Lancet* **2022**, *399*, 665−676.
(50) Gottlieb, R. L.; Nirula, A.; Chen, P.; Boscia, J.; Heller, B.; Morris, J.; Huhn, G.; Cardona, J.; Mocherla, B.; Stosor, V.; Shawa, I.; Kumar, P.; Adams, A. C.; Van Naarden, J.; Custer, K. L.; Durante, M.; Oakley, G.; Schade, A. E.; Holzer, T. R.; Ebert, P. J.; Higgs, R. E.; Kallewaard, N. L.; Sabo, J.; Patel, D. R.; Klekotka, P.; Shen, L.; Skovronsky, D. M. Effect of Bamlanivimab as Monotherapy or in Combination with Etesevimab on Viral Load in Patients with Mild to Moderate Covid-19: A Randomized Clinical Trial. *JAMA* **2021**, *325*, 632−644.
(51) Falcone, M.; Tiseo, G.; Valoriani, B.; Barbieri, C.; Occhineri, S.; Mazzetti, P.; Vatteroni, M. L.; Suardi, L. R.; Riccardi, N.; Pistello, M.; Tacconi, D.; Menichetti, F. Efficacy of Bamlanivimab/Etesevimab and Casirivimab/Imdevimab in Preventing Progression to Severe Covid-19 and Role of Variants of Concern. *Infect Dis Ther* **2021**, *10*, 2479−2488.
(52) Díaz-Caballero, M.; Navarro, S.; Ventura, S. Soluble Assemblies in the Fibrillation Pathway of Prion-Inspired Artificial Functional Amyloids Are Highly Cytotoxic. *Biomacromolecules* **2020**, *21*, 2334−2345.
(53) Owen, D. R.; Allerton, C. M.; Anderson, A. S.; Aschenbrenner, L.; Avery, M.; Berritt, S.; Boras, B.; Cardin, R. D.; Carlo, A.; Coffman, K. J. An Oral Sars-Cov-2 Mpro Inhibitor Clinical Candidate for the Treatment of Covid-19. *Science* **2021**, *374*, 1586−1593.
(54) Ansems, K.; Grundeis, F.; Dahms, K.; Mikolajewska, A.; Thieme, V.; Piechotta, V.; Metzendorf, M.-I.; Stegemann, M.; Benstoem, C.; Fichtner, F. Remdesivir for the Treatment of Covid-19. *Cochrane Database of Systematic Reviews* **2021**, *8*, CD014962.
(55) Whitley, R. Molnupiravir - a Step toward Orally Bioavailable Therapies for Covid-19. *N Engl J. Med.* **2022**, *386*, 592−593.
(56) Schütz, D.; Ruiz-Blanco, Y. B.; Münch, J.; Kirchhoff, F.; Sanchez-Garcia, E.; Müller, J. A. Peptide and Peptide-Based Inhibitors of Sars-Cov-2 Entry. *Advanced drug delivery reviews* **2020**, *167*, 47−65.
(57) Das, G.; Ghosh, S.; Garg, S.; Ghosh, S.; Jana, A.; Samat, R.; Mukherjee, N.; Roy, R.; Ghosh, S. An Overview of Key Potential Therapeutic Strategies for Combat in the Covid-19 Battle. *RSC Adv.* **2020**, *10*, 28243−28266.

https://doi.org/10.1021/acsami.2c18305
ACS Appl. Mater. Interfaces 2023, 15, 11444−11457

Concluding remarks

Chapter 1: Bioengineered self-assembled nanofibrils for high-affinity SARS-CoV-2 capture and neutralization

- Bioengineered amyloid-like nanofibrils were successfully designed to specifically capture and neutralize SARS-CoV-2. This was achieved through a modular, generalizable method leveraging the self-assembling properties of the SAC peptide derived from the Sup35 yeast prion domain.
- The nanofibrils demonstrated strong binding affinity to the receptor-binding domain (RBD) of the virus, ensuring effective neutralization while minimizing non-specific interactions.
- Stable nanofibrils can be embedded onto surfaces, such as polyvinylidene difluoride (PVDF), effectively trapped SARS-CoV-2' RBD proteins, creating functional antiviral layers that may serve as an effective layer of protection in public and medical environments susceptible to viral spread, reducing the risk of surface-based transmission. Offering a promising approach for antiviral coatings, with the potential to reduce viral spread in high-contact areas.
- Mesoscopic structure and activity of nanofibrils are easily modulated, by varying salt concentrations, allowing optimization of their structural characteristics and virus-binding efficiency.
- Molecular modeling of the Sup35-LCB1 nanofibrils revealed a stable cross-β arrangement of the SAC amyloid core, formed through stacking of linear β-strands or β-arches. The protruding LCB1 domains ensured accessible binding sites for the virus without significant steric hindrance.
- The amyloid-like nanofibrils exhibited no cytotoxic effects on human cell lines, supporting their potential application in diagnostic tools, antiviral coatings, or other biomedical uses.

Chapter 2: OligoBinders: Bioengineered Soluble Amyloid-like Nanoparticles to Bind and Neutralize SARS-CoV-2

- Soluble oligomeric amyloid-like spherical nanoparticles were constructed using a modular, generalizable method that uses the self-assembling properties of the SAC

peptide from Sup35-yeast prion domain. These nanoparticles displayed homogeneity in size distribution.

- The nanoparticles demonstrated potent neutralizing capabilities against SARS-CoV-2, effectively preventing the fusion of virus-like particles with ACE2-expressing cell membranes. Their inhibitory concentration (IC50) values were in the picomolar range, comparable to current antibody-based treatments.
- The nanoparticles exhibited high stability in plasma and did not induce cytotoxic effects in human cell lines. These properties underscore their suitability for therapeutic and prophylactic applications, including direct respiratory tract delivery via nasal sprays.

References

Adamcik, J., & Mezzenga, R. (2018). Amyloid polymorphism in the protein folding and aggregation energy landscape. *Angewandte Chemie International Edition*, *57*(28), 8370-8382.

Alberti, S., Halfmann, R., King, O., Kapila, A., & Lindquist, S. (2009). A systematic survey identifies prions and illuminates sequence features of prionogenic proteins. *Cell*, *137*(1), 146-158.

Altamura, L., Horvath, C., Rengaraj, S., Rongier, A., Elouarzaki, K., Gondran, C., Maçon, A. L., Vendrely, C., Bouchiat, V., & Fontecave, M. (2017). A synthetic redox biofilm made from metalloprotein–prion domain chimera nanowires. *Nature chemistry*, *9*(2), 157-163.

An, B., Wang, X., Cui, M., Gui, X., Mao, X., Liu, Y., Li, K., Chu, C., Pu, J., & Ren, S. (2017). Diverse supramolecular nanofiber networks assembled by functional low-complexity domains. *ACS Nano*, *11*(7), 6985-6995.

Anfinsen, C. B. (1973). Principles that govern the folding of protein chains. *Science*, *181*(4096), 223-230.

Anfinsen, C. B., Haber, E., Sela, M., & White Jr, F. (1961). The kinetics of formation of native ribonuclease during oxidation of the reduced polypeptide chain. *Proceedings of the National Academy of Sciences*, *47*(9), 1309-1314.

Annamalai, K., Gührs, K. H., Koehler, R., Schmidt, M., Michel, H., Loos, C., Gaffney, P. M., Sigurdson, C. J., Hegenbart, U., & Schönland, S. (2016). Polymorphism of amyloid fibrils in vivo. *Angewandte Chemie International Edition*, *55*(15), 4822-4825.

Annamalai, K., Liberta, F., Vielberg, M. T., Close, W., Lilie, H., Gührs, K. H., Schierhorn, A., Koehler, R., Schmidt, A., & Haupt, C. (2017). Common fibril structures imply systemically conserved protein misfolding pathways in vivo. *Angewandte Chemie*, *129*(26), 7618-7622.

Bai, Y., Luo, Q., & Liu, J. (2016). Protein self-assembly via supramolecular strategies. *Chemical Society Reviews*, *45*(10), 2756-2767.

Baldwin, A. J., Knowles, T. P., Tartaglia, G. G., Fitzpatrick, A. W., Devlin, G. L., Shammas, S. L., Waudby, C. A., Mossuto, M. F., Meehan, S., & Gras, S. L. (2011). Metastability of native proteins and the phenomenon of amyloid formation. *Journal of the American Chemical Society*, *133*(36), 14160-14163.

Baldwin, R. L., & Rose, G. D. (1999). Is protein folding hierarchic? II. Folding intermediates and transition states. *Trends in biochemical sciences*, *24*(2), 77-83.

Bartolomé-Nafría, A., García-Pardo, J., & Ventura, S. (2024). Mutations in human prion-like domains: pathogenic but not always amyloidogenic. *Prion*, *18*(1), 28-39.

Baskakov, I. V., Legname, G., Prusiner, S. B., & Cohen, F. E. (2001). Folding of prion protein to its native α-helical conformation is under kinetic control. *Journal of Biological Chemistry*, *276*(23), 19687-19690.

Baßler, J., & Hurt, E. (2019). Eukaryotic ribosome assembly. *Annual review of biochemistry*, *88*(1), 281-306.

Batlle, C., Calvo, I., Iglesias, V., J. Lynch, C., Gil-Garcia, M., Serrano, M., & Ventura, S. (2021). MED15 prion-like domain forms a coiled-coil responsible for its amyloid conversion and propagation. *Communications Biology*, *4*(1), 414.

Batlle, C., De Groot, N. S., Iglesias, V., Navarro, S., & Ventura, S. (2017). Characterization of soft amyloid cores in human prion-like proteins. *Scientific reports*, *7*(1), 12134.

Behbahanipour, M., Benoit, R., Navarro, S., & Ventura, S. (2023). OligoBinders: Bioengineered Soluble Amyloid-like Nanoparticles to Bind and Neutralize SARS-CoV-2. *ACS Appl Mater Interfaces*, *15*(9), 11444-11457.

Behbahanipour, M., Garcia-Pardo, J., & Ventura, S. (2021). Decoding the role of coiled-coil motifs in human prion-like proteins. *Prion*, *15*(1), 143-154.

Behbahanipour, M., Navarro, S., Bárcenas, O., Garcia-Pardo, J., & Ventura, S. (2024). Bioengineered self-assembled nanofibrils for high-affinity SARS-CoV-2 capture and neutralization. *Journal of Colloid and Interface Science*, *674*, 753-765.

Bemporad, F., & Chiti, F. (2012). Protein misfolded oligomers: experimental approaches, mechanism of formation, and structure-toxicity relationships. *Chemistry & biology*, *19*(3), 315-327.

Bieler, S., Estrada, L., Lagos, R., Baeza, M., Castilla, J., & Soto, C. (2005). Amyloid formation modulates the biological activity of a bacterial protein. *Journal of Biological Chemistry*, *280*(29), 26880-26885.

Bitran, A., Jacobs, W. M., Zhai, X., & Shakhnovich, E. (2020). Cotranslational folding allows misfolding-prone proteins to circumvent deep kinetic traps. *Proceedings of the National Academy of Sciences*, *117*(3), 1485-1495.

Boeynaems, S., Alberti, S., Fawzi, N. L., Mittag, T., Polymenidou, M., Rousseau, F., Schymkowitz, J., Shorter, J., Wolozin, B., & Van Den Bosch, L. (2018). Protein phase separation: a new phase in cell biology. *Trends in cell biology*, *28*(6), 420-435.

Breydo, L., & Uversky, V. N. (2015). Structural, morphological, and functional diversity of amyloid oligomers. *FEBS letters*, *589*(19), 2640-2648.

Calero, M., & Gasset, M. (2012). Featuring amyloids with Fourier transform infrared and circular dichroism spectroscopies. *Amyloid proteins: Methods and protocols*, 53-68.

Cao, L., Goreshnik, I., Coventry, B., Case, J. B., Miller, L., Kozodoy, L., Chen, R. E., Carter, L., Walls, A. C., & Park, Y.-J. (2020). De novo design of picomolar SARS-CoV-2 miniprotein inhibitors. *Science*, *370*(6515), 426-431.

Chiti, F., & Dobson, C. M. (2017). Protein misfolding, amyloid formation, and human disease: a summary of progress over the last decade. *Annual review of biochemistry*, *86*(1), 27-68.

Chiti, F., Webster, P., Taddei, N., Clark, A., Stefani, M., Ramponi, G., & Dobson, C. M. (1999). Designing conditions for in vitro formation of amyloid protofilaments and fibrils. *Proceedings of the National Academy of Sciences*, *96*(7), 3590-3594.

Colon, W., & Kelly, J. W. (1992). Partial denaturation of transthyretin is sufficient for amyloid fibril formation in vitro. *Biochemistry*, *31*(36), 8654-8660.

Creighton, T. E. (1993). *Proteins: structures and molecular properties*. Macmillan.

Cui, M., Qi, Q., Gurry, T., Zhao, T., An, B., Pu, J., Gui, X., Cheng, A. A., Zhang, S., & Xun, D. (2019). Modular genetic design of multi-domain functional amyloids: insights into self-assembly and functional properties. *Chemical science*, *10*(14), 4004-4014.

Das, S., Jacob, R. S., Patel, K., Singh, N., & Maji, S. K. (2018). Amyloid Fibrils: Versatile Biomaterials for Cell Adhesion and Tissue Engineering Applications. *Biomacromolecules*, *19*(6), 1826-1839.

De Groot, N. S., Pallarés, I., Avilés, F. X., Vendrell, J., & Ventura, S. (2005). Prediction of" hot spots" of aggregation in disease-linked polypeptides. *BMC Structural Biology*, *5*, 1-15.

Diaz-Caballero, M., Navarro, S., Fuentes, I., Teixidor, F., & Ventura, S. (2018). Minimalist Prion-Inspired Polar Self-Assembling Peptides. *ACS Nano*, *12*(6), 5394-5407.

Díaz-Caballero, M., Navarro, S., Nuez-Martínez, M., Peccati, F., Rodríguez-Santiago, L., Sodupe, M., Teixidor, F., & Ventura, S. (2020). pH-responsive self-assembly of amyloid fibrils for dual hydrolase-oxidase reactions. *Acs Catalysis*, *11*(2), 595-607.

Díaz-Caballero, M., Navarro, S., & Ventura, S. (2021). Functionalized Prion-Inspired Amyloids for Biosensor Applications. *Biomacromolecules*, *22*(7), 2822-2833.

Dill, K. A. (1985). Theory for the folding and stability of globular proteins. *Biochemistry*, *24*(6), 1501-1509.
Dill, K. A., & Chan, H. S. (1997). From Levinthal to pathways to funnels. *Nature structural biology*, *4*(1), 10-19.
Dobson, C. M. (2004). Principles of protein folding, misfolding and aggregation. Seminars in cell & developmental biology,
Eanes, E., & Glenner, G. (1968). X-ray diffraction studies on amyloid filaments. *Journal of Histochemistry & Cytochemistry*, *16*(11), 673-677.
Ebrahimi, S. B., & Samanta, D. (2023). Engineering protein-based therapeutics through structural and chemical design. *Nature communications*, *14*(1), 2411.
Eisenberg, D. S., & Sawaya, M. R. (2017). Structural studies of amyloid proteins at the molecular level. *Annual review of biochemistry*, *86*(1), 69-95.
Eliaz, D., Paul, S., Benyamin, D., Cernescu, A., Cohen, S., Rosenhek-Goldian, I., Brookstein, O., Miali, M., Solomonov, A., & Greenblatt, M. (2022). Micro and nano-scale compartments guide the structural transition of silk protein monomers into silk fibers. *Nature communications*, *13*(1), 7856.
Faltova, L., Küffner, A. M., Hondele, M., Weis, K., & Arosio, P. (2018). Multifunctional protein materials and microreactors using low complexity domains as molecular adhesives. *ACS Nano*, *12*(10), 9991-9999.
Fan, L., Li, J.-L., Cai, Z., & Wang, X. (2021). Bioactive hierarchical silk fibers created by bioinspired self-assembly. *Nature communications*, *12*(1), 2375.
Fernández, M. R., Batlle, C., Gil-García, M., & Ventura, S. (2017). Amyloid cores in prion domains: Key regulators for prion conformational conversion. *Prion*, *11*(1), 31-39.
Ferrone, F. (1999). [17] Analysis of protein aggregation kinetics. In *Methods in enzymology* (Vol. 309, pp. 256-274). Elsevier.
Fersht, A. R. (1995). Optimization of rates of protein folding: the nucleation-condensation mechanism and its implications. *Proceedings of the National Academy of Sciences*, *92*(24), 10869-10873.
Focosi, D., McConnell, S., Casadevall, A., Cappello, E., Valdiserra, G., & Tuccori, M. (2022). Monoclonal antibody therapies against SARS-CoV-2. *The Lancet Infectious Diseases*, *22*(11), e311-e326.
Fowler, D. M., Koulov, A. V., Alory-Jost, C., Marks, M. S., Balch, W. E., & Kelly, J. W. (2006). Functional amyloid formation within mammalian tissue. *PLoS biology*, *4*(1), e6.
Fraser, P. E. (2014). Prions and prion-like proteins. *Journal of Biological Chemistry*, *289*(29), 19839-19840.
Greenwald, J., & Riek, R. (2010). Biology of amyloid: structure, function, and regulation. *Structure*, *18*(10), 1244-1260.
Guijarro, J. I., Sunde, M., Jones, J. A., Campbell, I. D., & Dobson, C. M. (1998). Amyloid fibril formation by an SH3 domain. *Proceedings of the National Academy of Sciences*, *95*(8), 4224-4228.
Harbi, D., & Harrison, P. M. (2014). Classifying prion and prion-like phenomena. *Prion*, *8*(2), 161-165.
Harrison, A. F., & Shorter, J. (2017). RNA-binding proteins with prion-like domains in health and disease. *Biochemical Journal*, *474*(8), 1417-1438.
Hartl, F. U., & Hayer-Hartl, M. (2009). Converging concepts of protein folding in vitro and in vivo. *Nature structural & molecular biology*, *16*(6), 574-581.
Havranek, B., Lindsey, G. W., Higuchi, Y., Itoh, Y., Suzuki, T., Okamoto, T., Hoshino, A., Procko, E., & Islam, S. M. (2023). A computationally designed ACE2 decoy has broad

efficacy against SARS-CoV-2 omicron variants and related viruses in vitro and in vivo. *Communications Biology*, *6*(1), 513.

Herczenik, E., & Gebbink, M. F. (2008). Molecular and cellular aspects of protein misfolding and disease. *The FASEB Journal*, *22*(7), 2115-2133.

Hidaka, Y. (2014). Overview of the regulation of disulfide bond formation in Peptide and protein folding. *Current Protocols in Protein Science*, *76*(1), 28.26. 21-28.26. 26.

Huang, R., Qi, W., Su, R., Zhao, J., & He, Z. (2011). Solvent and surface controlled self-assembly of diphenylalanine peptide: from microtubes to nanofibers. *Soft Matter*, *7*(14), 6418-6421.

Hughes, M. P., Sawaya, M. R., Boyer, D. R., Goldschmidt, L., Rodriguez, J. A., Cascio, D., Chong, L., Gonen, T., & Eisenberg, D. S. (2018). Atomic structures of low-complexity protein segments reveal kinked β sheets that assemble networks. *Science*, *359*(6376), 698-701.

Jahn, T. R., & Radford, S. E. (2008). Folding versus aggregation: polypeptide conformations on competing pathways. *Archives of biochemistry and biophysics*, *469*(1), 100-117.

Jeremiah, S. S., Miyakawa, K., Morita, T., Yamaoka, Y., & Ryo, A. (2020). Potent antiviral effect of silver nanoparticles on SARS-CoV-2. *Biochemical and biophysical research communications*, *533*(1), 195-200.

Johnson, R. T. (2005). Prion diseases. *The Lancet Neurology*, *4*(10), 635-642.

Jumper, J., Evans, R., Pritzel, A., Green, T., Figurnov, M., Ronneberger, O., Tunyasuvunakool, K., Bates, R., Žídek, A., & Potapenko, A. (2021). Highly accurate protein structure prediction with AlphaFold. *Nature*, *596*(7873), 583-589.

Karplus, M., & Weaver, D. L. (1994). Protein folding dynamics: The diffusion-collision model and experimental data. *Protein Science*, *3*(4), 650-668.

Kato, M., Han, T. W., Xie, S., Shi, K., Du, X., Wu, L. C., Mirzaei, H., Goldsmith, E. J., Longgood, J., & Pei, J. (2012). Cell-free formation of RNA granules: low complexity sequence domains form dynamic fibers within hydrogels. *Cell*, *149*(4), 753-767.

Kendrew, J. C., Bodo, G., Dintzis, H. M., Parrish, R., Wyckoff, H., & Phillips, D. C. (1958). A three-dimensional model of the myoglobin molecule obtained by x-ray analysis. *Nature*, *181*(4610), 662-666.

Kim, P. S., & Baldwin, R. L. (1982). Specific intermediates in the folding reactions of small proteins and the mechanism of protein folding. *Annual review of biochemistry*, *51*(1), 459-489.

King, O. D., Gitler, A. D., & Shorter, J. (2012). The tip of the iceberg: RNA-binding proteins with prion-like domains in neurodegenerative disease. *Brain research*, *1462*, 61-80.

Küffner, A. M., Prodan, M., Zuccarini, R., Capasso Palmiero, U., Faltova, L., & Arosio, P. (2020). Acceleration of an enzymatic reaction in liquid phase separated compartments based on intrinsically disordered protein domains. *ChemSystemsChem*, *2*(4), e2000001.

Kwon, I., Kato, M., Xiang, S., Wu, L., Theodoropoulos, P., Mirzaei, H., Han, T., Xie, S., Corden, J. L., & McKnight, S. L. (2013). Phosphorylation-regulated binding of RNA polymerase II to fibrous polymers of low-complexity domains. *Cell*, *155*(5), 1049-1060.

Lee, N. R., Bowerman, C. J., & Nilsson, B. L. (2013). Effects of varied sequence pattern on the self-assembly of amphipathic peptides. *Biomacromolecules*, *14*(9), 3267-3277.

Levinthal, C. (1968). Are there pathways for protein folding? *Journal de chimie physique*, *65*, 44-45.

Li, G., & Sun, S. (2022). Silk fibroin-based biomaterials for tissue engineering applications. *Molecules*, *27*(9), 2757.

Li, J., McQuade, T., Siemer, A. B., Napetschnig, J., Moriwaki, K., Hsiao, Y.-S., Damko, E., Moquin, D., Walz, T., & McDermott, A. (2012). The RIP1/RIP3 necrosome forms a

functional amyloid signaling complex required for programmed necrosis. *Cell*, *150*(2), 339-350.
Li, T., Lu, X. M., Zhang, M. R., Hu, K., & Li, Z. (2022). Peptide-based nanomaterials: Self-assembly, properties and applications. *Bioact Mater*, *11*, 268-282.
Li, Y., Li, B., Fu, Y., Lin, S., & Yang, Y. (2013). Solvent-induced handedness inversion of dipeptide sodium salts derived from alanine. *Langmuir*, *29*(31), 9721-9726.
Li, Y., Tian, R., Zou, Y., Wang, T., & Liu, J. (2024). Strategies and Applications for Supramolecular Protein Self-assembly. *Chemistry–A European Journal*, e202402624.
Liu, J., Wang, D., Zheng, Q., Lu, M., & Arora, P. S. (2008). Atomic structure of a short α-helix stabilized by a main chain hydrogen-bond surrogate. *Journal of the American Chemical Society*, *130*(13), 4334-4337.
Lomakin, A., Chung, D. S., Benedek, G. B., Kirschner, D. A., & Teplow, D. B. (1996). On the nucleation and growth of amyloid beta-protein fibrils: detection of nuclei and quantitation of rate constants. *Proceedings of the National Academy of Sciences*, *93*(3), 1125-1129.
López de la Paz, M., & Serrano, L. (2004). Sequence determinants of amyloid fibril formation. *Proceedings of the National Academy of Sciences*, *101*(1), 87-92.
Luo, Q., Hou, C., Bai, Y., Wang, R., & Liu, J. (2016). Protein assembly: versatile approaches to construct highly ordered nanostructures. *Chemical reviews*, *116*(22), 13571-13632.
Machhi, J., Herskovitz, J., Senan, A. M., Dutta, D., Nath, B., Oleynikov, M. D., Blomberg, W. R., Meigs, D. D., Hasan, M., & Patel, M. (2020). The natural history, pathobiology, and clinical manifestations of SARS-CoV-2 infections. *Journal of neuroimmune pharmacology*, *15*, 359-386.
Macindoe, I., Kwan, A. H., Ren, Q., Morris, V. K., Yang, W., Mackay, J. P., & Sunde, M. (2012). Self-assembly of functional, amphipathic amyloid monolayers by the fungal hydrophobin EAS. *Proceedings of the National Academy of Sciences*, *109*(14), E804-E811.
Maji, S. K., Perrin, M. H., Sawaya, M. R., Jessberger, S., Vadodaria, K., Rissman, R. A., Singru, P. S., Nilsson, K. P. R., Simon, R., & Schubert, D. (2009). Functional amyloids as natural storage of peptide hormones in pituitary secretory granules. *Science*, *325*(5938), 328-332.
Mankar, S., Anoop, A., Sen, S., & Maji, S. K. (2011). Nanomaterials: amyloids reflect their brighter side. *Nano reviews*, *2*(1), 6032.
Marqusee, S., & Baldwin, R. L. (1987). Helix stabilization by Glu-... Lys+ salt bridges in short peptides of de novo design. *Proceedings of the National Academy of Sciences*, *84*(24), 8898-8902.
McParland, V. J., Kad, N. M., Kalverda, A. P., Brown, A., Kirwin-Jones, P., Hunter, M. G., Sunde, M., & Radford, S. E. (2000). Partially unfolded states of β2-microglobulin and amyloid formation in vitro. *Biochemistry*, *39*(30), 8735-8746.
Men, D., Guo, Y.-C., Zhang, Z.-P., Wei, H.-p., Zhou, Y.-F., Cui, Z.-Q., Liang, X.-S., Li, K., Leng, Y., & You, X.-Y. (2009). Seeding-induced self-assembling protein nanowires dramatically increase the sensitivity of immunoassays. *Nano letters*, *9*(6), 2246-2250.
Men, D., Zhang, Z.-P., Guo, Y.-C., Zhu, D.-H., Bi, L.-J., Deng, J.-Y., Cui, Z.-Q., Wei, H.-P., & Zhang, X.-E. (2010). An auto-biotinylated bifunctional protein nanowire for ultra-sensitive molecular biosensing. *Biosensors and Bioelectronics*, *26*(4), 1137-1141.
Men, D., Zhou, J., Li, W., Wei, C.-H., Chen, Y.-Y., Zhou, K., Zheng, Y., Xu, K., Zhang, Z.-P., & Zhang, X.-E. (2018). Self-assembly of antigen proteins into nanowires greatly enhances the binding affinity for high-efficiency target capture. *ACS Applied Materials & Interfaces*, *10*(48), 41019-41025.

Mendes, A. C., Baran, E. T., Reis, R. L., & Azevedo, H. S. (2013). Self-assembly in nature: using the principles of nature to create complex nanobiomaterials. *Wiley interdisciplinary reviews: nanomedicine and nanobiotechnology*, *5*(6), 582-612.

Mittal, A., Manjunath, K., Ranjan, R. K., Kaushik, S., Kumar, S., & Verma, V. (2020). COVID-19 pandemic: Insights into structure, function, and hACE2 receptor recognition by SARS-CoV-2. *PLoS pathogens*, *16*(8), e1008762.

Mondal, S., Adler-Abramovich, L., Lampel, A., Bram, Y., Lipstman, S., & Gazit, E. (2015). Formation of functional super-helical assemblies by constrained single heptad repeat. *Nature communications*, *6*(1), 8615.

Monsellier, E., Ramazzotti, M., Taddei, N., & Chiti, F. (2008). Aggregation propensity of the human proteome. *PLoS Computational Biology*, *4*(10), e1000199.

Moran, S. D., & Zanni, M. T. (2014). How to get insight into amyloid structure and formation from infrared spectroscopy. *The journal of physical chemistry letters*, *5*(11), 1984-1993.

Muschol, M., & Hoyer, W. (2023). Amyloid oligomers as on-pathway precursors or off-pathway competitors of fibrils. *Frontiers in molecular biosciences*, *10*, 1120416.

Nelson, R., & Eisenberg, D. (2006). Recent atomic models of amyloid fibril structure. *Current opinion in structural biology*, *16*(2), 260-265.

Nelson, R., Sawaya, M. R., Balbirnie, M., Madsen, A. Ø., Riekel, C., Grothe, R., & Eisenberg, D. (2005). Structure of the cross-β spine of amyloid-like fibrils. *Nature*, *435*(7043), 773-778.

Nilsson, M. R. (2004). Techniques to study amyloid fibril formation in vitro. *Methods*, *34*(1), 151-160.

Pacheco, M. O., Eccles, L. E., Davies, N. A., Armada, J., Cakley, A. S., Kadambi, I. P., & Stoppel, W. L. (2022). Progress in silk and silk fiber-inspired polymeric nanomaterials for drug delivery. *Frontiers in chemical engineering*, *4*, 1044431.

Pauling, L., & Corey, R. B. (1951). Configurations of polypeptide chains with favored orientations around single bonds: two new pleated sheets. *Proceedings of the National Academy of Sciences*, *37*(11), 729-740.

Pauling, L., Corey, R. B., & Branson, H. R. (1951). The structure of proteins: two hydrogen-bonded helical configurations of the polypeptide chain. *Proceedings of the National Academy of Sciences*, *37*(4), 205-211.

Peña-Díaz, S., Olsen, W. P., Wang, H., & Otzen, D. E. (2024). Functional amyloids: The biomaterials of tomorrow? *Advanced Materials*, *36*(18), 2312823.

Perutz, M. F., Rossmann, M. G., Cullis, A. F., Muirhead, H., Will, G., & North, A. C. (1960). Structure of hæmoglobin: a three-dimensional Fourier synthesis at 5.5-Å. resolution, obtained by X-ray analysis. *Nature*, *185*(4711), 416-422.

Peydayesh, M., Suter, M. K., Bolisetty, S., Boulos, S., Handschin, S., Nyström, L., & Mezzenga, R. (2020). Amyloid fibrils aerogel for sustainable removal of organic contaminants from water. *Advanced Materials*, *32*(12), 1907932.

Pollard, T. D., & Cooper, J. A. (2009). Actin, a central player in cell shape and movement. *Science*, *326*(5957), 1208-1212.

Porta-Pardo, E., Ruiz-Serra, V., Valentini, S., & Valencia, A. (2022). The structural coverage of the human proteome before and after AlphaFold. *PLoS Computational Biology*, *18*(1), e1009818.

Reches, M., & Gazit, E. (2004). Formation of closed-cage nanostructures by self-assembly of aromatic dipeptides. *Nano letters*, *4*(4), 581-585.

Riek, R., & Eisenberg, D. S. (2016). The activities of amyloids from a structural perspective. *Nature*, *539*(7628), 227-235.

Riek, R., & Saupe, S. J. (2016). The HET-S/s prion motif in the control of programmed cell death. *Cold Spring Harbor perspectives in biology*, *8*(9), a023515.

Robang, A. S., Roy, A., Dodd-o, J. B., He, D., Le, J. V., McShan, A. C., Hu, Y., Kumar, V. A., & Paravastu, A. K. (2024). Structural Consequences of Introducing Bioactive Domains to Designer β-Sheet Peptide Self-Assemblies. *Biomacromolecules*, *25*(3), 1429-1438.

Ross, E. D., & Cascarina, S. M. (2023). The roles of prion-like domains in amyloid formation, phase separation, and solubility. In *Structure and Intrinsic Disorder in Enzymology* (pp. 397-426). Elsevier.

Ross, E. D., Minton, A., & Wickner, R. B. (2005). Prion domains: sequences, structures and interactions. *Nature cell biology*, *7*(11), 1039-1044.

Saad, S., Cereghetti, G., Feng, Y., Picotti, P., Peter, M., & Dechant, R. (2017). Reversible protein aggregation is a protective mechanism to ensure cell cycle restart after stress. *Nature cell biology*, *19*(10), 1202-1213.

Saad, S., & Jarosz, D. F. (2021). Protein self-assembly: a new frontier in cell signaling. *Current opinion in cell biology*, *69*, 62-69.

Sabate, R., Rousseau, F., Schymkowitz, J., Batlle, C., & Ventura, S. (2015). Amyloids or prions? That is the question. *Prion*, *9*(3), 200-206.

Sabaté, R., & Ventura, S. (2013). Cross-β-sheet supersecondary structure in amyloid folds: techniques for detection and characterization. *Protein Supersecondary Structures*, 237-257.

Sant'Anna, R., Fernandez, M. R., Batlle, C., Navarro, S., de Groot, N. S., Serpell, L., & Ventura, S. (2016). Characterization of Amyloid Cores in Prion Domains. *Sci Rep*, *6*, 34274.

Sawyer, E. B., Claessen, D., Gras, S. L., & Perrett, S. (2012). Exploiting amyloid: how and why bacteria use cross-β fibrils. *Biochemical Society Transactions*, *40*(4), 728-734.

Schmuck, B., Gudmundsson, M., Blomqvist, J., Hansson, H., Hard, T., & Sandgren, M. (2018). Production of ready-to-use functionalized Sup35 nanofibrils secreted by Komagataella pastoris. *ACS Nano*, *12*(9), 9363-9371.

Schmuck, B., Gudmundsson, M., Härd, T., & Sandgren, M. (2019). Coupled chemistry kinetics demonstrate the utility of functionalized Sup35 amyloid nanofibrils in biocatalytic cascades. *Journal of Biological Chemistry*, *294*(41), 14966-14977.

Schmuck, B., Sandgren, M., & Härd, T. (2017). A fine-tuned composition of protein nanofibrils yields an upgraded functionality of displayed antibody binding domains. *Biotechnology journal*, *12*(6), 1600672.

Seth, P., Mukherjee, A., & Sarkar, N. (2023). Formation of hen egg white lysozyme derived amyloid-based hydrogels using different gelation agents: A potential tool for drug delivery. *International Journal of Biological Macromolecules*, *253*, 127177.

Seuring, C., Verasdonck, J., Ringler, P., Cadalbert, R., Stahlberg, H., Böckmann, A., Meier, B. H., & Riek, R. (2017). Amyloid fibril polymorphism: almost identical on the atomic level, mesoscopically very different. *The Journal of Physical Chemistry B*, *121*(8), 1783-1792.

Shimanovich, U., Bernardes, G. J., Knowles, T., & Cavaco-Paulo, A. (2014). Protein micro-and nano-capsules for biomedical applications. *Chemical Society Reviews*, *43*(5), 1361-1371.

Si, K., Lindquist, S., & Kandel, E. R. (2003). A neuronal isoform of the aplysia CPEB has prion-like properties. *Cell*, *115*(7), 879-891.

Solomonov, A., Kozell, A., & Shimanovich, U. (2024). Designing Multifunctional Biomaterials via Protein Self-Assembly. *Angewandte Chemie International Edition*, *63*(14), e202318365.

Soon, W. L., Peydayesh, M., Mezzenga, R., & Miserez, A. (2022). Plant-based amyloids from food waste for removal of heavy metals from contaminated water. *Chemical Engineering Journal*, *445*, 136513.

Stefani, M. (2010). Biochemical and biophysical features of both oligomer/fibril and cell membrane in amyloid cytotoxicity. *The FEBS journal*, *277*(22), 4602-4613.

Taglialegna, A., Navarro, S., Ventura, S., Garnett, J. A., Matthews, S., Penades, J. R., Lasa, I., & Valle, J. (2016). Staphylococcal Bap proteins build amyloid scaffold biofilm matrices in response to environmental signals. *PLoS pathogens*, *12*(6), e1005711.

Tanford, C. (1962). Contribution of hydrophobic interactions to the stability of the globular conformation of proteins. *Journal of the American Chemical Society*, *84*(22), 4240-4247.

Toombs, J. A., McCarty, B. R., & Ross, E. D. (2010). Compositional determinants of prion formation in yeast. *Molecular and cellular biology*, *30*(1), 319-332.

Toombs, J. A., Petri, M., Paul, K. R., Kan, G. Y., Ben-Hur, A., & Ross, E. D. (2012). De novo design of synthetic prion domains. *Proceedings of the National Academy of Sciences*, *109*(17), 6519-6524.

Uversky, V. N. (2010). Mysterious oligomerization of the amyloidogenic proteins. *The FEBS journal*, *277*(14), 2940-2953.

Uversky, V. N., & Fink, A. L. (2004). Conformational constraints for amyloid fibrillation: the importance of being unfolded. *Biochimica et Biophysica Acta (BBA)-Proteins and Proteomics*, *1698*(2), 131-153.

Varadi, M., Anyango, S., Deshpande, M., Nair, S., Natassia, C., Yordanova, G., Yuan, D., Stroe, O., Wood, G., & Laydon, A. (2022). AlphaFold Protein Structure Database: massively expanding the structural coverage of protein-sequence space with high-accuracy models. *Nucleic Acids Research*, *50*(D1), D439-D444.

Varela, A. E., Lang, J. F., Wu, Y., Dalphin, M. D., Stangl, A. J., Okuno, Y., & Cavagnero, S. (2018). Kinetic trapping of folded proteins relative to aggregates under physiologically relevant conditions. *The Journal of Physical Chemistry B*, *122*(31), 7682-7698.

Vazquez-Sanchez, S., Tilkin, B., Gasset-Rosa, F., Zhang, S., Piol, D., McAlonis-Downes, M., Artates, J., Govea-Perez, N., Verresen, Y., & Guo, L. (2024). Frontotemporal dementia-like disease progression elicited by seeded aggregation and spread of FUS. *Molecular Neurodegeneration*, *19*(1), 46.

Wang, J., Han, S., Meng, G., Xu, H., Xia, D., Zhao, X., Schweins, R., & Lu, J. R. (2009). Dynamic self-assembly of surfactant-like peptides A 6 K and A 9 K. *Soft Matter*, *5*(20), 3870-3878.

Wang, J., Liu, K., Xing, R., & Yan, X. (2016). Peptide self-assembly: thermodynamics and kinetics. *Chemical Society Reviews*, *45*(20), 5589-5604.

Wang, W., Azizyan, R. A., Garro, A., Kajava, A. V., & Ventura, S. (2020). Multifunctional Amyloid Oligomeric Nanoparticles for Specific Cell Targeting and Drug Delivery. *Biomacromolecules*, *21*(10), 4302-4312.

Wang, W., Gil-Garcia, M., & Ventura, S. (2021). Dual Antibody-Conjugated Amyloid Nanorods to Promote Selective Cell–Cell Interactions. *ACS Applied Materials & Interfaces*, *13*(13), 14875-14884.

Wang, W., Navarro, S., Azizyan, R. A., Baño-Polo, M., Esperante, S. A., Kajava, A. V., & Ventura, S. (2019). Prion soft amyloid core driven self-assembly of globular proteins into bioactive nanofibrils. *Nanoscale*, *11*(26), 12680-12694.

Wang, W., & Ventura, S. (2020). Prion domains as a driving force for the assembly of functional nanomaterials. *Prion*, *14*(1), 170-179.

Wang, X., Cao, R., Zhang, H., Liu, J., Xu, M., Hu, H., Li, Y., Zhao, L., Li, W., & Sun, X. (2020). The anti-influenza virus drug, arbidol is an efficient inhibitor of SARS-CoV-2 in vitro. *Cell discovery*, *6*(1), 28.

Wang, X., Zhang, S., Zhang, J., Wang, Y., Jiang, X., Tao, Y., Li, D., Zhong, C., & Liu, C. (2023). Rational design of functional amyloid fibrillar assemblies. *Chemical Society Reviews*, *52*(14), 4603-4631.

Whitesides, G. M., & Grzybowski, B. (2002). Self-assembly at all scales. *Science*, *295*(5564), 2418-2421.

Wickner, R. B., Masison, D. C., & Edskes, H. K. (1995). [PSI] and [URE3] as yeast prions. *Yeast*, *11*(16), 1671-1685.

Wu, M.-B., Yang, F., Yang, J., Zhong, Q., Körstgen, V., Yang, P., Müller-Buschbaum, P., & Xu, Z.-K. (2020). Lysozyme membranes promoted by hydrophobic substrates for ultrafast and precise organic solvent nanofiltration. *Nano letters*, *20*(12), 8760-8767.

Yadav, S. S., Padhy, P. K., Singh, A. K., Sharma, S., Fatima, S., Sinha, A., Tariq, R., Sharma, S. K., & Priya, S. (2024). Advancements in amyloid-based biological materials for healthcare, environmental and sensing applications. *Materials Advances*, *5*(10), 4078-4090.

Zhou, X.-M., Shimanovich, U., Herling, T. W., Wu, S., Dobson, C. M., Knowles, T. P., & Perrett, S. (2015). Enzymatically active microgels from self-assembling protein nanofibrils for microflow chemistry. *ACS Nano*, *9*(6), 5772-5781.

Zhou, X. M., Entwistle, A., Zhang, H., Jackson, A. P., Mason, T. O., Shimanovich, U., Knowles, T. P., Smith, A. T., Sawyer, E. B., & Perrett, S. (2014). Self-assembly of amyloid fibrils that display active enzymes. *ChemCatChem*, *6*(7), 1961-1968.

Zhu, J., Avakyan, N., Kakkis, A., Hoffnagle, A. M., Han, K., Li, Y., Zhang, Z., Choi, T. S., Na, Y., & Yu, C.-J. (2021). Protein assembly by design. *Chemical reviews*, *121*(22), 13701-13796.

Zwanzig, R., Szabo, A., & Bagchi, B. (1992). Levinthal's paradox. *Proceedings of the National Academy of Sciences*, *89*(1), 20-22.

ANNEX 1: Supplementary materials Chapter 1

Bioengineered self-assembled nanofibrils for high-affinity SARS-CoV-2 capture and neutralization

Molood Behbahanipour, Susanna Navarro, Oriol Bárcenas, Javier Garcia-Pardo, Salvador Ventura *

Journal of Colloid And Interface Science

2024

https://doi.org/10.1016/j.jcis.2024.06.175

Supporting Information

Bioengineered Self-Assembled Nanofibrils for High-Affinity SARS-CoV-2 Capture and Neutralization

Molood BehBahanipour[a], *Susanna Navarro*[a], *Oriol Bárcenas*[a], *Javier Garcia-Pardo*[a] *and Salvador Ventura*[a,*]

[a]Institut de Biotecnologia i de Biomedicina (IBB) and Departament de Bioquímica i Biologia Molecular; Universitat Autònoma de Barcelona; 08193 Bellaterra (Barcelona), Spain.

*Correspondence: Salvador.Ventura@uab.cat (S.V.); Tel.: +34-93-586-8956 (S.V.)

Supporting Tables

Table S1. Sup35-LCB1/LCB3 self-assembly conditions and fibril yields, relative to initial fusion protein concentration.

Na-PB concentration (mM)	Sup35-LCB1	Sup35-LCB3
20 mM	15%	14%
150 mM	33%	29%
300 mM	58%	40%

Table S2. Secondary structure assignments of amide I band components in the Sup35-LCB1/LCB3 nanofibrils by ATR-FTIR spectroscopy.

Na-PB concentration (mM)	Sup35-LCB1			Sup35-LCB3		
	Wavenumber (cm^{-1})	**Band Assignment**	**Area (%)**	**Wavenumber (cm^{-1})**	**Band Assignment**	**Area (%)**
20 mM	1628.3	Amyloid-like inter-molecular β-sheet structure	36.8%	1628.6	Amyloid-like inter-molecular β-sheet structure	30.4%
	1651.7	α-helix	49.1%	1652.1	α-helix	49.6%
	1673.8	β-Turn / Loop + Turn	14.1%	1673.7	β-Turn / Loop + Turn	20%
150 mM	1628.3	Amyloid-like inter-molecular β-sheet structure	37.6%	1628.6	Amyloid-like inter-molecular β-sheet structure	32%
	1651.5	α-helix	48.6%	1651.2	α-helix	52.1%
	1673.5	β-Turn / Loop + Turn	13.8%	1673.3	β-Turn / Loop + Turn	15.9%
300 mM	1626.9	Amyloid-like inter-molecular β-sheet structure	40.7%	1629.0	Amyloid-like inter-molecular β-sheet structure	29.8%
	1650.4	α-helix	48.5%	1651.6	α-helix	54.5%
	1675.9	Parallel β-strand / Loop + Turn	10.8%	1673.8	β-Turn / Loop + Turn	15.7%

Supporting Figures

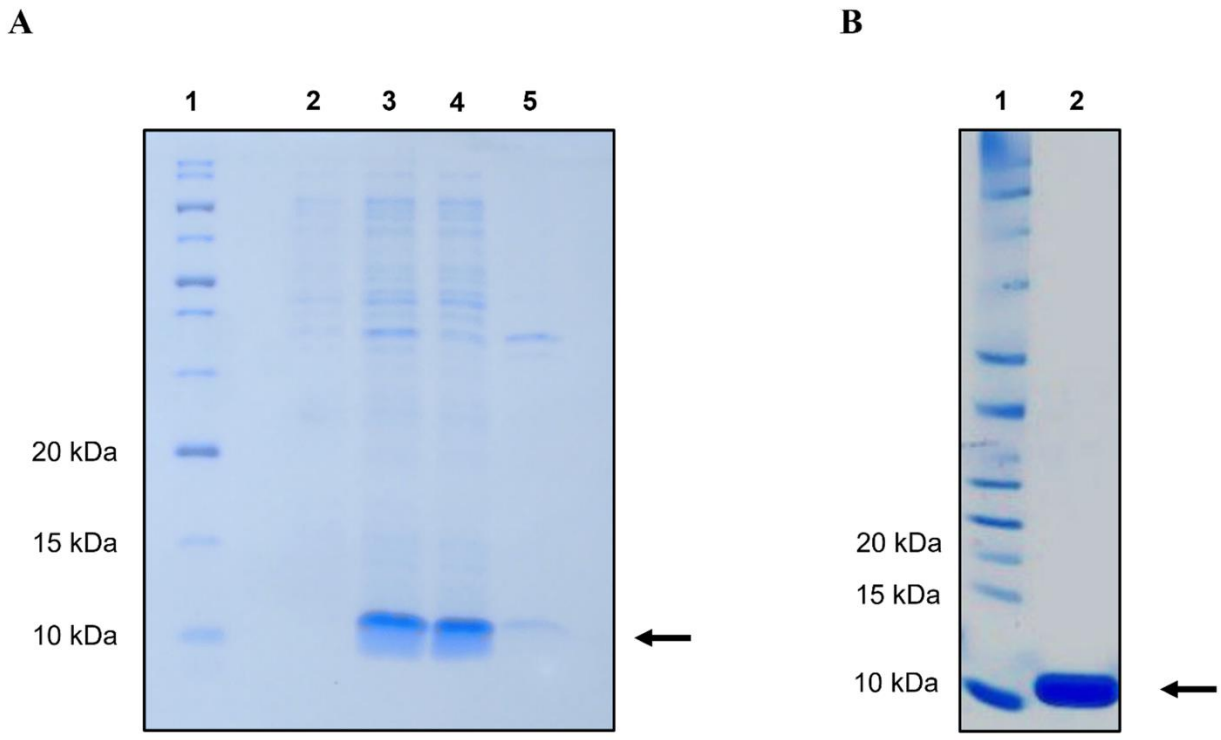

Fig. S1. Expression and purification of soluble Sup35-LCB1 fusion protein. (A) SDS-PAGE analysis of Sup35-LCB1 expression: Lane 1, molecular weight marker (MW); lane 2, non-induced culture; lane 3, total extract of induced culture; lane 4, soluble fraction; lane 5, insoluble fraction. (B) SDS-PAGE analysis of Sup35-LCB1 fusion protein purified by size exclusion chromatography: Lane 1, MW; Lane 2, purified Sup35-LCB1 protein. Note that the band corresponding to Sup35-LCB1 (10.56 kDa) is indicated with a black arrow.

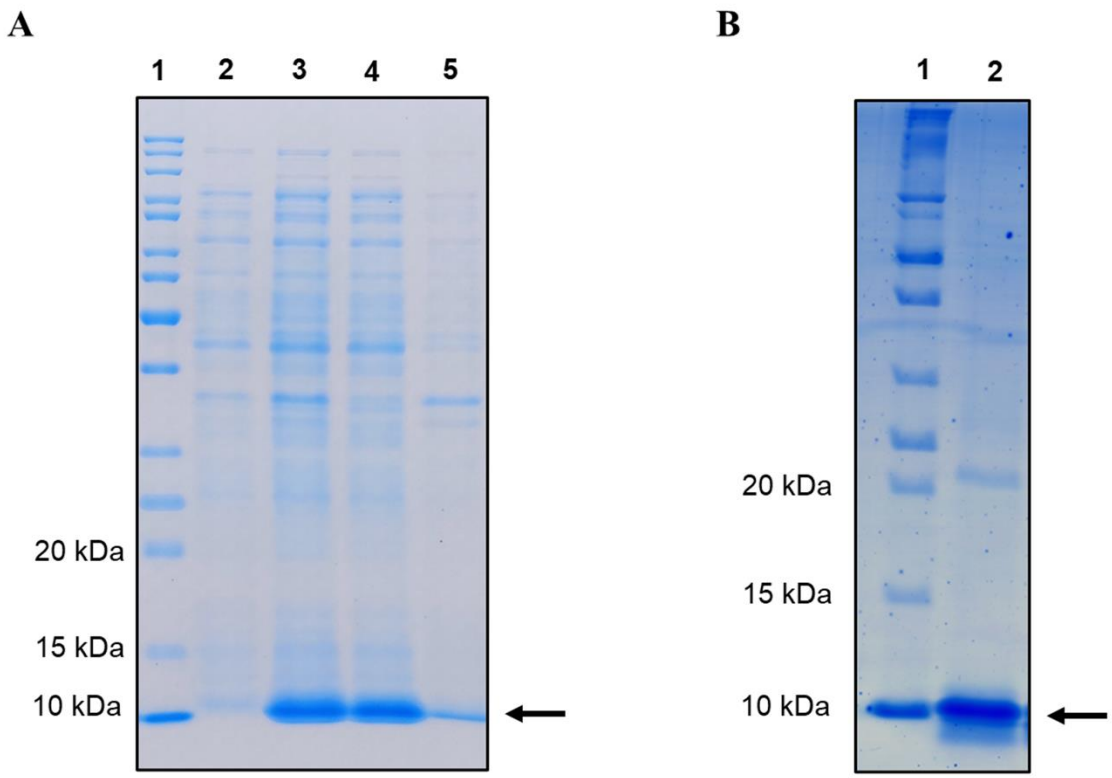

Fig. S2. Expression and purification of soluble Sup35-LCB3 fusion protein. (A) SDS-PAGE analysis of the Sup35-LCB3 expression: Lane 1, molecular weight marker (MW), lane 2, non-induced culture, lane 3, total extract of induced culture, lane 4, soluble fraction, lane 5, insoluble fraction. (B) SDS-PAGE analysis of Sup35-LCB3 fusion protein purified by size exclusion chromatography: Lane 1, MW; Lane 2, purified Sup35-LCB3 protein. Note that the band corresponding to Sup35-LCB3 (11.49 kDa) is indicated with a black arrow.

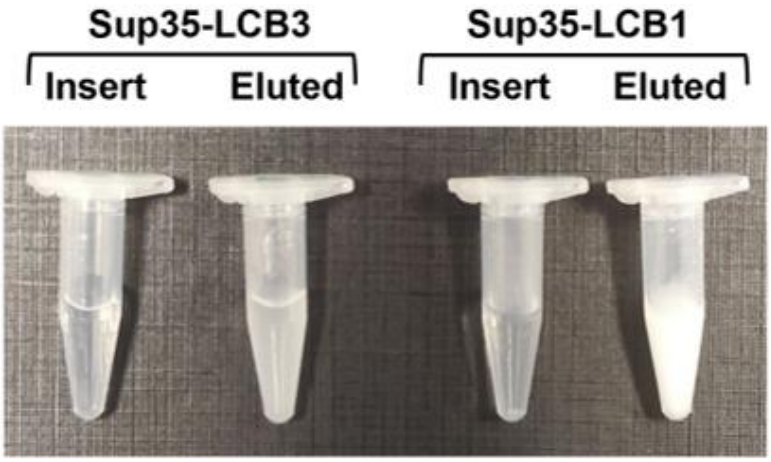

Samples	Abs 360_Insert	Abs 360_Eluted
Sup35-LCB1 (10 fold dilution)	0.011	> 1.5
Sup35-LCB3 (10 fold dilution)	0.014	0.308

Fig. S3. Sup35-LCB1/LCB3 solubility in Milli-Q™ water. Top panel: Turbidity of the Sup35-LCB1/LCB3 before and after exchanging the buffer with double-distilled Milli-Q™ water. Bottom panel: Absorbance values of LCB1/LCB3 samples shown in the upper panel. Note that both protein solutions exhibit increased turbidity and light scattering at 360 nm.

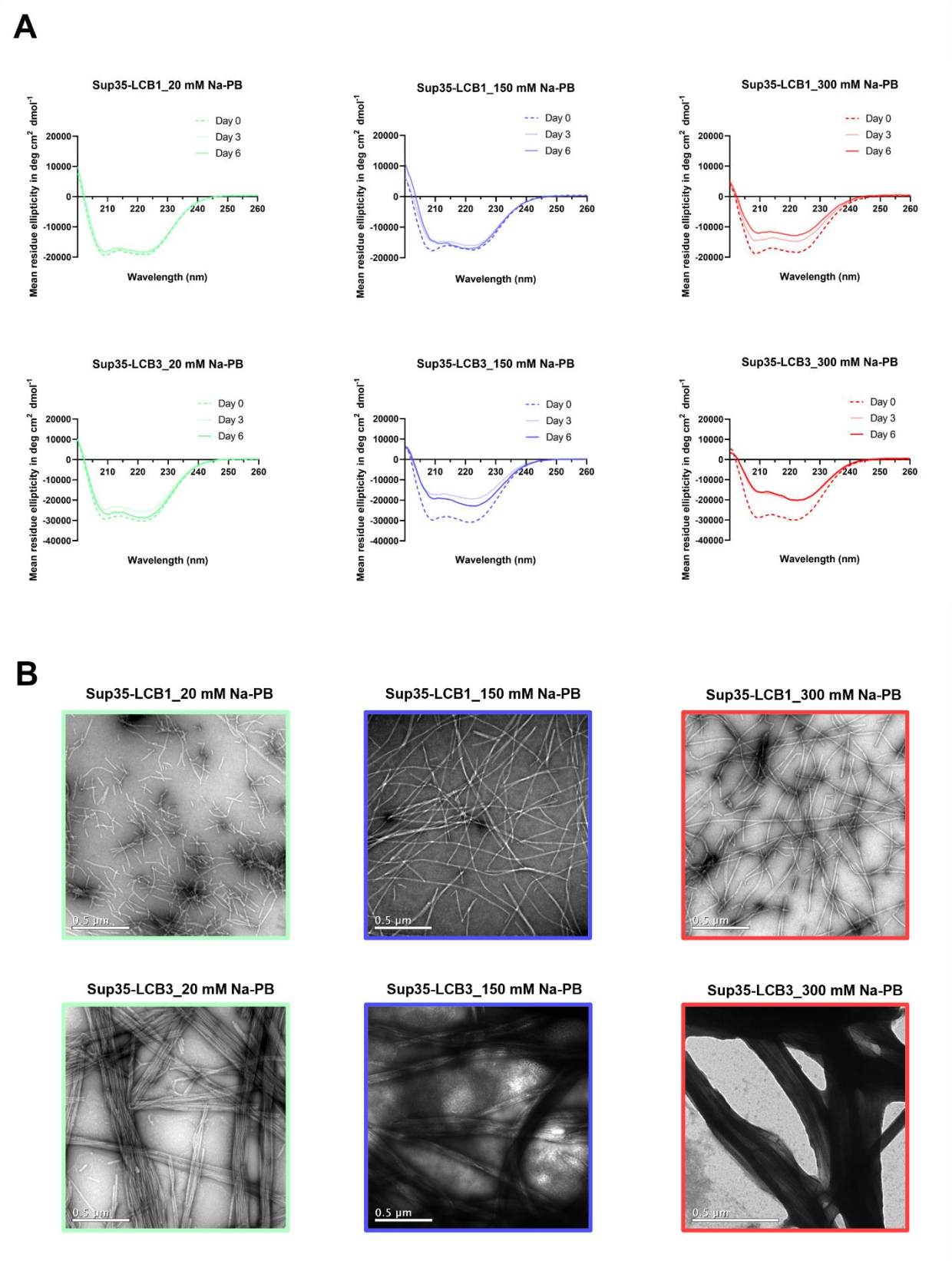

Fig. S4. Biophysical characterization of the Sup35-LCB1/LCB3 fibrils at different salt concentrations. (A) CD spectra of the Sup35-LCB1/LCB3 protein samples collected at

different time points (i.e., day 0, day 3, and day 6) under various Na-PB conditions (i.e., 20, 150, and 300 mM). Each spectrum represents the average of 20 scans. The reduction in signal intensity at 209 nm and 222 nm over time suggests a change in secondary structure as fibrillation progresses. (B) TEM images of protein fibrils self-assembled at 20 mM (green), 150 mM (blue), and 300 mM (red) Na-PB obtained on Day 6 of the fibrillation process. In all the images, the scale bar is 0.5 μm.

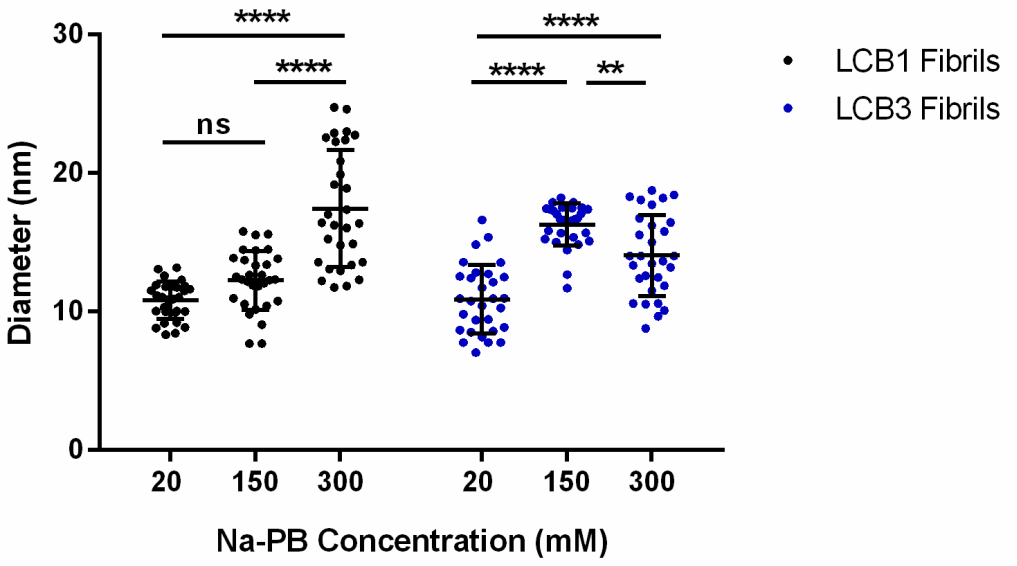

Fig. S5. Diameter of individual Sup35-LCB1 and Sup35-LCB3 amyloid fibrils prepared in different salt conditions (*i.e.*, 20, 150, and 300 mM Na-PB). Ns, indicates no statistically significant difference. **$p < 0.01$, ****$p < 0.0001$.

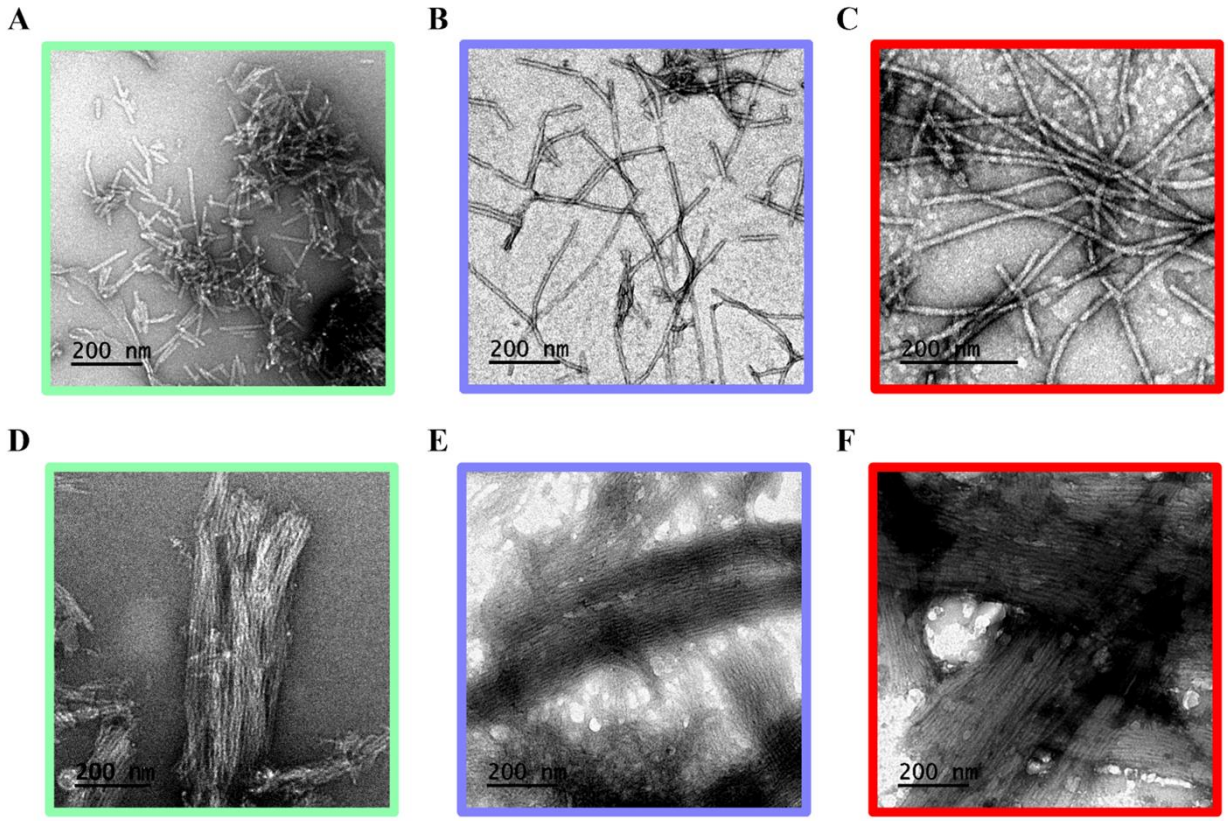

Fig. S6. Transmission Electron Microscopy (NS-TEM) micrographs of Sup35-LCB1/3 self-assembled nanofibrils after 1 month incubation at RT. (A-C) NS-TEM images of Sup35-LCB1 nanofibrils prepared at (A) 20 mM, (B) 150 mM and (C) 300 mM Na-PB. (D-F) NS-TEM images of Sup35-LCB3 nanofibrils prepared at (D) 20 mM, (E) 150 mM and (F) 300 mM Na-PB. In all the images, the scale bar is 200 nm.

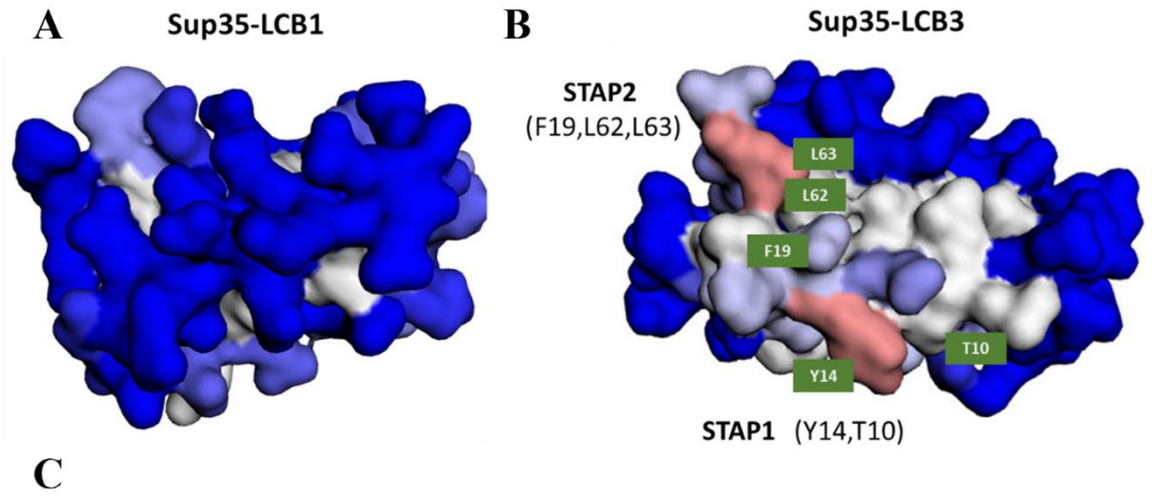

C

Protein variant	*Num charges (KR+DE)*	*+ charges*	*- charges*	*Total charge*	*pI*	*Num aas*	*A3D average score*	*A3D max score*
LCB1 wt	24	8	16	-8	4.47	55	-1.9827	0
LCB3 wt	27	11	16	-5	4.94	64	-1.8691	0.3102

Fig. S7. Aggrescan 3D (A3D) analysis of LCB1 and LCB3 binders. (A, B) Crystal structures of (A) LCB1 and (B) LCB3 proteins showing the corresponding A3D predictions. Predicted aggregation propensities are colored in the structure ranging from blue (more solubilizing residues) to red (aggregation-prone residues). The position of the two predicted hydrophobic patches in LCB3 is indicated. LCB1/3 structures are shown in equivalent spatial orientations. PDB accession codes used for calculations are: LCB1 (PDB 7JZU) and LCB3 (PDB 7JZM). (C) Summary of the A3D derived parameters. A3D 2.0 [1] was used for calculations.

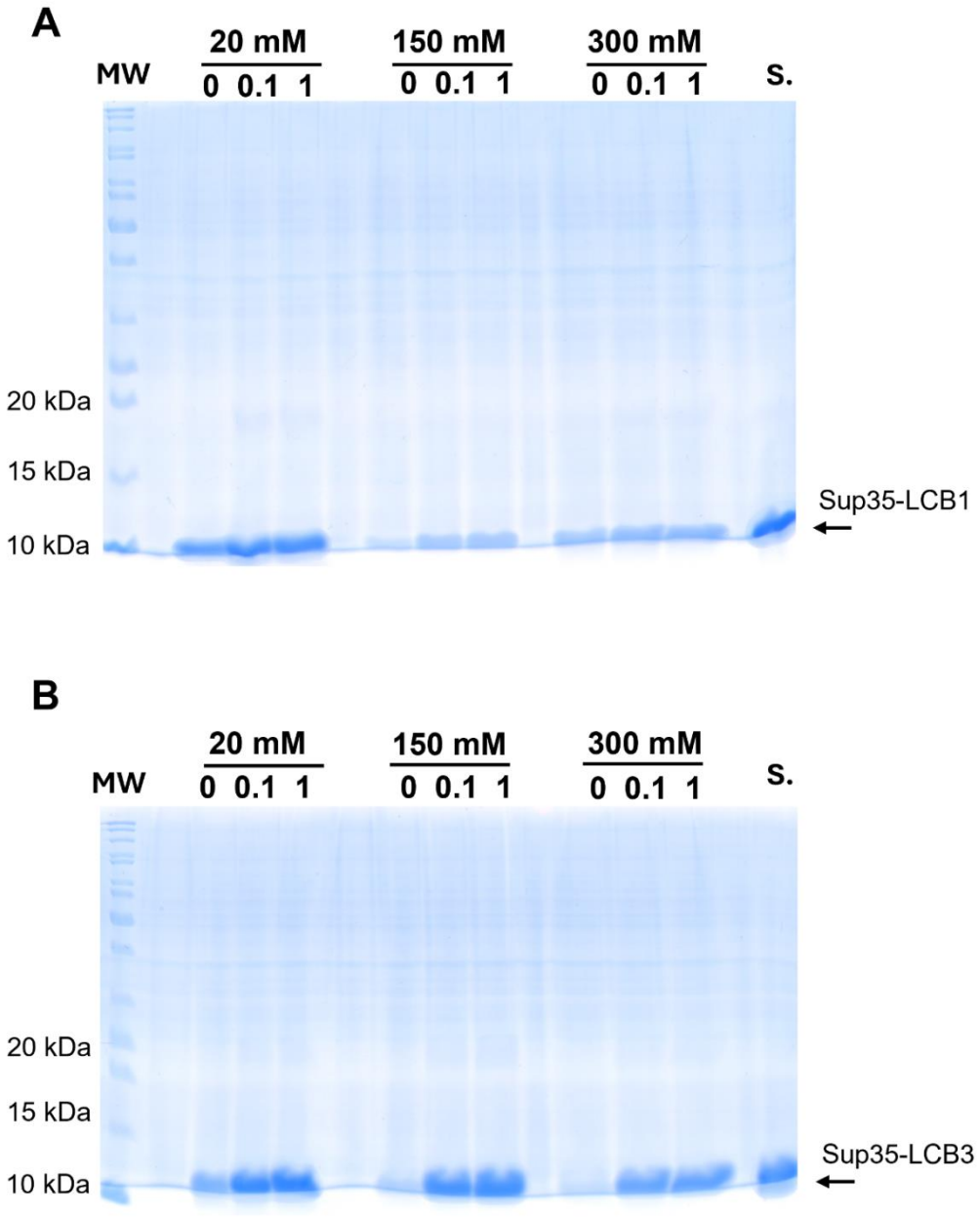

Fig. S8. Effect of SDS on the stability of Sup35-LCB1/3 self-assembled nanofibrils. (A) Sup35-LCB1 and (B) Sup35-LCB3 fibrils formed at three different Na-PB conditions were incubated with varying SDS concentrations (0, 0.1, and 1%), as described in the experimental section. The SDS-solubilized monomeric proteins at different SDS concentrations (0.1 and 1 % w/v) were analyzed by SDS-PAGE. The arrow indicates the extent of fibril dissociation under the indicated condition. S stands for each Sup35-LCB1 and Sup35-LCB3 soluble monomeric protein.

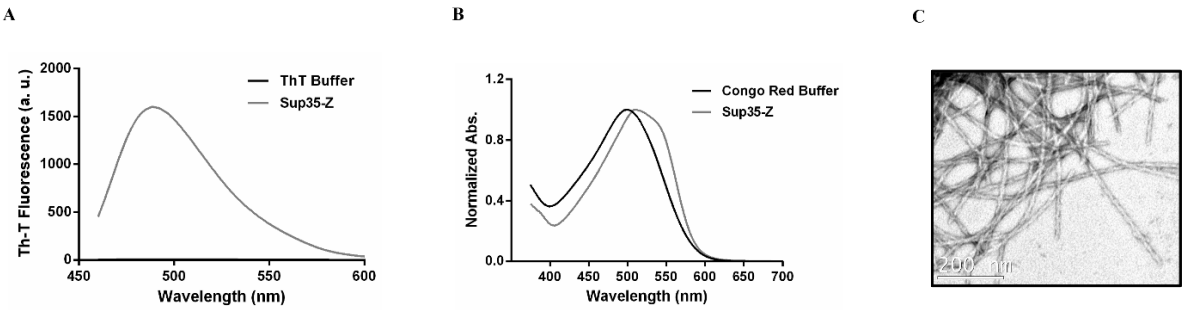

Fig. S9. Biophysical characterization of Sup35-Z fusion protein. (A) Th-T fluorescence emission spectra in the absence (black line) or in the presence of Sup35-Z nanofibrils. (B) CR normalized absorbance spectra recorded in the range from 375 to 700 nm in the absence (black line) or in the presence of Sup35-Z self-assembled nanofibrils (C) NS-TEM images of Sup35-Z nanofibrils prepared in PBS buffer after 5 days incubation at 37°C and 600 rpm. Scale bar is 200 nm.

Supporting References

[1] A. Kuriata, V. Iglesias, J. Pujols, M. Kurcinski, S. Kmiecik, S. Ventura, Aggrescan3D (A3D) 2.0: prediction and engineering of protein solubility, Nucleic Acids Res. 47 (2019) W300-W307. https://doi.org/10.1093/nar/gkz321.

ANNEX 2: Supplementary materials Chapter 2

OligoBinders: Bioengineered Soluble Amyloid-like Nanoparticles to Bind and Neutralize SARS-CoV-2

Molood Behbahanipour, Roger Benoit, Susanna Navarro*, and Salvador Ventura*

ACS Applied Materials & Interfaces

2023

https://doi.org/10.1021/acsami.2c18305

Supporting Information

OligoBinders: Bioengineered soluble amyloid-like nanoparticles to bind and neutralize SARS-CoV-2

Molood Behbahanipour[1], Roger Benoit[2], Susanna Navarro[1*] and Salvador Ventura[1*]

[1]Institut de Biotecnologia i de Biomedicina (IBB) and Departament de Bioquímica i Biologia Molecular; Universitat Autònoma de Barcelona; 08193 Bellaterra (Barcelona), Spain.

[2]Laboratory of Nanoscale Biology, Division of Biology and Chemistry, Paul Scherrer Institute, 5232 Villigen PSI, Switzerland.

*Corresponding authors

E-mail:

Susanna.Navarro.Cantero@uab.cat (Susanna Navarro)

Salvador.Ventura@uab.cat (Salvador Ventura)

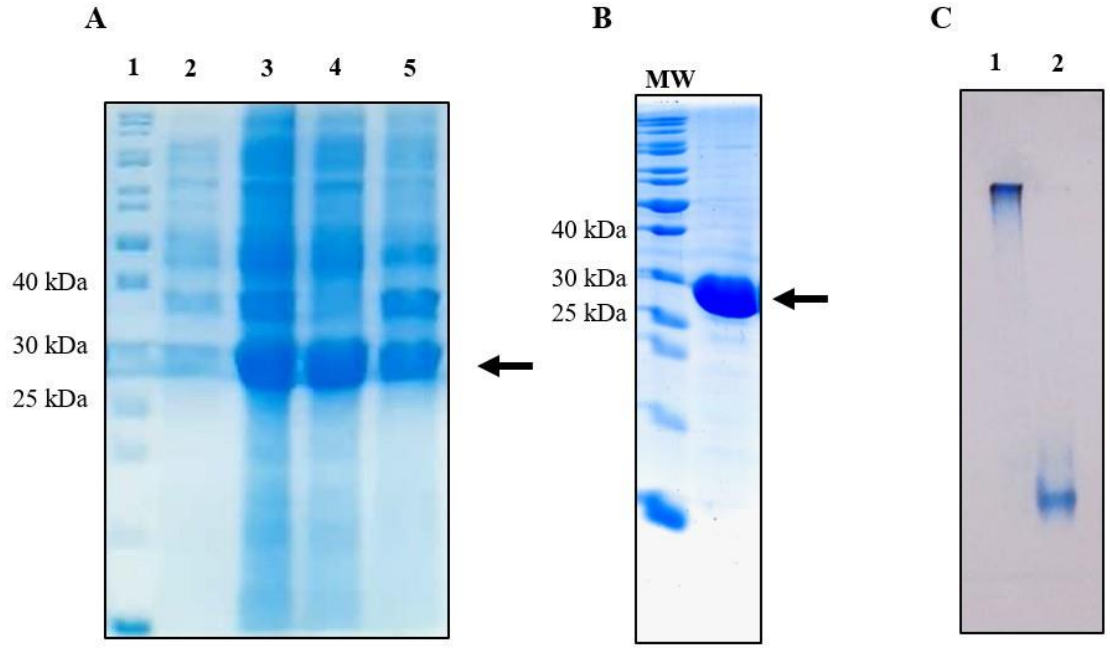

Figure S-1. Expression and purification of soluble and oligomeric Sup35-DHFR-LCB1 fusion protein. (A) SDS-PAGE analysis of the expression of Sup35-DHFR-LCB1 (28,8 kDa): Lane 1, corresponds to the molecular weight marker (MW), lane 2, non-induced culture, lane 3, total extract of induced culture, lane 4, soluble fraction (supernatant), lane 5, insoluble fraction (pellet). (B) SDS-PAGE analysis of purified Sup35-DHFR-LCB1 (28,8 kDa) by gel filtration. A black arrow indicates the band corresponding to Sup35-DHFR-LCB1. (C) Native- PAGE gel analysis of purified oligomers: Lane 1, corresponds to purified oligomers, Lane 2, soluble Sup35-DHFR-LCB1.

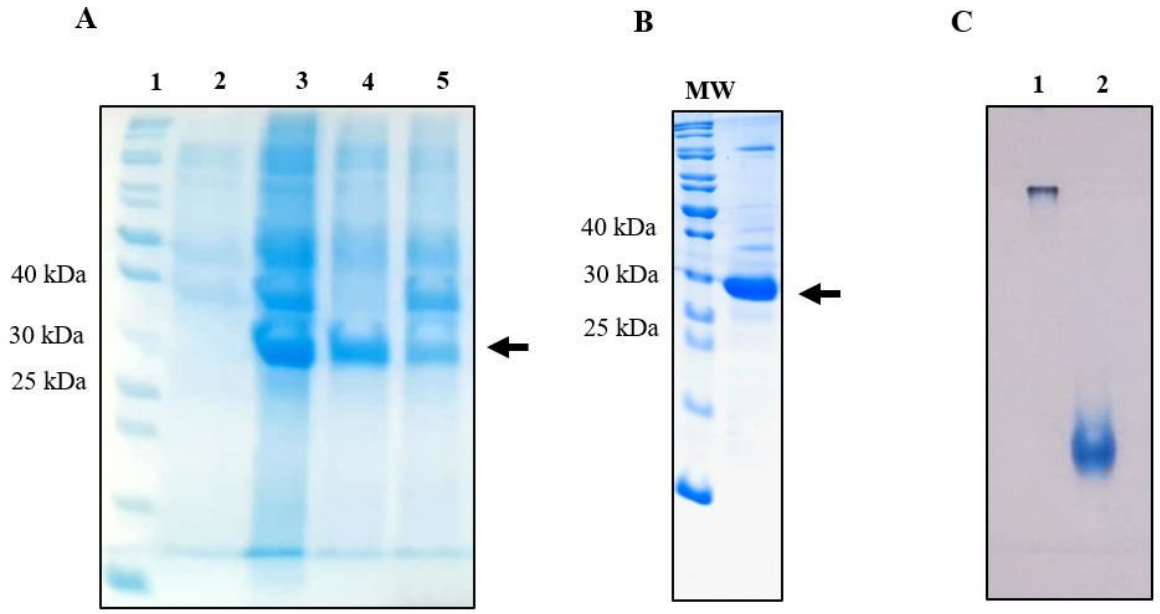

Figure S-2. Expression and purification of soluble and oligomeric Sup35-DHFR-LCB3 fusion protein. (A) SDS-PAGE analysis of the expression of Sup35-DHFR-LCB3 (29.7 kDa): Lane 1, corresponds to the molecular weight marker (MW), lane 2, non-induced culture, lane 3, total extract of induced culture, lane 4, soluble fraction (supernatant), lane 5, insoluble fraction (pellet). (B) SDS-PAGE analysis of purified Sup35-DHFR-LCB3 (29.7 kDa) by gel filtration. A black arrow indicates the band corresponding to Sup35-DHFR-LCB3. (C) Native-PAGE gel analysis of purified oligomers: Lane 1, corresponds to purified oligomers, Lane 2, soluble Sup35-DHFR-LCB3.

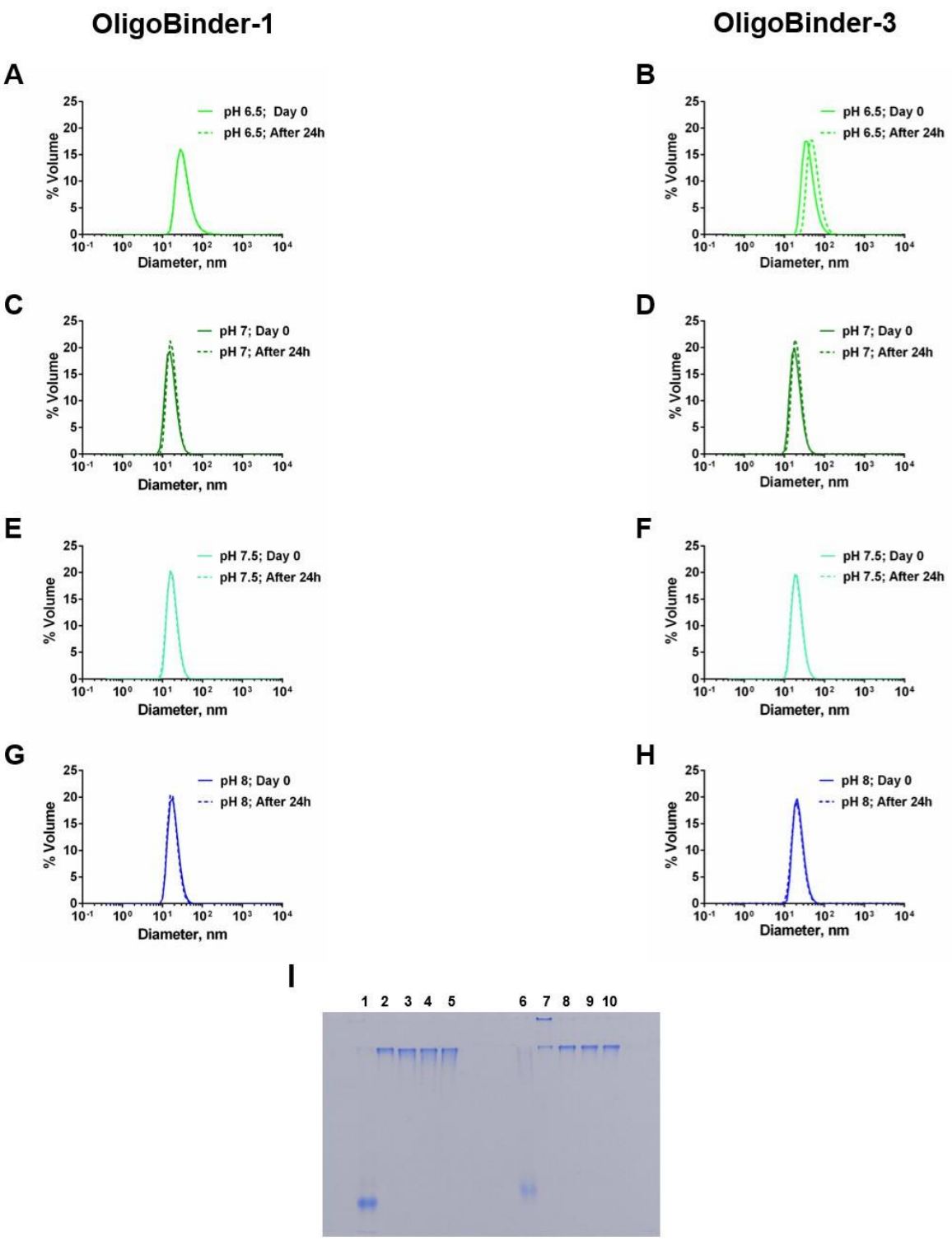
OligoBinder-1
OligoBinder-3
A
B
C
D
E
F
G
H
I
pH 6.5; Day 0
pH 6.5; After 24h
pH 7; Day 0
pH 7; After 24h
pH 7.5; Day 0
pH 7.5; After 24h
pH 8; Day 0
pH 8; After 24h
% Volume
Diameter, nm
1 2 3 4 5 6 7 8 9 10

Figure S-3. Characterization of size distribution of OligoBinders 1 and 3 at different pHs at time 0 and after 24h incubation. (A-H) Size distribution of OligoBinders 1 and 3 at different pHs (6.5, 7.0, 7.5, 8.0) measured by DLS. (I) Native-PAGE gel analysis of purified oligomers at different pHs: Lane 1 and 6 correspond to purified soluble monomeric Sup35-DHFR-LCB1 and 3, respectively. Lane 2 to 5, correspond to OligoBinder-1 incubated for 24h at pH 6.5; pH 7.0; pH 7.5; and pH 8.0, respectively. Lane 7 to 10, correspond to OligoBinder-3 incubated for 24h at pH 6.5; pH 7.0; pH 7.5; pH 8.0, respectively.

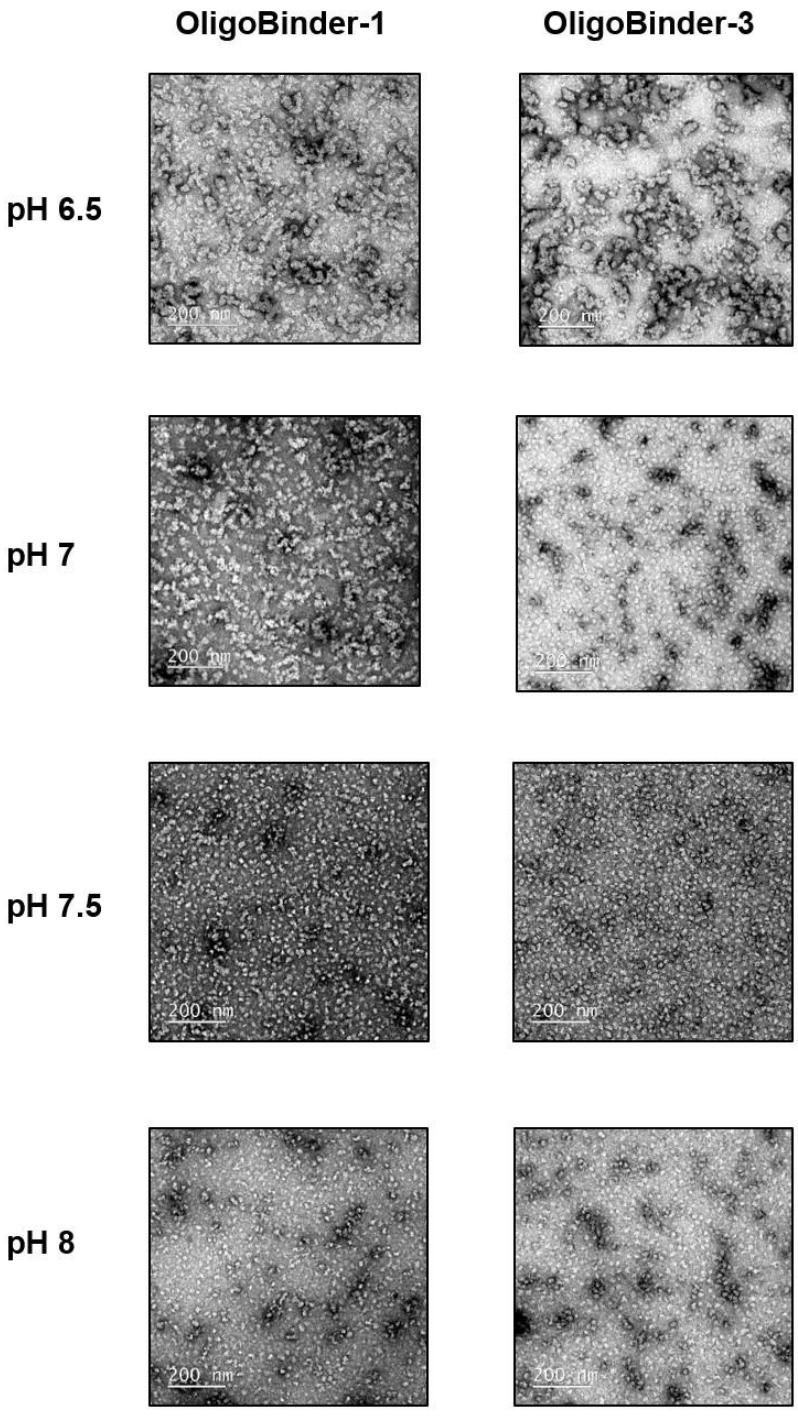

Figure S-4. TEM images of OligoBinders 1 and 3 incubated for 24h at different pH.

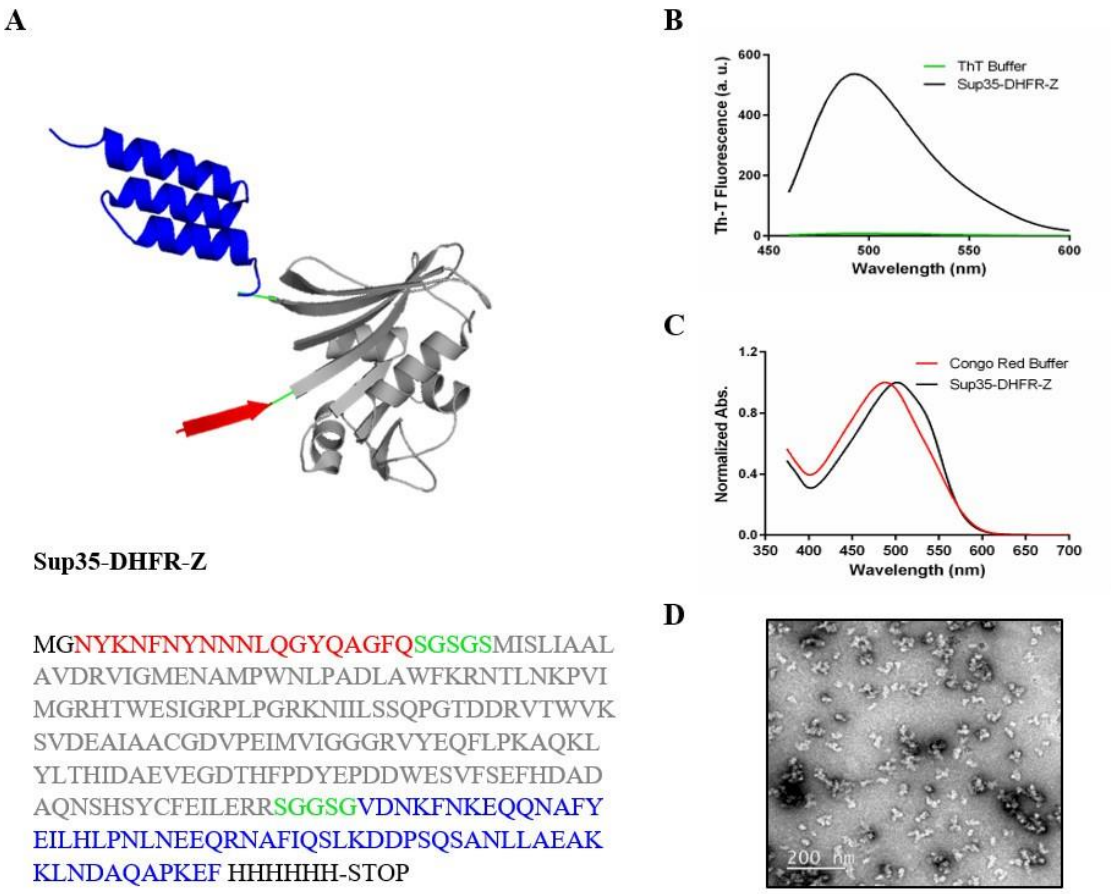

Figure S-5. Schematic representation and biophysical characterization of oligomeric Sup35-DHFR-Z fusion protein. (A) Cartoon representation and sequence of Sup35-DHFR-Z fusion protein. The SAC (residues 100 to 118 of Sup35 protein) fused to DHFR followed by a Z-domain (PDB: 1Q2N) of Staphylococcus aureus protein A; are shown in red, grey and blue, respectively. The three different moieties are linked by S/G linkers shown in green. (B) Fluorescence emission spectra of Th-T recorded upon 445 nm excitation in the absence (green line) and in the presence of 20 μM oligomeric (black) protein. (C) Congo Red normalized absorbance spectra were recorded in the range from 375 to 700 nm in the absence (red line)

and in the presence of 20 μM oligomeric (black) protein. (D) Transmission electron micrographs of negatively stained amyloid-like oligomeric particles formed by Sup35-DHFR-Z. Scale bar corresponds to 200 nm.

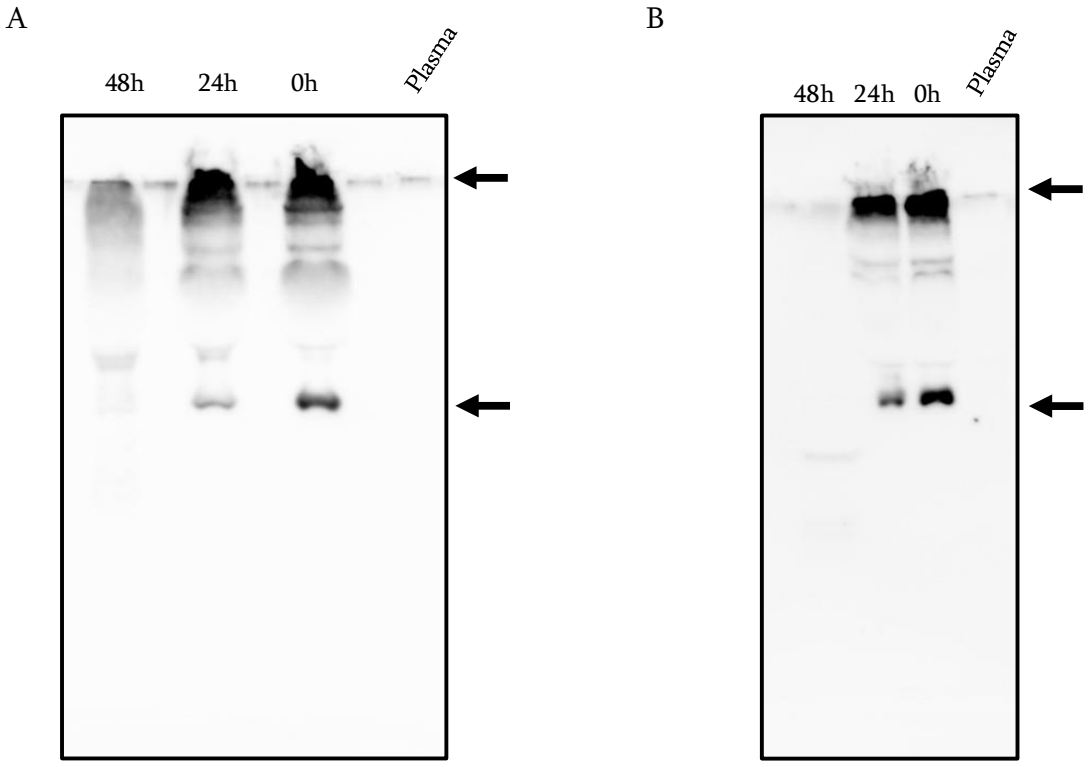

Figure S-6. Stability of OligoBinders in plasma. Western blot analysis of OligoBinder-1 and OligoBinder-3, incubated in plasma for different time intervals (0-48 h) at room temperature, after SDS-PAGE electrophoresis. (A) Sup35-DHFR-LCB1, and (B) Sup35-DHFR-LCB3 were detected using a primary anti-His tag antibody. Plasma without added OligoBinders was used as negative control. The arrows indicate the presence of oligomers (top) and monomeric species (bottom).

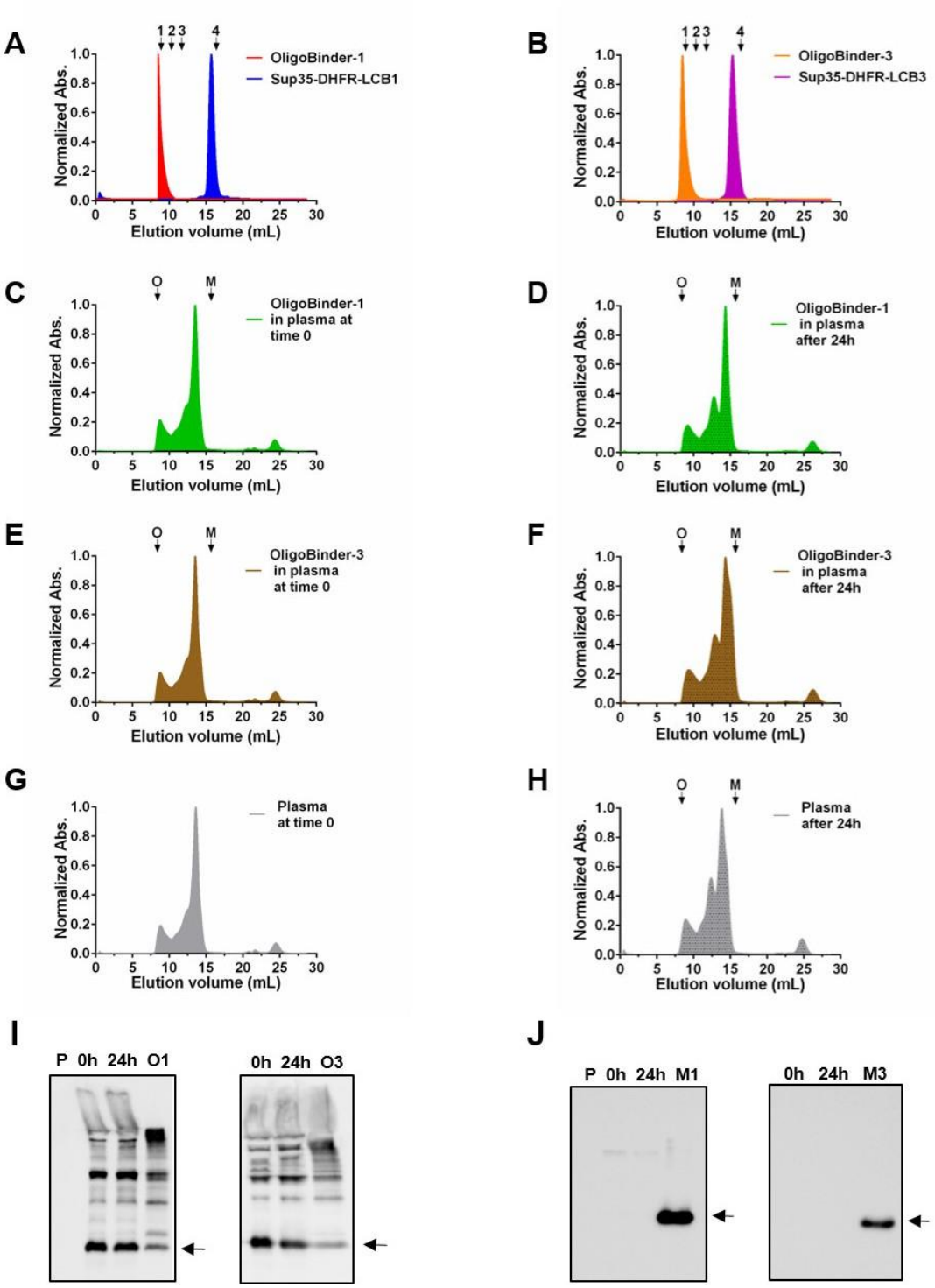
A
1 2 3
4
OligoBinder-1
Sup35-DHFR-LCB1
Normalized Abs.
Elution volume (mL)
B
OligoBinder-3
Sup35-DHFR-LCB3
C
O
M
OligoBinder-1 in plasma at time 0
D
OligoBinder-1 in plasma after 24h
E
OligoBinder-3 in plasma at time 0
F
OligoBinder-3 in plasma after 24h
G
Plasma at time 0
H
Plasma after 24h
I
P 0h 24h O1
0h 24h O3
J
P 0h 24h M1
0h 24h M3

Figure S-7. Characterization of OligoBinders size and stability in plasma. (A) and (B) elution profiles of Oligobinders 1 and 3 and their corresponding monomers after size exclusion chromatography (SEC) fractionation. Black arrows 1 to 4 stands for size reference molecular weight markers: 1= thyroglobulin 669 kDa, 2= ferritin 440 kDa, 3= β-amylase 200 kDa, 4= carbonic anhydrase 29 kDa. (C) and (E) elution profiles of OligoBinder-1, and 3 incubated in plasma, and (G) plasma alone at time 0. (D) and (F) elution profiles of OligoBinder-1 and 3 incubated in plasma, and (H) plasma alone after 24h. Black arrows O and M indicate the fractions that were analyzed by SDS-PAGE. They correspond to the fractions where OligoBinders and their monomers are expected to elute according to their profiles in (A) and (B). (I) and (J) SDS-PAGE immunoblotting of the different O and M fractions. Soluble monomeric Sup35-DHFR-LCB1 and 3, and OligoBinders 1 and 3 in sodium phosphate buffer were used as positive controls. Plasma without added OligoBinders was used as a negative control. The arrows indicate the monomeric species. Abbreviations: P, plasma; O1,3, OligoBinder-1 and 3; M1,3, Sup35-DHFR-LCB-1 and 3 monomers.